MOBILE BOOM CRANES AND ADVANCED INPUT SHAPING CONTROL

A Thesis
Presented to
The Academic Faculty

by

Jon Danielson

In Partial Fulfillment
of the Requirements for the Degree
Master of Science in the
School of Mechanical Engineering

Georgia Institute of Technology
August 2008

MOBILE BOOM CRANES AND ADVANCED INPUT SHAPING CONTROL

Approved by:

William Singhose, Committee Chair
School of Mechanical Engineering
Georgia Institute of Technology

Mark Costello
School of Aerospace Engineering
Georgia Institute of Technology

Wayne Whiteman
School of Mechanical Engineering
Georgia Institute of Technology

Date Approved: June 16, 2008

ACKNOWLEDGEMENTS

There are many people who have helped me reach this point in my life, but none are more important than my parents. I greatly thank them for everything they have sacrificed for and given to me. I would also like to thank all the teachers and professors who helped me along the way; my advisor, Dr. William Singhose, for his advice and guidance in preparing this thesis. Thanks be to my labmates, whose consistent help and input, made graduate school a great place to work.

TABLE OF CONTENTS

LIST OF TABLES

LIST OF FIGURES

SUMMARY

Millions of cranes are used around the world. Because of their wide-spread use in construction industries, boom cranes are an important class of cranes whose performance should be optimized. One limitation of most boom cranes is they are usually attached to a stationary base or a mobile base that is only used for initial positioning and not during operation. This limits the workspace of the boom crane significantly. If a boom crane was attached to a mobile base that could be safely used during lifting operations, then the boom crane workspace could be extended significantly.

The problem with using cranes, and in particular mobile cranes, is the large oscillations of the payload that are typically induced when moving the crane. One control strategy that has been used to control oscillation on other types of cranes is called Input Shaping, a command filtering technique that reduces motion-induced vibration in oscillatory systems.

This thesis develops a dynamics model for a mobile boom crane and analyzes the difficulty of controlling payload oscillation on a boom crane. Input shaping will shown to be effective for controlling oscillation on boom cranes. A new method for operating a boom crane in Cartesian coordinates will also be shown. This thesis will also detail the design of a small-scale mobile boom crane for experimental and research purposes.

A substantial part of this thesis will also focus on the development of new input-shaping methods for nonlinear drive systems commonly found on boom and other types of cranes. An example application of a control system featuring input shaping for an industrial bridge crane will also be discussed.

CHAPTER I

INTRODUCTION

1.1 Concepts: Boom Cranes

A boom crane is distinguished from other cranes by its use of a single boom which pivots and rotates on a base at one end; the payload is hoisted from the other. Most boom cranes are stationary, such as those in Figure 1.1. The crane in Figure 1.1(a) is a pedestal boom crane. It uses cables to pivot the boom up and down, a motion called luffing. The crane in Figure 1.1(b) is a hydraulic boom crane. Instead of using a cable system to luff the boom, it uses a hydraulic cylinder. Both styles of cranes use a motor to rotate the boom about a vertical axis, a motion called slewing.

Another category of boom cranes, called rough-terrain or mobile-boom cranes, are usually smaller in scale than their stationary counterparts. Figure 1.2 shows two types of these cranes. Despite being called mobile cranes in industry, they are not mobile in the sense

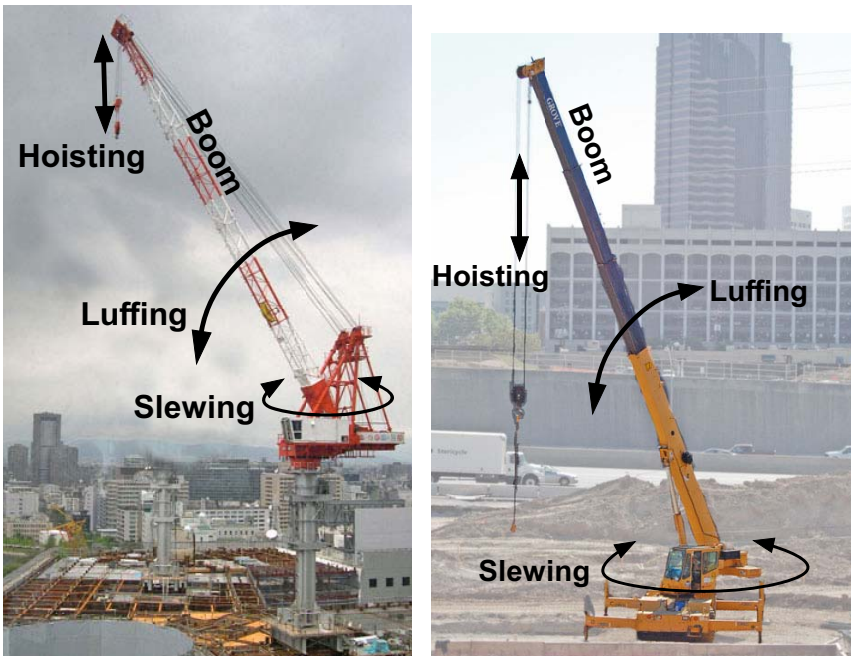

(a) Pedestal Boom Crane (b) Hydraulic Boom Crane

Figure 1.1: Two Types of boom cranes

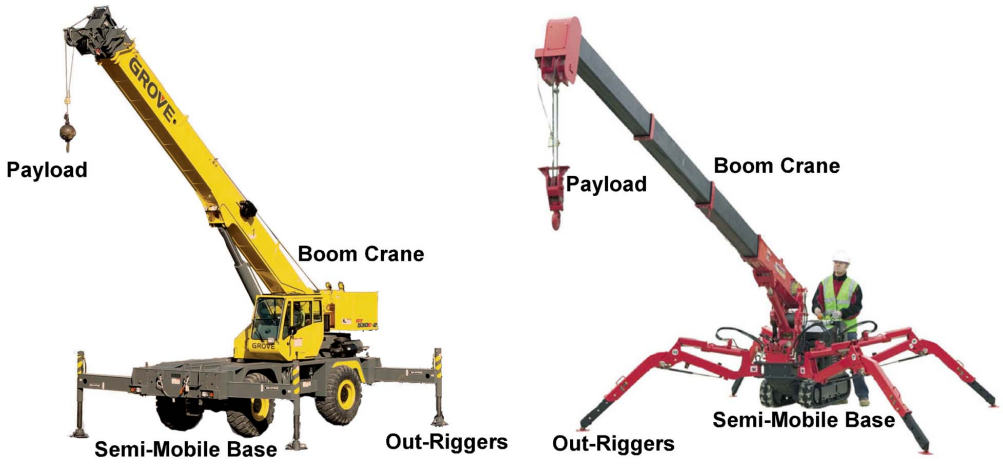

(a) A Rough Terrain Boom Crane. Picture Courtesy of *Manitowoc Crane Group*© [38]

(b) A Mini Boom Crane. Picture Courtesy of *UNIC mini cranes*© [66]

Figure 1.2: Two Types of Mobile Boom Cranes (Size Scales Not Equal)

that the crane can move while a payload is being manipulated. This is why the base of both cranes in Figure 1.2 are labeled *semi-mobile*. These semi-mobile cranes usually require outriggers to stabilize the crane while it manipulates a payload. In this thesis, a mobile crane will refer to a crane that has the capability to operate while the base is in motion. The ideas presented in this thesis will lay the ground-work for further advancement of this style of crane.

A diagram of a common way to actuate a boom crane is shown in Figure 1.3. This actuation method, most commonly used on a crawler crane, is a simple method that uses cables to luff the boom and hoist payload of the crane. One cable, labeled the luff cable in the diagram, runs from the motor on the base of the crane over a point on a static member of the crane called a jib, and then connects to the tip of the boom. The purpose of this cable is the luff the boom up and down. A second cable, labeled the hoist cable, is connected to the payload over a pulley at the end of the boom and hoists the payload up and down. The jib member acts as a support for the hoist and luff cables, improves the stability of the crane, and reduces the actuation force to raise and lower the boom and payload.

The mass of the payload is supported by transferring the weight radially down the axis of the boom and through the hoist and luff cables. All boom cranes have some type of counterweight to keep the center of mass of the crane above the base. The crawler-crane

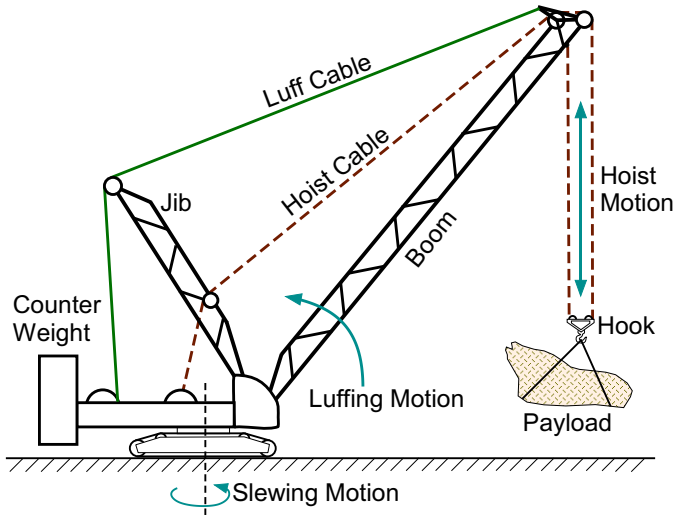

Figure 1.3: A Common Actuation System for a Boom Crane

style of actuation system will be used throughout this thesis as the default style of actuation for a boom crane.

Control Methods

A boom crane presents an especially challenging problem for oscillation control because of its actuation system and dynamic nonlinearities. Luffing and slewing motions impart complicated accelerations to the payload that result in nonlinear payload dynamics. Further complications of the dynamics occur when the crane is on a mobile base. With the added degrees of freedom, merely finding the most efficient ways to operate a mobile boom is a challenging research question, let alone controlling payload oscillation.

Three possible types of oscillation-control strategies for cranes are i) training highly-skilled operators, ii) input shaping, and iii) feedback control. Input shaping has successfully been implemented on many cranes [44, 17, 51]. While it works best on systems that behave linearly, input shaping is effective on moderately nonlinear systems. However, the performance of input shaping is degraded by the nonlinear effects. An analysis of the performance of input-shaping on boom cranes is an important contribution of this thesis.

Another type of vibration control technique that has been implemented on cranes is feedback control. While feedback control can be successful and has been implemented on cranes [12, 19], it is more difficult and expensive to implement than input-shaping control. As the effectiveness of input shaping is reduced, or when disturbances are introduced into

the system, the use of feedback control becomes more justifiable. For example, a mobile boom crane will have significant disturbances from driving the crane over uneven terrain. For a more complete and effective oscillation control strategy, a combination of command shaping and feedback control would be necessary.

Many groups have the investigated various facets of boom crane control. Sawondy introduces a combination feedback and feedforward controller to control the sway of a hydraulic boom crane. The oscillation of the payload is measured using gyroscopes and the feedforward controller uses a plant-inversion method [39]. Lewis used a notch filter to control payload oscillation [28]. This approach is similar to input shaping in that modification of the command sent to the boom crane is the only method to limit oscillation. It has been shown however, that these type of command smoothing filters are not as efficient (as far as system rise-time) as input shaping [45, 68]. Arnold creates command profiles using an optimization approach to limit payload oscillation. While this technique can produce near-zero oscillation, the entire trajectory of the boom crane must be known ahead of time[3]. For most human-operated cranes, this is not an option. Abdel-Rahman uses changes in pendulum length to reduce oscillation in boom cranes [1].

1.2 Concepts: Input Shaping

Input shaping is a filtering technique that reduces vibration in a flexible system. Input shaping works by convolving a reference signal with a series of impulses called an input shaper. The timing and amplitude of these impulses are chosen such that when applied to an oscillatory system, the vibration caused by the sequence impulses cancels out [42, 55].

To understand how input shaping works, first consider a single impulse, A_1, applied to an undamped flexible system. Then, another impulse, A_2, of the same amplitude is applied one half of the period of oscillation later. The response from both impulses is shown in Figure 1.4. If a system is sufficiently linear, superposition may be used to find the total response to both impulses. This total superimposed response is also shown in Figure 1.4 as a solid line. Because the amplitudes of the impulses are equal and they are separated by one half of the oscillation period, the vibration caused by A_1 is canceled by A_2. One of the

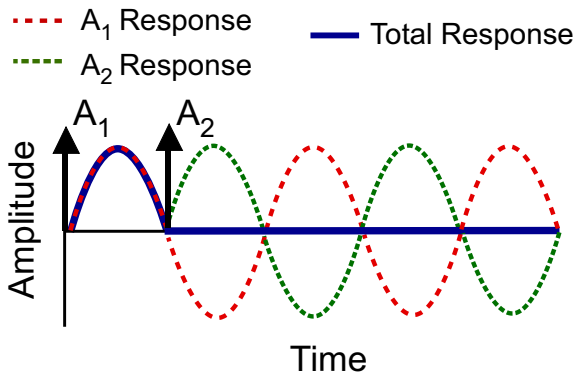

Figure 1.4: Zero Vibration Response to Two Impulses

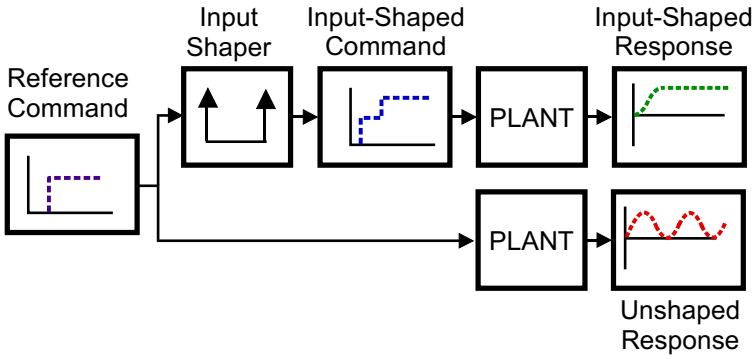

Figure 1.5: Input Shaping Process

first descriptions of this effect appeared in O.J.M Smith's paper in 1957 [56]. By changing the number, timing, and amplitude of the impulses, different input shapers with different time and frequency domain properties can be created.

An input shaper can be convolved with an arbitrary baseline command to from an input-shaped command. The convolution process preserves the vibration-reducing properties of the input shaper. Therefore, the input-shaped command will cause zero vibration at the modeled frequency if the input shaper causes zero vibration at the modeled frequency. Figure 1.5 shows a block diagram of the input-shaping process and how it compares to command generation without input shaping.

The downside to input shaping is that it increases the rise time of the system, as illustrated in Figure 1.6. The increased rise time is equivalent to the time of the last impulse, t_n. This time is known as the shaper duration. Although the delay associated with input-shaping is a drawback, the benefit to using input shaping to control vibration over a

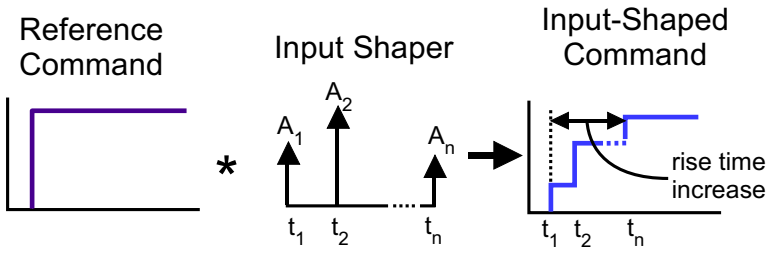

Figure 1.6: Rise Time Increase Associated with Input Shaping

feedback controller is that input shaping requires no sensors and does not alter the stability of the flexible system. Input shaping has also been shown to be superior to other types of command filters, such as first order and s-curves, for many different control scenarios [10, 68, 45].

One important property of input shapers is robustness to frequency modeling errors. For example, the frequency of payload oscillation in a boom crane is affected by many factors, primarily by changing the payload suspension length. The robustness of an input-shaper can be measured using a sensitivity plot [42], as shown in Figure 1.7. The horizontal axis shows the normalized frequency, which is defined as the actual frequency, ω_n, divided by the model frequency, ω_m. The vertical axis shows the normalized vibration, which is defined as the residual vibration from a unit impulse divided by the residual vibration caused by the input-shaper impulses. The width of each curve in Figure 1.7 is an indication of shaper robustness: the wider the curve, the more robust the shaper. A numerical way to describe the robustness of an input shaper is called its Insensitivity; which is defined as the width of the sensitivity curve at a certain percent residual vibration. For example, the EI input shaper in Figure 1.7 has an insensitivity of 40% ($\pm$20% about 1) measured at 5% residual vibration.

Figure 1.7 shows the sensitivity curves of three common input shapers. Each of these shapers is formed using a different set of design constraints. The Zero Vibration (**ZV**) input shaper has the least amount of robustness. As the actual frequency deviates from the modeled frequency the residual vibration increases rapidly[56, 64]. The input-shaper used

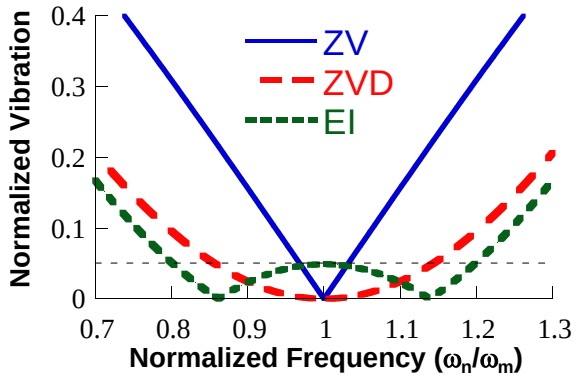

Figure 1.7: Sensitivity Curves for ZV and ZVD Input Shapers

in Figure 1.4 was a ZV Shaper. For an undamped system, the ZV shaper is given by:

$$\text{ZV} = \begin{bmatrix} A_i \\ t_i \end{bmatrix} = \begin{bmatrix} \frac{1}{2} & \frac{1}{2} \\ 0 & \frac{T}{2} \end{bmatrix} \tag{1.1}$$

Where A_i is the impulse amplitude, t_i is the impulse time, and T is the period of vibration.

The Zero Vibration and Derivative (**ZVD**) shaper is formed by enforcing a zero-derivative constraint on its sensitivity curve at the model frequency [42]. Thus, it's robustness is increased significantly. This robustness comes a cost though, the ZVD input shaper is twice the duration of the input shaper for the undamped case. A ZVD shaper designed for an undamped natural frequency is given by:

$$\text{ZVD} = \begin{bmatrix} A_i \\ t_i \end{bmatrix} = \begin{bmatrix} \frac{1}{4} & \frac{1}{2} & \frac{1}{4} \\ 0 & \frac{T}{2} & T \end{bmatrix} \tag{1.2}$$

The Extra-Insensitive (**EI**) shaper is formed by allowing a small amount of vibration at the modeled frequency while maximizing the sensitivity curve width [50]. Its duration is approximately equal to the ZVD input shaper, but has a greater insensitivity because of the small vibration allowed at the modeling frequency. The extra insensitivity can be seen in Figure 1.7. This design technique is justified because with real systems it is never possible to achieve zero vibration. Therefore, the zero-vibration constraint is relaxed to a more realistic goal of residual vibration, so that more robustness can be achieved. A more detailed analysis of robust input shapers can be found in [67].

Another type of robust shaper is the Specified Insensitivity (**SI**) shaper [47, 51]. It is

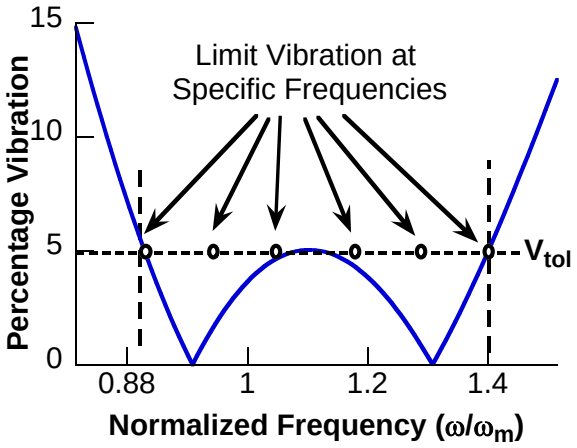

Figure 1.8: Sensitivity Curve for SI Shaper.

formed by limiting the vibration at a few specific frequencies over any desired insensitivity range. The residual vibration is constrained to be less than or equal to a specified upper-bound at each of these points, as shown in Figure 1.8. This shaper has the advantage that it can be designed to be arbitrarily robust to frequency changes. The SI input shaper is calculated using a numerical optimization routine. Because only a few frequencies are specified at which vibration is limited, each giving a single constraint equation, the numerical optimization is relatively easty set-up and compute.

A final class of common input shapers is unity-magnitude input shapers. The impulses of these input shapers have magnitudes of either $+1$ or -1. The most common is a Unity Magnitude Zero Vibration (UMZV) input shaper [53]. For an undamped system, it has the form:

$$\text{UMZV} = \begin{bmatrix} A_i \\ t_i \end{bmatrix} = \begin{bmatrix} 1 & -1 & 1 \\ 0 & \frac{T}{6} & \frac{T}{3} \end{bmatrix} \tag{1.3}$$

The benefit to using unity magnitude shapers is that they are faster than their positive magnitude counterparts. For example, the UMZV shaper has a duration of $T/3$ and the ZV shaper has a duration of $T/2$. However, they are generally less robust to modeling errors and have the tendency to excite higher un-modeled oscillation modes. Unity magnitude shapers are also compatible with on/off actuation systems such as thruster jets and relay-driven electric motors. For these types of systems, UM shapers are the only input shaping option.

Because input shaping works best for linear systems, the implementation of input shaping on such systems has been widely successful [51, 13, 43, 31, 11, 60]. Despite being designed for linear systems, input shaping has been adapted to work well for nonlinear systems as well [26, 18, 20]. One particular nonlinear system of interest that input shaping has been successfully applied to is a tower crane. Because a tower crane has a slewing motion analogous to a boom crane, the successful application of input shaping on tower crane slewing can be transferred to boom crane slewing. It was shown by Lawrence and Blackburn that a ZVD shaper showed good performance in reducing sway when performing slewing maneuvers [6, 21]. Two new input-shaping algorithms were also developed for slewing motions. The effectiveness of input shaping on luffing motions, in addition to slewing motions, of a boom crane will be shown in this thesis.

1.3 Thesis Contributions

The primary contributions of this thesis are:

1. A development of full nonlinear dynamic equations of motion for a boom crane and an analysis of the difficulties of controlling its motion.

2. Analysis of the affect of input shaping on boom crane motion is investigated.

3. A description of a new method of operation for a boom crane using Cartesian coordinates rather than the crane's native spherical coordinates.

4. A small scale mobile boom crane was designed to be a test apparatus for researchers, as well as a platform for students to learn and conduct experiments.

5. Three new input-shaping strategies are presented. Two involve adapting input shaping for non-linear actuation dynamics. The third is a new multi-mode shaping design strategy.

6. A discussion of an application of input shaping and feedback control on an industrial bridge crane is presented.

CHAPTER II

DYNAMIC BEHAVIOR OF BOOM CRANES

This chapter investigates the dynamics of mobile boom cranes. Equations of motion for a mobile boom crane are derived and verified in Sections 2.1 and 2.2. Section 2.3 presents the challenges of controlling luffing motions on a boom crane. Next, an evaluation of the effectiveness of conventional input-shaping control on boom cranes is given in Section 2.4. Finally, an analysis of the effect of vertical acceleration on a pendulum, motivated by dynamic effects found in luffing dynamics, is given in Section 2.5.

2.1 Mathematical Model - Mobile Boom Crane

The dynamic equations of motion for a mobile boom crane was derived using Kane's method[1]. Figure 2.1 shows a diagram of the mobile boom crane containing definitions of reference frames, dimensions, and key points used to derive the equations. The model is composed of three rigid bodies: **Base, Boom,** and **Cable**. The payload of the crane is treated as a point mass, **P**. Each body has an associated reference frame, **B, J,** and **C**, respectively. These frames are shown in Figure 2.1 attached to their respective bodies. In addition to these three body frames, there is a Newtonian (inertial) reference frame **N**. A chart showing the progression of the reference frames, along with intermediate reference frames used in this derivation is shown in Figure 2.2. Two reference points fixed in the crane, **D** and **E**, will be used to define the velocities and accelerations of key points on the crane. The payload, defined as **P**, of the crane is treated as a point mass fixed in **C**.

The configuration of the mobile boom crane is defined as follows. The symbols x and y define the position of the mobile base in the newtonian frame:

$$\vec{P}_{N_O \to B_O} = x\mathbf{N}_1 + y\mathbf{N}_2 \tag{2.1}$$

where N_O is the origin of frame **N** and B_O is the origin of frame **B**. The base rotates about

[1]The *Autolev* source code used to create the equations can be found in Appendix A

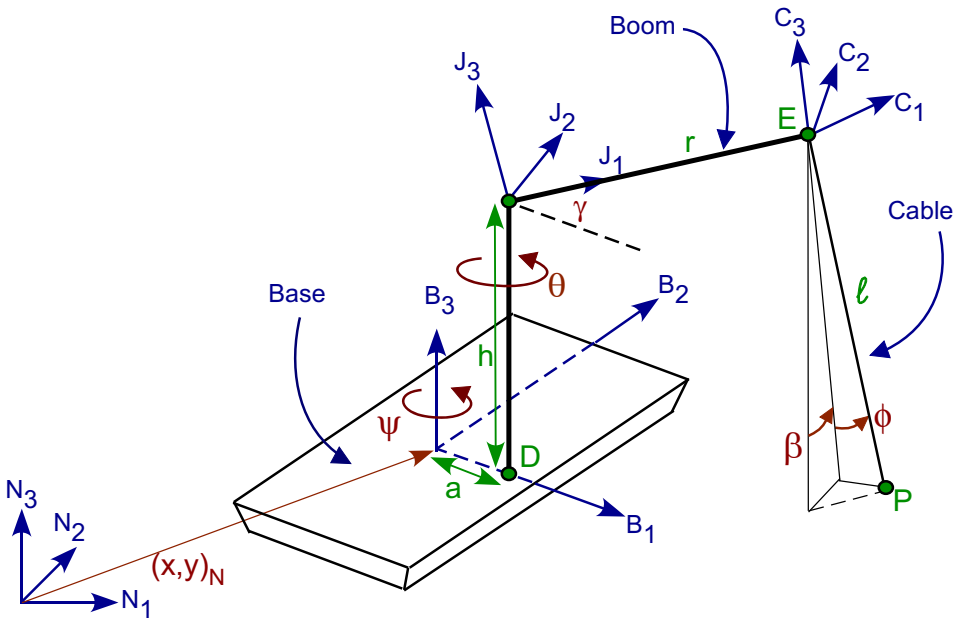

Figure 2.1: Mobile Boom Crane Coordinate Diagram

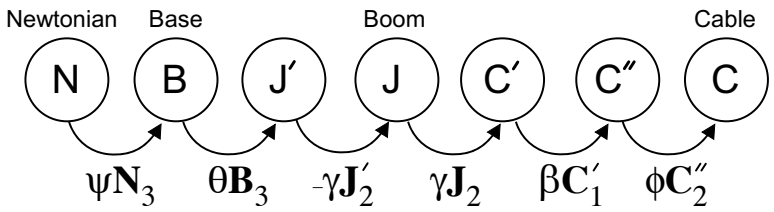

Figure 2.2: Coordinate Frames Used to Define Boom Crane Motion

the $\mathbf{N}_3$ axis by an angle ψ:

$$\vec{\omega}_{B/N} = \dot{\psi}\mathbf{N}_3 \tag{2.2}$$

The position of the bottom of the boom is defined as:

$$\vec{P}_{B_O \to J_O} = a\mathbf{B}_1 + h\mathbf{B}_3 \tag{2.3}$$

The slew rotation of the boom is defined by an angle θ:

$$\vec{\omega}_{J'/B} = \dot{\theta}\mathbf{B}_3 \tag{2.4}$$

where J' is an intermediate reference frame in which the luff of the boom is referenced:

$$\vec{\omega}_{J/J'} = -\dot{\gamma}\mathbf{J}'_2 \tag{2.5}$$

The negative sign ensures that a positive angle angular velocity corresponds to an upwards luffing of the boom. In order to assure that the cable aligns with the $\mathbf{N}_3$ axis when the

Table 2.1: Variables used in mobile boom crane model

Category	Variable
Base Motion (Specified)	x
	y
	ϕ
Boom Motion (Specified)	θ
	γ
	ℓ
Payload Motion (Motion)	ϕ
	β

swing angles of the pendulum are zero, an intermediate reference frame, C', rotates the opposite of the luff angle:

$$\vec{\omega}_{C'/J} = \dot{\gamma}\mathbf{J}_2 \tag{2.6}$$

The point where the cable pendulum attaches to the **Boom** (**E**) is defined as:

$$\vec{P}_{J_O \to E} = r\mathbf{J}_1 \tag{2.7}$$

Where $\mathbf{J}_O$ is the origin of frame **J**. The swing of the pendulum is defined by angles β and ϕ; where β is the tangential swing and ϕ is the radial swing:

$$\vec{\omega}_{C''/C'} = \dot{\beta}\mathbf{C}'_1 \tag{2.8}$$

$$\vec{\omega}_{C/C''} = -\dot{\phi}\mathbf{C}''_2 \tag{2.9}$$

Note the use of another intermediate reference frame, C'', and that $\dot{\phi}$ is defined as positive away from the base. Finally, the position of the crane's payload is defined as:

$$\vec{P}_{E \to P} = -\ell\mathbf{C}_3 \tag{2.10}$$

The variables chosen to describe the position of the crane can be categorized as either inputs (specified variables) or outputs (motion variables). Table 2.1 summarizes these.

The kinematics of the mobile boom crane can now be derived. This is done by specifying known positions, angular velocities, and accelerations. The angular velocities were defined previously, and the point velocities of $\mathbf{B}_O$, **D**, $\mathbf{J}_O$, **E**, and **P** can be found by taking the

derivative of their respective position vectors. The acceleration of the payload is the primary concern of this analysis. It can be found by differentiating the velocity of **P** in the inertial reference frame:

$$\vec{a}_{P/N} = \frac{^{N}d}{dt}\vec{v}_{P/I} \tag{2.11}$$

The only external force acting on the system is gravity. It is defined as:

$$\vec{F}_g = -g\mathbf{N}_3 \tag{2.12}$$

Finally, the dynamic model is:

$$\ddot{\beta} = F\left(\ell, r, \dot{\theta}, \dot{\gamma}, \ldots\right) \tag{2.13}$$

$$\ddot{\phi} = H\left(\ell, r, \dot{\theta}, \dot{\gamma}, \dot{\beta}, \ldots\right) \tag{2.14}$$

The full equations of motion, not shown here for brevity, can be found in (A.1) and (A.2) in Appendix A.

2.2 Verification of Model

In order to validate the model, (2.14) and (2.13) were compared with three other crane models. First, equations of motion for a stationary boom crane was used to verify the luffing and slewing component of the mobile boom crane model. Second, because the the mobile boom crane with only base motion is identical to a bridge crane, a comparison of x and y base inputs was verified with a bridge crane model. Finally, a comparison of the dynamic model derived from Kane's method was compared to a dynamic model derived from Lagrange's Equations. With these three tests, confidence in the mobile boom crane model can be established.

A partially-linearized model for a stationary boom crane was developed in [28]:

$$\ddot{\beta} = \frac{-2\dot{\ell}}{\ell}\dot{\beta} - 2\dot{\theta}\dot{\phi} - \left(-\dot{\theta}^2 - \frac{rsin(\gamma)\ddot{\gamma}^2}{\ell} + \frac{rcos(\gamma)\ddot{\gamma}}{\ell} + \frac{g}{\ell}\right)\beta - \left(\dot{\theta}p + \frac{2\dot{\theta}\dot{\ell}}{\ell}\right)\phi - \frac{rcos(\gamma)\dot{\theta}p}{\ell} + \frac{2rsin(\gamma)\dot{\theta}\dot{\gamma}}{\ell} \tag{2.15}$$

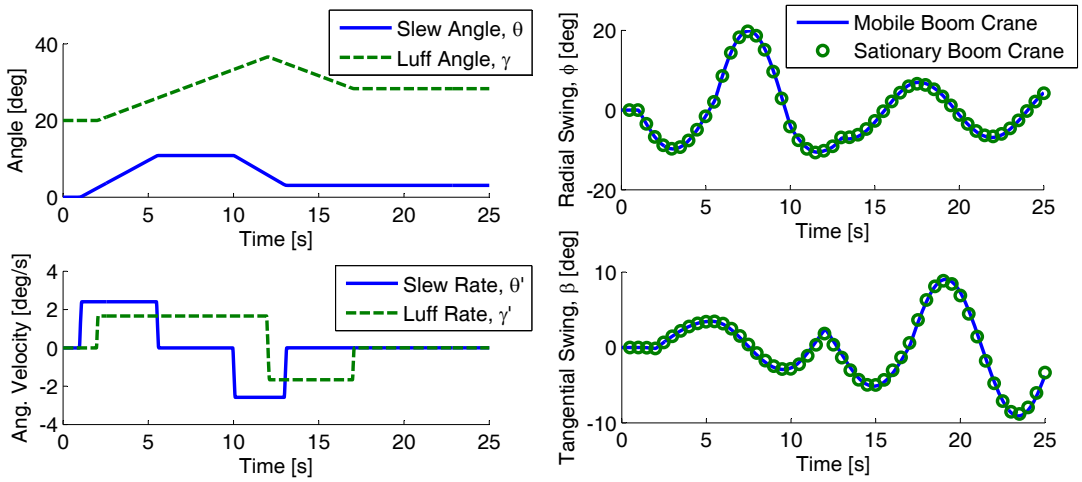

(a) Luffing and Slewing Inputs

(b) Response of Pendulum

Figure 2.3: Example Crane Maneuver Showing Congruence Between Mobile Boom Crane Model and a Stationary Boom Crane Model

$$\ddot{\phi} = 2\dot{\theta}\dot{\beta} - \frac{2\dot{\ell}}{\ell}\dot{\phi} - \left(\frac{-2\dot{\theta}\dot{\ell}}{\ell} - \ddot{\theta}\right)\beta - \left(-\dot{\theta}^2 - \frac{rsin(\gamma)\dot{\gamma}^2}{\ell} + \frac{rcos(\gamma)\ddot{\gamma}}{\ell} + \frac{g}{\ell}\right)\phi + \frac{rcos(\gamma)\dot{\theta}^2}{\ell} + \frac{rcos(\gamma)\dot{\gamma}^2}{\ell} + \frac{rsin(\gamma)\ddot{\gamma}}{\ell} \quad (2.16)$$

This model assumes small payload swing angles and that $\dot{\phi}^2$ and $\dot{\beta}^2$ are negligible. A sample luffing and slew move, shown in Figure 2.3(a), was input into the dynamic model of (2.15) and (2.16) and also the mobile boom crane model of(2.14) and (2.13). The crane parameters (r, ℓ, $\dot{\gamma}$, and $\dot{\theta}$) for A Kobelco CK800 crane were used in the simulation. Figure 2.3(b) shows the response of the two models aligns exactly. Numerous other commands of various durations and amplitudes were also simulated. The agreement between the two models provides confidence in the slewing and luffing component of the mobile boom crane model.

When the base of the mobile boom crane (without rotation, ψ) is the only input to the system, the payload behaves as though it were attached to a bridge crane. To verify the mobile boom crane model produces such results, x and y inputs were simulated on the mobile boom crane model and a standard bridge crane dynamic model:

$$\ell\cos(\beta)\ddot{\phi} + g\sin\phi + \ddot{x}\cos\phi - 2\ell\sin\beta\dot{\beta}\dot{\phi} = 0 \quad (2.17)$$

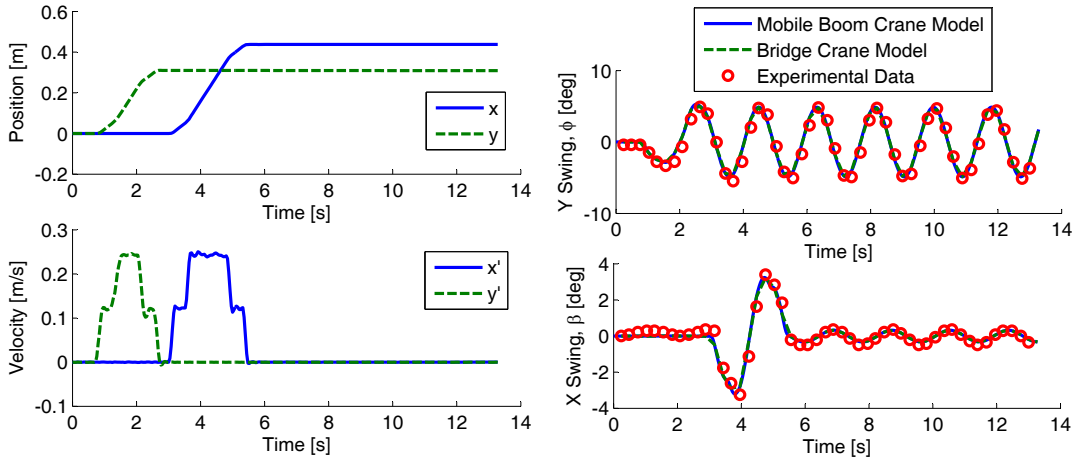

(a) x and y Position Inputs

(b) Response of Pendulum

Figure 2.4: Example Base Maneuver Showing Congruence Between Mobile Boom Crane Model and Bridge Crane Model

$$\ell\ddot{\beta} + g\sin\beta\cos\phi + \ddot{y}\cos\beta + \ell\sin\beta\cos\beta\dot{\phi}^2 - \ddot{x}\sin\beta\sin\phi = 0 \tag{2.18}$$

The two base inputs, shown in Figure 2.4(a), produced nearly identical pendulum responses, as shown in Figure 2.4(b). These two inputs were also experimentally tested on a portable bridge crane. Both models match the actual pendulum response, shown as circles in Figure 2.4(b), very well. As with the stationary model, this congruence provides further confidence in the mobile boom crane model.

As a final verification, the mobile boom crane model in (2.14) and (2.13) developed using Kane's Method was tested against a model developed using Lagrange's Equations. For brevity, a detailed analysis of the derivation of the equations of motions using Lagrange's Equations will not be given here, but the *Matlab* code used to derive the equations can be found in Appendix B. Figure 2.5(a) shows the base and crane inputs were given simultaneously to both models. Figure 2.5(b) shows that the responses are indistinguishable.

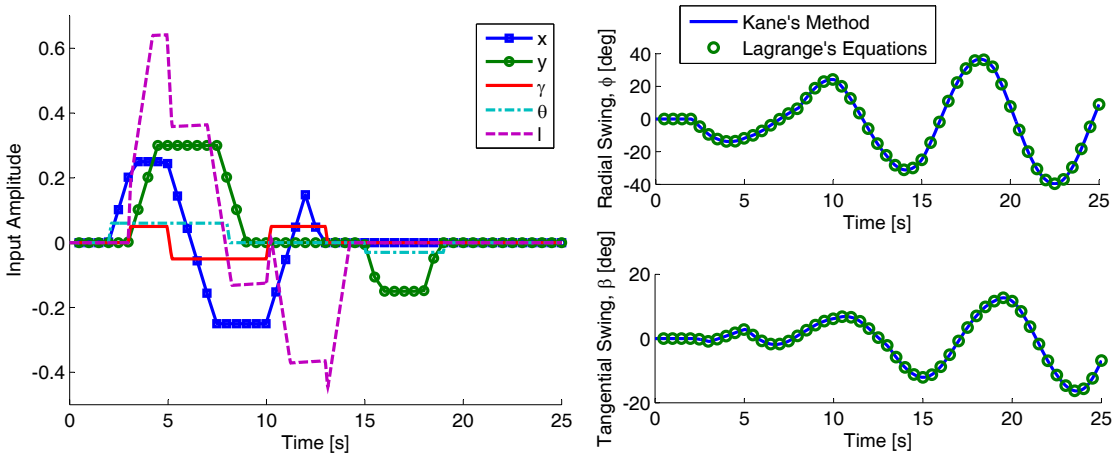

(a) Model Inputs

(b) Response of Pendulum

Figure 2.5: Example Maneuver Showing Congruence Between Mobile Boom Crane Model Developed with Kane's Method and Lagrange's Equations

2.3 Luffing Dynamics

Luffing motions in boom cranes present unique challenges in oscillation reduction for control system designers. This section examines the complicated actuation and oscillatory dynamics that occur in luffing motion.

For many types of cranes, the elements in the control system are constant. For example, Figure 2.6 shows a block diagram for a bridge crane. A reference command is first issued to the crane's motors. The dynamics of the motors for these crane's are constant; meaning they do not vary with time or configuration of the crane. The motor dynamics include a second-order plant and typically a velocity limit, acceleration limit, and usually a velocity dead-zone. Configuration dependent dynamics refer to dependency of the dynamics on the luffing angle of the boom. The motors impart motion to the crane's pendulum suspension point and cause oscillation. The motion of the pendulum can be described by linear time

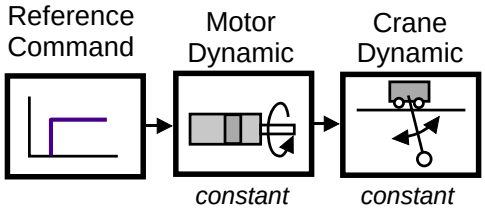

Figure 2.6: Block Diagram for Tower or Bridge Crane Motion

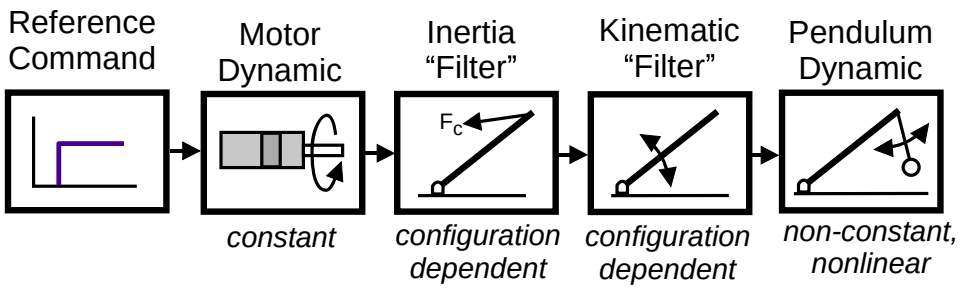

Figure 2.7: Block Diagram for a Luffing Motion on a Boom Crane

and crane-configuration independent dynamic models[2] . This independence makes control of bridge cranes relatively straight forward.

Luffing motions of a boom crane do not share this configuration and time independence. Figure 2.7 shows a block diagram of luffing motion on a boom crane. The first two blocks of the system are identical to the bridge: a reference command is sent to a motor whose dynamics are time and crane-configuration independent. The Inertia Filter describes how the force requirement on the luffing cable by the motor varies as the luffing angle changes. Section 2.3.1 examines this filter in detail.

After the inertia filter, a second filter relates how the luffing rate changes with the luffing angle. This effect can be considered a kinematic filter (relating to the motion of the crane) whereas the inertial filter could be considered a kinetic filter (relating to the forces that induce motion). However, both originate from the same phenomenon: the actuation requirements change as a function of luffing angle. Section 2.3.2 describes the kinematic filter in detail.

The final block is the pendulum dynamics of the payload. Section 2.3.3 will show how pendulum oscillation can have multiple time-varying frequencies and that the influence of luffing motion on pendulum oscillation will change with the luffing angle and speed.

[2]Because all crane models depend on payload suspension length, the term "crane-configuration independent" does not include payload suspension length changes, only the mechanisms of the crane that move the payload suspension point.

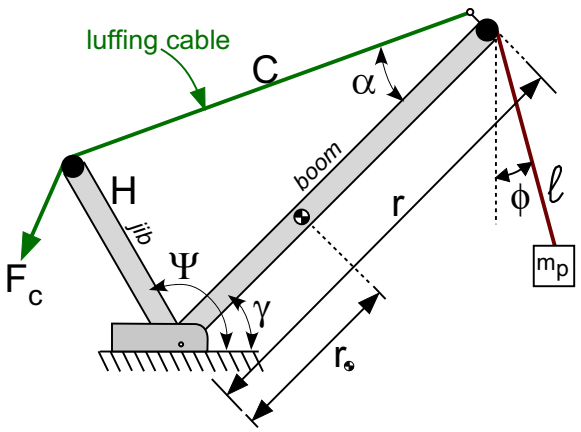

Figure 2.8: Structural Diagram Showing Luffing Cable Force

2.3.1 Inertia Filter

The parameters of the boom crane that are important for analyzing the inertial filter are shown in Figure 2.8. The force from the luffing motor, F_c acts on the end of the boom at an angle α. The luffing cable is supported by the jib that has a length H and is at an angle Ψ to the horizontal. The boom of length r has a center of mass at $r_{\oplus}$ from the base of the boom.

The angle at which F_c acts relative to the boom, α, must be determined from known geometry of the system. First, the length of luffing cable from the jib to the boom, C, must be determined. From the law of cosines for the triangle with sides C, H, and r:

$$C = \sqrt{H^2 + r^2 - 2Hr\cos(\Psi - \gamma)} \tag{2.19}$$

Now, α can be shown to be:

$$\sin(\alpha) = \frac{H\sin(\Psi - \gamma)}{\sqrt{H^2 + r^2 - 2Hr\cos(\Psi - \gamma)}} \tag{2.20}$$

Which is a function of the constant geometry of the crane: H, r, and Ψ; and γ, which is not constant.

A free body diagram showing all the forces acting on the boom is shown in Figure 2.9. The boom has a mass m_b and a moment of inertia about its rotation point I_b. The force from the payload, labeled F_p in the figure, depends on its motion. The payload swing angle was defined relative to the vertical as ϕ. The magnitude of F_p can easily be determined by

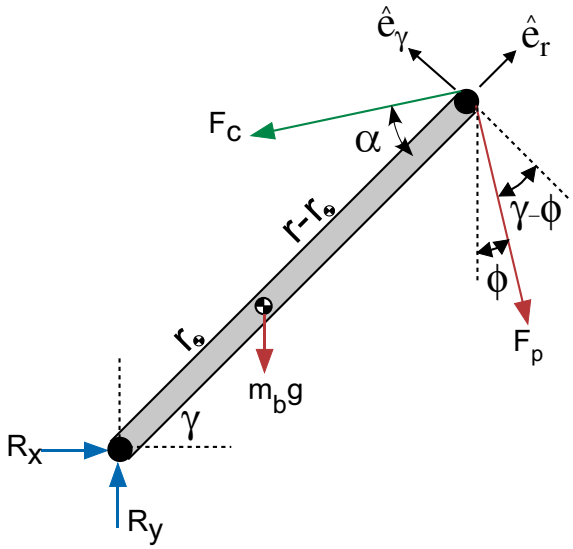

Figure 2.9: Free Body Diagram of Boom

using Newton's second law: $\left(\vec{F} = m\vec{a}\right) \cdot \hat{e}_p$; where $\hat{e}_p$ is a unit vector along the axis of the payload suspension cable:

$$F_p = m_p \left(\ell\dot{\phi}^2 + g\cos\phi\right) \tag{2.21}$$

The only unknown forces acting on the boom are the reaction forces R_x and R_y and the luffing force F_c. The three Newton-Euler equations for this system (2 translational in the $\hat{e}_r$ and $\hat{e}_\gamma$ directions and one rotational) that can be used to solve for these are:

$$\begin{bmatrix} \cos\gamma & \sin\gamma & -\cos\alpha \\ -\sin\gamma & \cos\gamma & \sin\alpha \\ r_\oplus \sin\gamma & -r_\oplus\cos\gamma & (r-r_\oplus)\sin\alpha \end{bmatrix} \begin{Bmatrix} R_x \\ R_y \\ F_c \end{Bmatrix} = \begin{bmatrix} -r_\oplus\dot{\gamma}^2 m_b + m_b g\sin\gamma + F_p\sin(\gamma-\phi) \\ r\ddot{\gamma}m_b + m_b g\cos\gamma + F_p\cos(\gamma-\phi) \\ I_b\ddot{\gamma} + F_p(r-r_\oplus)\cos(\gamma-\phi) \end{bmatrix} \tag{2.22}$$

Solving these three linear equations yields an expression for F_c:

$$F_c = \frac{1}{\sin\alpha}\left(\ddot{\gamma}\left(I_b + r r_\oplus m_b\right) + m_p r\left(\ell\dot{\phi}^2 + g\cos\phi\right)\cos(\gamma-\phi) + r_\oplus m_b g\cos\gamma\right) \tag{2.23}$$

This equation shows how the input force from the motor F_c will change as the boom luffs and the payload swings. To better understand the terms in (2.23), it can be rearranged to

group similar terms:

$$F_c = \frac{1}{\sin\alpha}\cdot$$
$$\left(\underbrace{\left(I_b + r r_{\oplus} m_b\right)\ddot{\gamma}}_{\text{boom inertia}} + \underbrace{\left(m_p r \ell \cos\left(\gamma - \phi\right)\right)\dot{\phi}^2}_{\text{payload inertia}} + \underbrace{\left(m_p r \cos\phi \cos\left(\gamma - \phi\right) + m_b r_{\oplus} \cos\gamma\right) g}_{\text{gravity}} \right) \quad (2.24)$$

When the boom crane is operated closer to horizontal and γ is small, the gravity and payload inertial terms have a much more significant contribution to the luffing force than when the boom is closer to vertical. This intuitive result means that the luffing actuator requirements will change greatly throughout the crane's luffing motion.

The magnitude of α has a large effect on F_c as well. From (2.24), the larger $\sin(\alpha)$ is, the less the magnitude of the luffing force force. This increase in $\sin(\alpha)$ can be accomplished by increasing the ratio of H/r; as can be seen from (5.11) or by examining the geometry of the crane in Figure 2.8. From the figure, the larger the value of H, the greater lever arm F_c has on the boom and thus, the required force is lowered.

It should be noted that many cranes have motors that operate on velocity control, meaning that a separate controller on the motor regulates the current/torque sent to the motor to maintain a desired velocity. In such a case, the actuator dynamic and inertial filter described in this section are highly coupled. This leaves the crane operator, or computer controller, essentially unaware of the inertial filter. This operating condition is only valid when the crane motors have enough torque to overcome the inertial and gravity loads from the boom. At small luffing angles and with heavy payloads, this assumption may not hold.

2.3.2 Kinematic Filter

Whether or not the crane luffing motor is under velocity or torque control, the varying force requirement is not the sole challenge for accurate luffing control. Just as the force requirement changed as the boom is luffed, the required speed of the luffing cable to maintain a specific luffing rate changes as the boom luffs. This relationship can be stated mathematically as:

$$\dot{\gamma} = \dot{\gamma}(\dot{C}, \gamma)$$

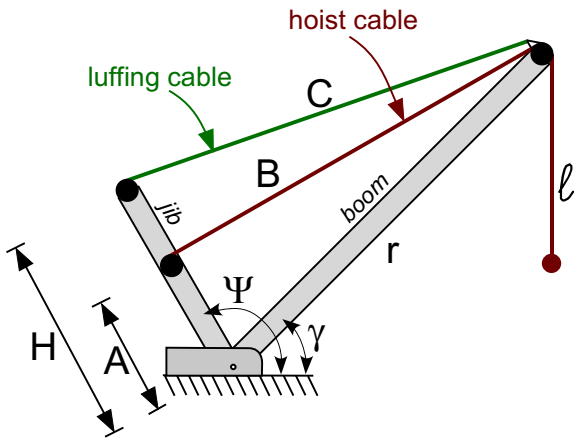

Figure 2.10: Structural Diagram Showing Luffing and Hoisting Cables

Where $\dot{C}$ is the luffing cable speed.

Taking the time derivative of the expression for C in (2.19) yields the luffing line speed, $\dot{C}$:

$$\dot{C} = -\left(\frac{Hr\sin(\Psi-\gamma)}{\sqrt{H^2+r^2-2Hr\cos(\Psi-\gamma)}}\right)\dot{\gamma} \tag{2.25}$$

This equations shows that in order to accurately control luffing motion, the crane motor must adjust its desired speed in accordance to luffing angle in addition to adjusting its torque to overcome the changing inertia. Also, as the ratio of H to R decreases, the ratio of $\dot{\gamma}$ to $\dot{C}$ increases; effectively amplifying the effect of luffing line speed on luffing speed. However, this comes at a cost: the luffing force (F_c) required to rotate the boom increases as H/r decreases; as was discussed previously by examining (2.24).

Figure 2.10 diagrams the geometry of the boom crane that is relevant to the analysis of the kinematic filter. New to this figure is the hoist cable. It runs from a pulley mounted on the jib (labled as a distance A along the jib) to the end of the boom. It will be shown in this section that the suspension length of the payload, a section of the hoist cable, is affected by luffing as well.

Using the law of cosines for triangle with sides A, B, and r in Figure 2.10, a relationship between the payload suspension length and the luffing speed can be established:

$$\dot{B} = -\frac{Ar\sin(\Psi-\gamma)}{\sqrt{A^2+r^2-2Ar\cos(\Psi-\gamma)}}\dot{\gamma} \tag{2.26}$$

Where B is the section of hoisting cable from the jib to the boom, as labeled in Figure 2.10.

This equation determines how the length of this segment of the hoist cable is changed by the luffing motion. If the total length of the hoist line is held constant, then any change in B is the negative of the change in ℓ. This gives a direct relation between suspension length and luffing rate:

$$\dot{\ell} = \left(\frac{Ar \sin(\Psi - \gamma)}{\sqrt{A^2 + r^2 - 2Ar\cos(\Psi - \gamma)}} \right) \dot{\gamma} \tag{2.27}$$

By multiplying the numerator and denominator by $1/r$, it can be seen that as the ratio of A to r decreases, luffing has a smaller impact on payload suspension length:

$$\dot{\ell} = \left(\frac{A \sin(\Psi - \gamma)}{\sqrt{1 + \frac{A^2}{r^2} - 2\frac{A}{r}\cos(\Psi - \gamma)}} \right) \dot{\gamma} \tag{2.28}$$

In addition to this indirect hoisting being something that is inconvenient to a crane operator, the control of the payload oscillation can become more complicated due to the variation in pendulum suspension length, and therefore payload natural frequency. For example, input-shaping control uses knowledge of system frequency to suppress oscillation. If the pendulum frequency changes during luffing, then input shaping performance could be degraded. The next section will examine this frequency change and other pendulum dynamic properties.

2.3.3 Pendulum Dynamics

In order to analyze the pendulum dynamics, a simpler expression for the radial swing angle ϕ than given in the full nonlinear equation, (2.14), will be determined. By ignoring all inputs except for luffing and assuming no out-of-plane oscillation, the equation of motion for the radial swing is:

$$\ddot{\phi} + \frac{g}{\ell}\sin\phi = \frac{r}{\ell}\left(\ddot{\gamma}\sin(\gamma - \phi) + \dot{\gamma}^2\cos(\gamma - \phi)\right) \tag{2.29}$$

This expression can further be simplified by assuming ϕ is small and the boom luff rate is constant ($\ddot{\gamma} = 0$). While this second assumption is generally not the case unless specifically accounted for (as could easily be seen by taking the time derivative of (2.25)), for the sake of illustration, the assumption is made. Thus,

$$\ddot{\phi} + \frac{g - r\dot{\gamma}^2\sin\gamma}{\ell}\phi = \frac{r}{\ell}\dot{\gamma}^2\cos\gamma \tag{2.30}$$

Table 2.2: Comparison of Luffing Frequency and Pendulum Frequency

Crane Model	r [m]	$\dot{\gamma}_{\text{avg}}$ $\left[\frac{\text{rad}}{\text{s}}\right]$	$\omega_{n,\text{avg}}$ $\left[\frac{\text{rad}}{\text{s}}\right]$
Kobelco CK800-III	61.0	0.029	0.45
Kobelco CK1600-II	76.2	0.025	0.40
Kobelco CK2500-II	91.4	0.017	0.35

This is a linear, homogeneous differential equation with time (or crane-configuration) varying coefficients. If it is further assumed that $g >> r\dot{\gamma}^2 \sin(\gamma)$, then this equation can be further simplified to harmonic oscillator with natural frequency $\omega_n = \sqrt{g/\ell}$ and a forced input, $F = \frac{r}{\ell}\dot{\gamma}^2 \cos\gamma$. This input is the component of the centripetal acceleration in the horizontal direction. Since $\dot{\gamma}$ was assumed constant, γ can be written as $\gamma = \dot{\gamma}t + \gamma_0$. The solution to (2.30) assuming zero initial conditions ($\phi(0) = 0$ and $\dot{\phi}(0) = 0$) is then:

$$\phi = \frac{r\dot{\gamma}^2}{g - \ell\dot{\gamma}^2}\left(\frac{\dot{\gamma}\sin(\gamma_0)}{\omega_n}\sin(\omega_n t) - \cos(\gamma_0)\cos(\omega_n t) + \cos(\dot{\gamma}t + \gamma_0)\right) \tag{2.31}$$

This equation shows that the payload will oscillate at two frequencies: its natural frequency and the luffing rate, $\dot{\gamma}$. However, for most boom crane's, ω_n is much greater than $\dot{\gamma}$. Table 2.2 compares average pendulum natural frequency and luffing frequency for three sizes of boom cranes [7]. Overall, the pendulum natural frequency is over ten times larger than the luffing frequency. Figure 2.11 shows time responses of the pendulum angle from a constant luffing input using the linear approximation in (2.31) and the full nonlinear model in (2.14). Overall a good congruence is shown. The pendulum frequency is clearly present at a period of approximately 3s. The luffing frequency is also present, but only one quarter of it's period is captured in the ten second simulation. Note that ℓ was kept constant for this simulation.

For command filtering vibration control techniques, such as input shaping, the very low luffing frequencies presents a problem because the command delay due to these filters is proportional to the period of oscillation. The very low frequency associated with luffing is therefore difficult to practically control using command filtering techniques.

The conclusions about the payload dynamics to this point are only valid assuming small swing angles, constant luff rates, and $g >> r\dot{\gamma}^2 \sin\gamma$. The third assumption is related to the natural frequency of the pendulum. From (2.31), the loosely-termed "natural frequency" of

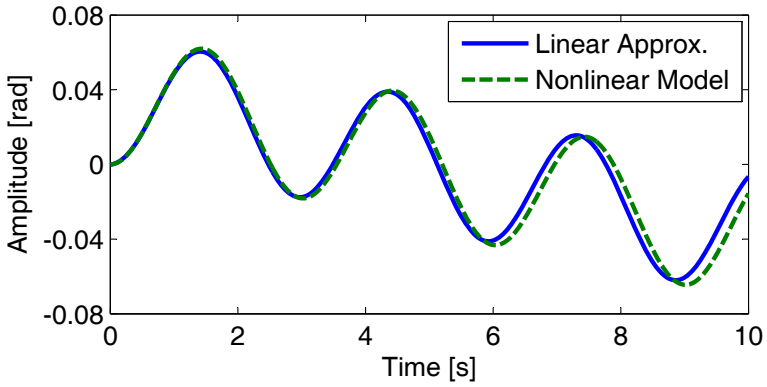

Figure 2.11: Comparison of Linear and Nonlinear Pendulum Responses for Constant Luffing Motion and Payload Suspension Length

the payload without the third assumption is time varying:

$$\omega_n = \sqrt{\frac{g - r\dot{\gamma}^2 \sin\gamma}{\ell(\gamma)}} \tag{2.32}$$

The centripetal acceleration associated with luffing adds a component of acceleration parallel to gravity, effectively reducing the natural frequency of the pendulum for positive luffing and increases the natural frequency if luffing is negative. The change in natural frequency is not constant, but varies sinusoidally with the angle of the boom, as can be seen in (2.32). This effect is clearly visible in the difference between the linear model and nonlinear model responses in Figure 2.11. The nonlinear response has a slightly lower frequency than the linear approximation. This effect on the vertically-accelerated pendulum is the motivation for a more thorough analysis in Section 2.5.

Also note in (2.32) that ℓ is a function of the luff angle as well. This relationship, established in the previous section, can have a much more significant effect on pendulum frequency than centripetal acceleration, depending on the ratio of A to r. To demonstrate this difference, the contributions from centripetal acceleration and cable length changes were calculated throughout the luffing range of a Kobelco CK800 crane [7]. Figure 2.12 plots these contributions for a constant luffing motion from 20° to 78°. The contribution of each effect is normalized to the un-accelerated natural frequency at the beginning of the simulation, ω_{n0}. The centripetal acceleration has a small affect on the natural frequency, only a 0.3% reduction at its maximum at the end of the maneuver. The change in cable

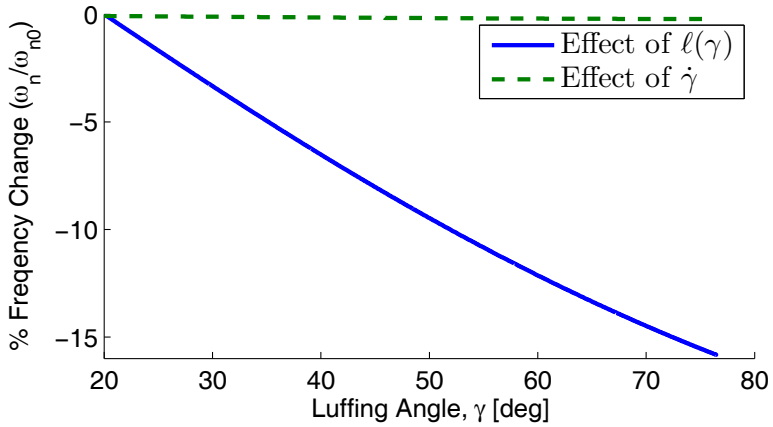

Figure 2.12: Contributions of Centripetal Acceleration and Cable Length Changes on Payload Natural Frequency

length reduces the natural frequency by over 15% by the end of the maneuver.

The horizontal component of centripetal acceleration on the right-hand-side of (2.31) is present even if the boom is not angularly accelerating. This is in stark contrast to a bridge crane or the radial motion of a tower crane in that even a constant velocity input (translation or angular) induces oscillation of the payload. When the boom is accelerated, the dynamics become even more complicated. As can be seen from (2.29), angular acceleration of the boom will impart tangential acceleration on the payload suspension point. Thus, the natural frequency of the payload will also be affected by the vertical component of tangential acceleration.

The important conclusions from this section can be summarized as:

- Natural frequency of the payload swing is affected by luffing rate and angle:
  - Length of pendulum, ℓ, changes with luff angle.
  - Centripetal and tangential acceleration modify the vertical acceleration of the pendulum.
- The payload oscillates at two frequencies, its natural frequency and a frequency equivalent to the luffing rate.
- Even a constant luffing rate induces oscillation of the payload.
- As the ratio of jib length, H, to boom length, r, increases, the effect of the kinematic filter is increased.
- As the ratio of distance along the jib to hoist cable pulley, A, to boom length, r, increases, the influence of luffing on payload suspension length increases.

2.4 Conventional Input Shaping

2.4.1 Luffing Input Shaping

This section will discuss the effectiveness of conventional input-shaping techniques on the luffing motion of boom cranes. Because input shaping is an inexpensive and simple control technique to implement, it would be beneficial if it was effective despite the nonlinear pendulum dynamics presented in the previous section.

One of the largest challenges for implementing input shapers on a boom crane is dealing with a variable hoist length. As discussed in the previous section, the payload suspension length can be altered just by luffing the boom. Combined with the manual hoisting controlled by the operator, the payload suspension length is highly variable. Hence, the payload's natural frequency can vary significantly during operation.

This can cause a problem for input shaping, as significant changes in system natural frequency can degrade a shaper's performance. However, it has been shown that conventional input shapers provide good vibration reduction as the hoisted length changes, particularly if robust shapers are used [52, 34].

To experimentally determine how effective input shaping is on luffing maneuvers, the experimental apparatus pictured in Figure 2.13 was used. The luff input cable is connected to a Siemens Vector Drive motor capable of accurate and fast motions. The boom and

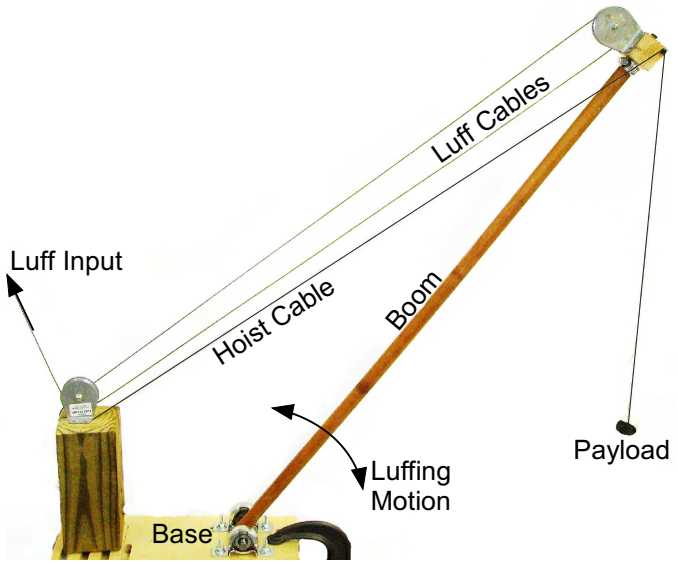

Figure 2.13: Experimental Apparatus for Testing Luffing Maneuvers

Table 2.3: Properties of Luffing Experimental Apparatus

Property		Value	
Boom Length	r	0.89	m
Jib Length	H	0.33	m
Hoist Cable Pulley Point	A	0.29	m
Jib Angle	Ψ	137	deg
Min. Luff Angle	$\gamma_{\min}$	11	deg
Max. Luff Angle	$\gamma_{\max}$	80	deg
Min. Payload Sus. Length	$\ell_{\min}$	0.18	m
Max. Payload Sus. Length	$\ell_{\min}$	0.50	m
Max. Luffing Line Speed	$\dot{C}$	0.12	m/s
Max. Luffing Speed	$\dot{\gamma}_{\max}$	21	deg/s
Average Luffing Speed	$\dot{\gamma}_{\text{avg}}$	15	deg/s

payload were made light-weight so that the torque of the motor could easily lift the payload at all luffing angles. Therefore, the inertia filter described in the previous section can be approximated as unity.

The properties of the luffing apparatus are listed in Table 2.3. The geometry of the jib (H, A, and Ψ) were chosen such that luffing motions will have a significant affect on payload natural frequency. This was done by making the jib length, H, and hoist cable pulley location, A, relatively large in comparison to the boom length r. It was shown in the previous section that as A increases, the effect of luffing on payload suspension length increase, and therefore natural frequency.

The payload suspension length at the minimum luffing angle was chosen such that the payload would rest on the ground. The resulting maximum payload suspension frequency is $\omega_{n,\max} = 7.3$ rad/s. The minimum natural frequency of the payload occurs when the boom is at its maximum luffing angle and the payload suspension length has increased to $\ell_{\max}$. Giving $\omega_{n,\min} = 4.4$ rad/s. The swing of the payload was recorded on a digital video camera and analyzed using machine vision software.

The luffing cable speed was chosen to be $\dot{C} = 0.12$ m/s to give an average luffing speed of $\dot{\gamma}_{\text{avg}}$ =15 deg/s (0.26 rad/s). The ratio of average luffing rate to average payload natural frequency is about equal to that of the commercial cranes listed in Table 2.2.

Four input shapers were evaluated for their effectiveness at suppressing the varying payload oscillation frequency during luffing motion: ZV, ZVD, EI, and SI. Considering

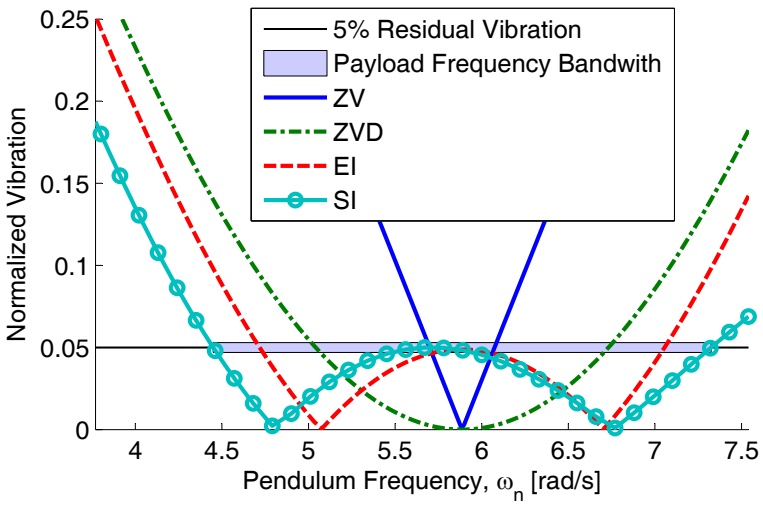

Figure 2.14: Sensitivity Curves for Input Shapers Tested on Luffing Maneuvers

the bandwidth of frequencies exhibited during luffing motions, the ZV, ZVD, and EI input shapers were designed to suppress the middle of the payload frequency bandwidth, $\omega_m = 5.9$ rad/s. The SI input shaper was designed so that vibration is suppressed to 5% of unshaped vibration throughout the entire payload frequency bandwidth.

A plot of the sensitivity curves for each of these input shapers is shown in Figure 2.14. This plot shows the oscillation caused by each input shaper on an undamped oscillatory plant. The vertical vibration axis is normalized by the amount of vibration caused by a unity impulse to the undamped plant. The horizontal axis is the frequency of the system.

It is important to remember that this sensitivity curve is created assuming a linear oscillatory plant. The luffing boom crane is nonlinear, so the vibration levels shown in Figure 2.14 will only approximate the actual oscillation of the payload. An accurate sensitivity curve for an input shaper on a luffing boom crane will be a function of crane geometry, initial luffing angle, luffing duration, and initial payload suspension-length/natural-frequency.

Each input shaper was tested for seven different luffing durations, ranging from 18° to 62°, starting at a luffing angle of 10°. Figure 2.15 shows a plot of the experimental results, along with corresponding theoretical results from the full nonlinear boom crane dynamic model. Overall, the input shaper performance on the luffing maneuver corresponds to the input-shaper sensitivity in Figure 2.14. The most robust shaper, SI, performed the best; while the least robust shaper, ZV, performed the worst.

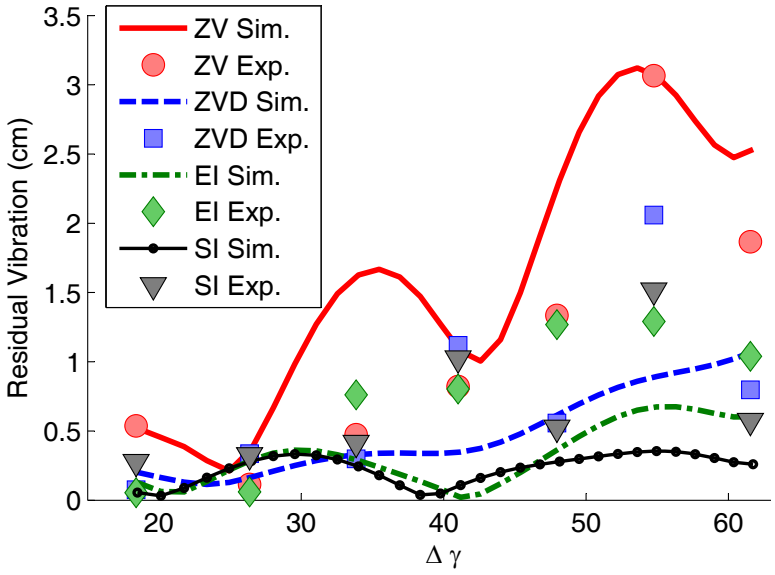

Figure 2.15: Amount of Residual Vibration for Luffing Maneuvers of Varying Luffing Durations

The experimental data points do not match the theoretical curves as well as would be expected. The main reason for this discrepancy lies in the uncertainty in the initial conditions of the experiment, and the data collection system. The initial swing of the payload before the experiment is impossible to eliminate entirely. Compared to the amount of residual vibration expected in the theoretical curves (around 0.5 cm), the amount of initial oscillation in the payload is significant, and could play a significant role in the actual residual vibration recorded.

A second reason for the discrepancy in the experimental data lies in the data recording system. At small amounts of residual oscillation, the resolution of the digital camera and the uncertainty in the machine vision software leads to noise in the experimental data.

The biggest disadvantage to using input shaping is the rise-time delay of the system caused by the input-shaping process. One way to reduce this delay on luffing maneuvers is to not input-shape portions of the command at small luffing angles and input shape the command at higher luffing angles. The reasoning for this comes from the dynamic analysis presented in section 2.3. At small luffing angles, the amount of horizontal acceleration on the payload is small. Therefore, input shaping is not as necessary. Figure 2.16 shows an example of this kind of luffing command for an Unshaped-ZV combination.

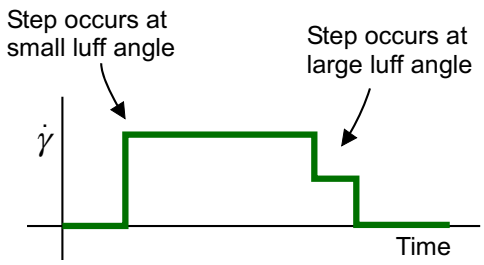

Figure 2.16: Velocity Profile of Proposed Luffing Maneuver

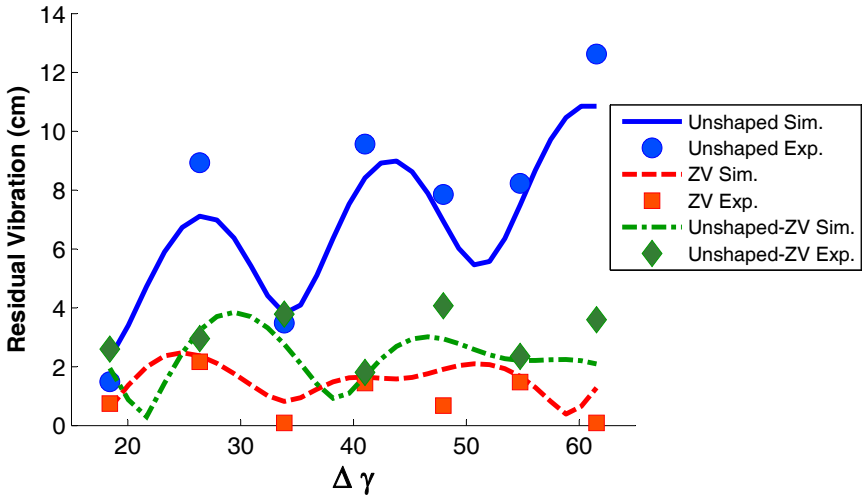

Figure 2.17: Velocity Profile of Proposed Luffing Maneuver

Experimental and simulation results for this command profile are shown in Figure 2.17. Results for unshaped commands and standard ZV-shaped commands are shown for comparison. The residual vibration of this style command is slightly higher than the standard ZV command, as would be expected, but still far less than the unshaded command. Depending on the application, this slightly higher amount of residual vibration could be an acceptable trade-off for shorter rise-time delays.

Another observation from these experimental results in Figure 2.17 is that they match the theoretical results better than those in Figure 2.15. Because the amount of vibration expected is greater, the experiments match the theory much better. This confirms the reasoning for the poor matching of experimental results in Figure 2.15.

2.4.2 Luffing Slewing Combination

As difficult as it is to predict the effectiveness of input-shaping on luffing maneuvers alone, the effectiveness of luffing and slewing simultaneously is even more difficult. Some research

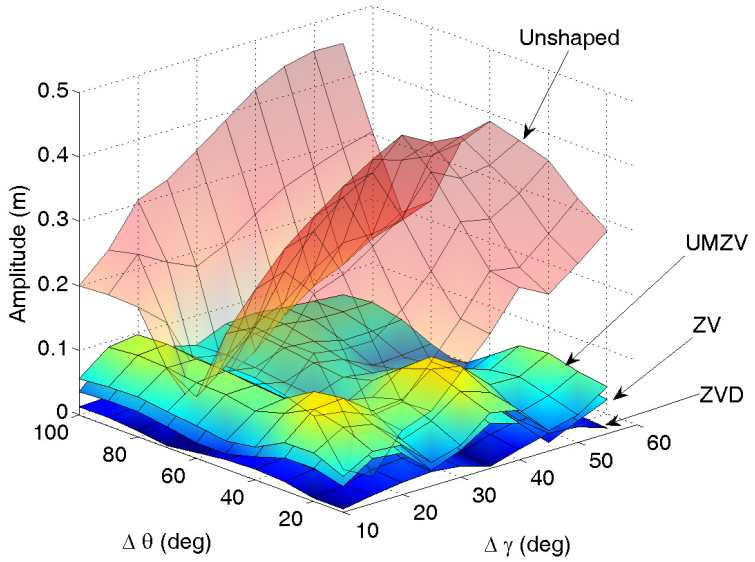

Figure 2.18: Input Shaping Performance for Luffing and Slewing Motions

has been done on the effectiveness of input shaping on pure slewing maneuvers [6, 25]. This research was done for the purpose of improving control of tower cranes. It was shown that ZVD was the most effective input shaper tested.

To determine how effective input shaping is on luffing-slewing combination maneuvers, a series of simulations were conducted for numerous slewing and luffing maneuvers; each of various duration. Figure 2.18 shows the results of these simulation. The vertical axis shows the residual vibration after each move was completed. The two horizontal axis are the length of the luffing ($\Delta\gamma$) and slewing ($\Delta\theta$) portion of each maneuver. Over the entire range of maneuvers, all input shapers are effective at reducing vibration. As expected though, the more robust shapers perform better at reducing vibration. Figure 2.19 shows the residual vibration for the ZV and ZVD input shapers. From this plot it can be seen that the ZVD is much more effective than the less robust ZV input shaper.

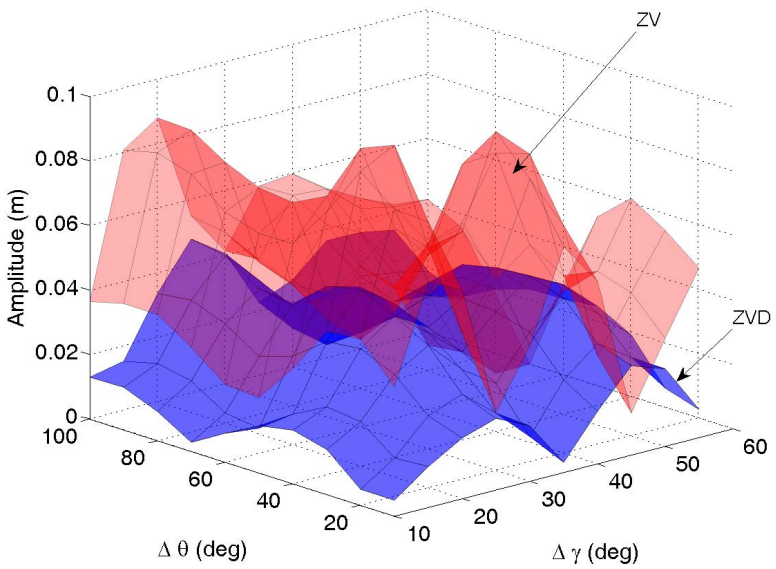

Figure 2.19: ZV and ZVD Performance for Luffing and Slewing Motions

2.5 Vertically Accelerated Pendulums

The pendulum is a widely studied physical system [5, 41, 40]. Although the pendulum is a nonlinear system, for small swing angles and a fixed suspension point, its natural frequency can be approximated as:

$$\omega_n = \sqrt{\frac{g}{L}} \tag{2.33}$$

where g is the acceleration due to gravity and L is the suspension length of the pendulum.

The motion of simple pendulums and variants, including spherical, vertical, and double pendulums have been widely studied. One that has not been widely studied is that of a pendulum undergoing vertical acceleration. Price[35] and Rowland[37] examined the effects of a pendulum in a uniformly accelerating field, but their analysis was from the viewpoint of special relativity and not relevant to engineering applications.

This section examines the effect of vertical acceleration on pendulum dynamics for the purpose of controlling oscillation in practical applications. Steps and pulses in vertical acceleration will be examined in detail because of their relevance to engineering applications. It will be shown that not only is pendulum frequency altered by vertical acceleration, but its amplitude and phase can also be affected.

2.5.1 Background

The equation of motion for a simple pendulum with a massless rod, zero damping, and constant suspension length is given by:

$$\ddot{\theta} + \frac{g}{L}\sin(\theta) = 0 \tag{2.34}$$

Where θ is the angle of the pendulum. The approximate natural frequency in (2.33) is determined from the linearization of this equation.

When the pendulum undergoes vertical acceleration the equation of motion is given by:

$$\ddot{\theta} + \frac{g + \ddot{z}}{L}\sin(\theta) = 0 \tag{2.35}$$

where $\ddot{z}$ is the magnitude of vertical acceleration. Using the same linearization method used for ω_n in (2.33), the natural frequency of the vertically accelerated pendulum is [14]:

$$\omega_a = \sqrt{\frac{g + \ddot{z}}{L}} \tag{2.36}$$

This result is consistent with the *equivalence principal* that states that an observer is unable to distinguish between gravity in an inertial reference frame and zero gravity in an accelerating frame.

By using small angle approximations and assuming $\ddot{z}$ is constant, (2.35) can be linearized and an approximation for $\theta(t)$ is:

$$\theta(t) = \frac{\dot{\theta}(0)}{\omega}\sin(\omega t) + \theta(0)\cos(\omega t) \tag{2.37}$$

Where the subscript is left off of ω to indicate that it can be either ω_n or ω_a. This response will be use throughout this section to construct pendulum responses to steps and pulses in vertical acceleration.

While (2.36) approximates the pendulum's natural frequency as it is vertically accelerated, in engineering applications, a constant uniform acceleration rarely occurs over long durations. More common in engineering applications are step and pulse inputs of vertical acceleration. Section 2.5.2 presents an experimental validation of (2.36) for a step in vertical acceleration. Section 2.5.3 examines how the timing of a step in vertical acceleration affects

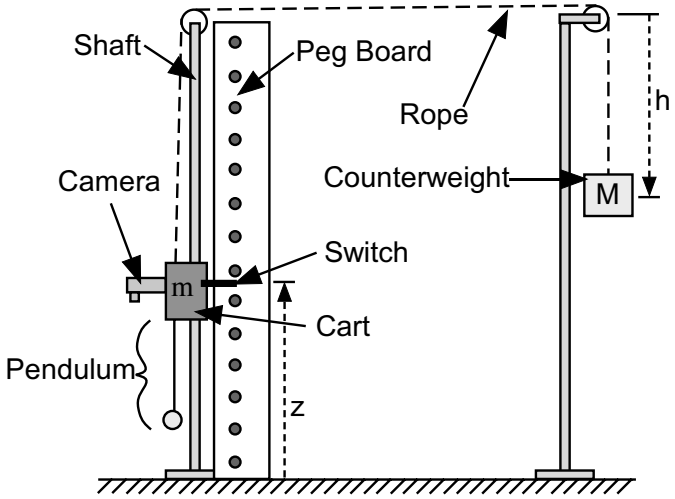

Figure 2.20: Experimental Apparatus

the pendulum's frequency and amplitude. It will be shown that a step applied at the proper time can reduce the amplitude of the pendulum's oscillation. Section 2.5.4 examines pulses in acceleration. It will be shown that not only amplitude and frequency are altered by a pulse input, but the steady-state phase can also change. Pulse switch times that reduce the steady-state pendulum amplitude will be derived.

2.5.2 Experimental Verification

To test the approximation resulting in (2.36), the experimental apparatus diagramed in Figure 2.20 was constructed to measure pendulum oscillation frequency when a step in vertical acceleration is applied. The apparatus consists of a cart that slides on linear bearings along a vertical shaft. The position of the cart is z. The range of cart motion is $z = 0$ to $z = 1.3$m. A pendulum is attached to the bottom of the cart. A camera is also attached to the cart that records the response of the pendulum. Attached to the top of the base is a rope that is attached to a counterweight of mass M. The vertical position of the counterweight is h. Finally, a limit switch is attached to the cart to record the position of the cart. As it is accelerated, the switch is pulsed on when it passes over the pegs on the peg board. These pulses give the position response, $z(t)$. The combined mass of the cart, camera, switch, and pendulum is m.

To test positive vertical accelerations, the cart is lowered to the bottom of the shaft

Table 2.4: Physical Parameters Used in Experiment

$\ddot{z}_{avg}/g$	ω_a/ω_n	L [m]	b [Ns/m]	m [kg]	M [kg]
-0.19	0.95	0.17	4	2	1.2
-0.17	0.98	0.17	1	2	1.3
0.00	1	0.17	–	2	2.0
0.04	1.02	0.17	1	2	2.9
0.06	1.05	0.17	5	2	3.1
0.11	1.08	0.17	9	2	3.4

($z = 0$) and correspondingly $h = 0$. The counterweight mass, M, is chosen so that $M > m$. The pendulum is given an initial swing and then the counterweight is released so that the pendulum cart accelerates upward. The magnitude of vertical acceleration is changed by adjusting the counterweight mass. Testing negative accelerations are completed similarly by adjusting $M < m$ and releasing the pendulum at the top of the shaft ($z = 1.3$m).

The limit switch/peg board approach was used because an accelerometer did not provide accurate data to measure the small accelerations present in this experiment. Because the limit switch measures the time response, not the vertical acceleration, $\ddot{z}$ is determined by differentiating the position response.

The equation of motion of the moving cart assuming viscous damping and negligible rope and pendulum mass is:

$$\ddot{z} + \frac{b}{m}\dot{z} = -\frac{M+m}{m}g \tag{2.38}$$

where b is the damping coefficient. For $b \neq 0$ and $\dot{z}(0) = 0$, the solution to this equation is:

$$z(t) = \frac{d}{a^2}\left(e^{-at} + at - 1\right) + z(0) \tag{2.39}$$
$$a = \frac{b}{M+m} \qquad d = \frac{M-m}{M+m}g$$

Because the acceleration, $\ddot{z}$, is not constant in (2.39), the average value of the function over the duration of the acceleration is used:

$$\ddot{z}_{avg} = \frac{1}{t_f - t_0}\int_{t_o}^{t_f} \frac{d^2 z(t)}{dt^2} dt = \frac{d}{at_f}\left(1 - e^{-at_f}\right) \tag{2.40}$$

Every variable in this equation is known except for the damping coefficient, b. It was experimentally determined by performing a least-squares minimization between (2.39) and the experimental response from the limit switch data. Table 2.4 lists the numerical values for

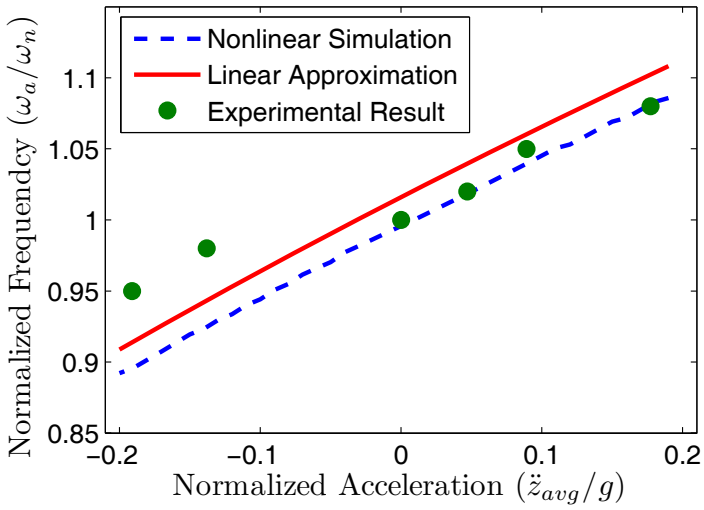

Figure 2.21: Pendulum Frequency as a Function of Vertical Acceleration

each parameter for each experimental point. The variance in the magnitude of the damping coefficient is most likely attributed to un-modeled nonlinear dynamics of the linear-motion bearings.

A plot of pendulum frequency versus acceleration magnitude is shown in Figure 2.21. The dotted line is the frequency determined from a nonlinear simulation of (2.35) the pendulum's period. This frequency was determined from the period of oscillation, calculated by measuring the time between zero-crossings of the response. The solid line is the linear approximation for natural frequency defined by (2.36). The experimental results are shown as circles.

One important result shown by this figure is that the linear approximation of the frequency follows very closely to the full nonlinear result. This fact will allow us to safely assume that the linear approximation for ω_a is valid. The experimental results also match the theoretical results fairly well. However, the experimental points for $\ddot{z} < 0$ differ from the theory more than the cases when $\ddot{z} > 0$. This difference arises because the period of the pendulum increases as acceleration decreases. Therefore, the camera needs to record more of the time response of the pendulum to accurately determine the oscillation frequency. Because only a limited experimental range for z is available, accurate measurement of the frequency is more difficult for $\ddot{z} < 0$.

Another important result from Figure 2.21 is the amount of frequency change that can result from a small amount of acceleration. From the figure, a $0.1g$ vertical acceleration will increase the frequency by 5%. This increase is significant for some vibration control techniques that depend on knowledge of the pendulum frequency.

Positive vertical accelerations are limited by the actuators of whatever machine is raising the pendulum, effectively limiting the amount of positive vertical acceleration that the pendulum can experience. Negative vertical accelerations, however, have no such constraint and can easily approach free fall. As vertical acceleration is decreased to free fall ($\ddot{z} = -1g$), the pendulum frequency approaches zero. As this scenario is more likely, these frequency changes become more significant. For example, a high-speed crane that quickly picks up and drops a payload experiences pendulum frequency change. If the payload is lowered with significant acceleration, then the frequency drops significantly and should be accounted for in the control system design.

2.5.3 Effects of Varying Step Time

As seen previously, the amplitude of a step in vertical acceleration affects the frequency of a pendulum. In this section, the time at which the step is applied, relative to the pendulum's instantaneous swing angle, will be shown to affect the amplitude of vibration. An approximation of the response of the pendulum after the step has occurred can be determined by concatenating solutions for the unaccelerated and accelerated pendulum using (2.37). By using the final condition of the unaccelerated swing of the pendulum as the initial condition of the accelerated swing (i.e. equating the boundary conditions), $\theta(t)$ is:

$$\theta(t) = A_s \cos(\omega_a t - \phi_s) \tag{2.41}$$

Where:

$$A_s = \sqrt{B_1^2 + B_2^2} \tag{2.42}$$

$$\phi_s = \tan^{-1}\left(\frac{B_1}{B_2}\right) \tag{2.43}$$

and,

$$B_1 = \frac{\dot{\theta}_0 \cos(\omega_n t_s) - \theta_0 \sin(\omega_n t_s)}{\omega_a} \tag{2.44}$$

$$B_2 = \frac{\dot{\theta}_0}{\omega_n} \sin(\omega_n t_s) + \theta_0 \cos(\omega_n t_s) \tag{2.45}$$

Note that for calculation purposes, the four quadrant $\tan^{-1}$ function should be used.

Without loss of generality, (2.41) can be simplified by setting $t_s = t_0 = 0$ and adjusting the initial conditions $\dot{\theta}_0$ and θ_0 accordingly:

$$\theta(t)\Big|_{t_s=0} = \sqrt{\frac{\dot{\theta}_0^2}{\omega_a^2} + \theta_0^2} \cos\left(\omega_a t - \tan^{-1}\left(\frac{\dot{\theta}_0/\omega_a}{\theta_0}\right)\right) \tag{2.46}$$

From this equation it is easy to see that the amplitude of the accelerated step response can be altered by choosing the appropriate initial conditions. This is equivalent to choosing the switch time t_s relative to the angle of the pendulum swing.

In engineering applications, it is often useful to limit the amount of vibration in a pendulum swing. To determine what initial conditions minimize the accelerated amplitude for a given magnitude of vertical acceleration, it is useful to examine the energy balance of the pendulum before vertical acceleration is applied:

$$mgL\,(1 - \cos\beta) = mgL\,(1 - \cos\theta) + \frac{1}{2} mL^2 \dot{\theta}^2 \tag{2.47}$$

Where β is the maximum angle in the pendulum swing before vertical acceleration is applied. This equation provides a relationship between $\dot{\theta}_0$ and θ_0. Since it is valid at all time, including $t = 0$, this equation can be solved for $\dot{\theta_0}^2$:

$$\dot{\theta_0}^2 = 2\omega_n^2\,(\cos\theta_0 - \cos\beta) \tag{2.48}$$

This result can be substituted into the amplitude of (2.46) to yield a cost function for the pendulum amplitude as a function of θ_0:

$$A_{\text{step}} = \sqrt{\frac{2g}{g + \ddot{z}}\,(\cos\theta_0 - \cos\beta) + \theta_0^2} \tag{2.49}$$

To minimize this equation, the derivative with respect to θ_0 of the term in the square root is set equal to zero to yield an optimal condition for θ_0:

$$\sin\theta_0 = \frac{g + \ddot{z}}{g}\theta_0 \tag{2.50}$$

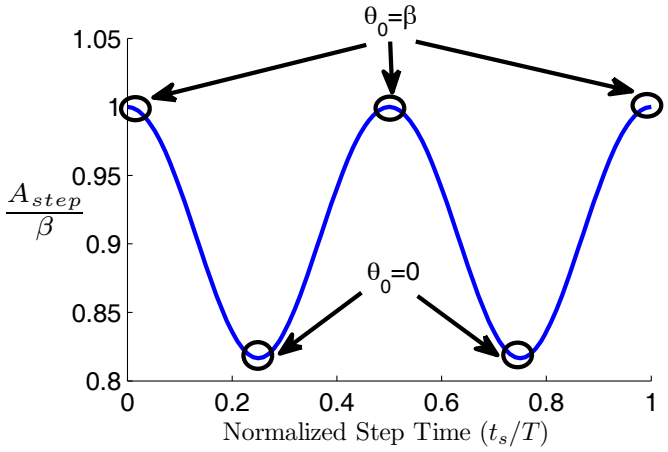

Figure 2.22: Variation in Response Amplitude and Phase Versus Step Switch Time

Because this equation was derived using the small angle approximation first used in (2.37), to determine applicable solutions to (2.50), small angles must again be assumed. This yields a single solution for the initial condition of the pendulum to yield an optimally small swing amplitude: $\theta_0 = 0$ and $\dot{\theta}_0 = \beta\omega_n$. In turn, the amplitude of the response given by (2.46) is:

$$A_{\text{step}} = \beta\frac{\omega_n}{\omega_a} = \frac{\dot{\theta}_0}{\omega_a} \tag{2.51}$$

This result implies that a positive step in vertical acceleration, applied at $\theta = 0$, will yield a minimum amplitude of response. The amount of reduction depends on the magnitude of $\ddot{z}$. The greater $\ddot{z}$, the greater the reduction in pendulum oscillation amplitude. A negative step in vertical acceleration applied at $\theta = 0$ will have the opposite effect. It will increase the magnitude of the accelerated response.

To illustrate how step time, t_s, affects the response of the pendulum, step inputs of positive vertical acceleration were simulated under the following conditions:

$$\begin{aligned} \ddot{z} &= 0.5g\text{H}\left(t - t_s\right) \qquad t_s = 0, 0.05T, ..., T \\ \theta_0 &= \beta = \frac{\pi}{6} \qquad \dot{\theta}_0 = 0 \end{aligned} \tag{2.52}$$

The resulting oscillation amplitude is plotted against switch time, t_s, in Figure 2.22. The amplitude axis is normalized against the unaccelerated amplitude, β. Note that the maximum reduction in amplitude occurs at $t_s = T/4$ and $3T/4$. These points are labeled in the figure as $\theta_0 = 0$, highlighting what was predicted by (2.50). The amplitude is not affected

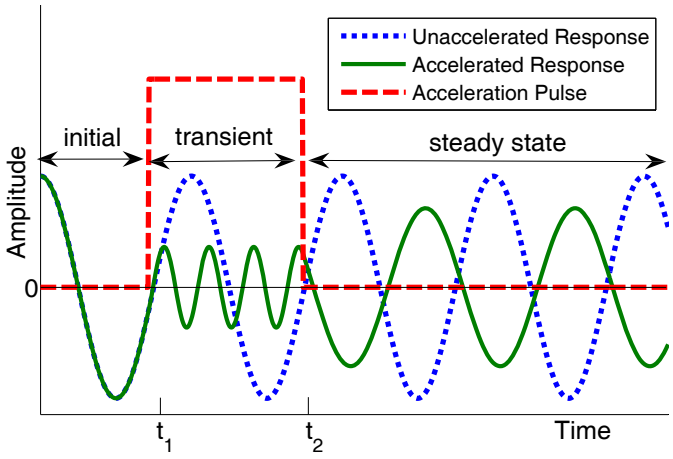

Figure 2.23: Effect of a Pulse in Acceleration on Steady State Pendulum Response

when the pendulum is at the apex of its swing ($t_s = 0, T/2, T$ and $\dot{\theta}_0 = 0$) as can be seen from (2.46). These points are labeled as $\theta_0 = \beta$.

2.5.4 Pulses in Acceleration

Although steps in acceleration are useful for understanding fundamental effects, pulse inputs in acceleration are a more common occurrence. A plot of a response that exemplifies the properties of a pulse response is shown in Figure 2.23. In the figure, the pendulum has an initial swing in the zone labeled *initial*. When the acceleration pulse is applied during the *transient* zone, starting at t_1 and ending at t_2, the frequency and amplitude of the pendulum changes as predicted by (2.41). The portion of the response of most interest occurs when the pendulum returns to its unaccelerated state, labeled *steady-state*. From the figure it is clear that the amplitude and phase of the pendulum swing changes from its original conditions. The amount of phase shift and amplitude change is a function the pulse duration, the time at which the pulse is applied to the pendulum, and the magnitude of the acceleration pulse.

In order to simplify the expression for the steady-state response of the pendulum, the initial phase of the pendulum is eliminated by setting $t_1 = 0$. This can be done without loss of generality, as was done with a step response, by adjusting the initial condition of the pendulum. Then, by using the same piecewise technique used for a step in vertical

acceleration, the steady-state response of the pendulum subject to a pulse is:

$$\theta_{\text{ss}}(t) = A_p \cos\Big(\omega_n t - (\phi_p + \omega_n t_2)\Big) \tag{2.53}$$

Where:

$$A_{\text{pulse}} = \sqrt{\left(\frac{\dot{\theta}(t_2)}{\omega_n}\right)^2 + \theta(t_2)^2} \tag{2.54}$$

$$\phi_p = \tan^{-1}\left(\frac{\dot{\theta}(t_2)/\omega_n}{\theta(t_2)}\right) \tag{2.55}$$

And

$$\theta(t_2) = \sqrt{\frac{\dot{\theta}_0^2}{\omega_a^2} + \theta_0^2}\cos\left(\omega_a t_2 - \tan^{-1}\left(\frac{\dot{\theta}_0/\omega_a}{\theta_0}\right)\right) \tag{2.56}$$

$$\dot{\theta}(t_2) = -\omega_a\sqrt{\frac{\dot{\theta}_0^2}{\omega_a^2} + \theta_0^2}\sin\left(\omega_a t_2 - \tan^{-1}\left(\frac{\dot{\theta}_0/\omega_a}{\theta_0}\right)\right) \tag{2.57}$$

It was shown in the previous section that a step in vertical acceleration, applied at the appropriate time, could reduce the amplitude of response. If a pulse is analyzed as a series of two steps, then the pulse times t_1 and t_2 that minimize oscillation amplitude can be determined relatively easily.

First, consider a positive pulse in acceleration that consists of a positive step followed by a negative step. According to (2.51), the amplitude reduction of a positive step in acceleration is reduced by choosing a step time corresponding to $\theta = 0$. A negative step can maintain amplitude only if the step time occurs at the apex of the pendulum's swing; otherwise amplitude is increased. Therefore t_1 and t_2 should be chosen to meet these conditions:

$$t_1 \quad \text{so that} \quad \theta(t_1) = 0$$

$$t_2 = t_1 + \frac{n\pi}{2\omega_a} \quad n = 0, 1, 3, 5, \ldots \tag{2.58}$$

If these step times are inserted into (2.53), then the response of an oscillation-minimizing pulse can be simplified to:

$$\theta_{\text{ss}}(t) = \beta\frac{\omega_n}{\omega_a}\cos(\omega_n(t - t_2)) \tag{2.59}$$

This response shows a reduction in amplitude by a factor of ω_n/ω_a and a phase lag of $\omega_n t_2$.

A negative pulse in acceleration is the logical opposite of a positive pulse in acceleration. Accordingly, t_1 should be chosen so that $\theta(t_1) = \beta$ and t_2 so that $\theta(t_2) = 0$. Therefore, the optimal time for t_2 is also given by (2.58). The steady state response for this case can be simplified to:

$$\theta_{\text{ss}}(t) = -\beta \frac{\omega_a}{\omega_n} \sin(\omega_n(t - t_2)) \tag{2.60}$$

This result shows that both positive and negative pulses in vertical acceleration can be used to reduce the amplitude of pendulum vibration.

To summarize, this section examined how vertical acceleration affects the dynamic response of a pendulum. It was shown that the frequency, amplitude, and phase of a pendulum can be altered when a vertical acceleration occurs. Experimental results were obtained to support the frequency shift that occurs under vertical acceleration. Because of their utility in engineering applications, step and pulse inputs of vertical acceleration were examined in detail. A positive step in vertical acceleration was found to reduce pendulum oscillation amplitude if it is applied when the pendulum is near the bottom of its swing. A negative step can only increase oscillation amplitude except if the step is applied when the pendulum is at the apex of its swing, in which case amplitude is unaffected. Pulses in vertical acceleration were shown to change the steady-state amplitude and phase of oscillation. By analyzing the pulse as a series of two steps in vertical acceleration, it was shown that both a positive and negative pulse in acceleration can reduce the amplitude of pendulum oscillation.

CHAPTER III

CARTESIAN BOOM AND TOWER CRANE CONTROL STRATEGY

This chapter describes a method for transforming the actuation of cranes from their joint space to Cartesian space. Boom cranes are naturally described and actuated in spaces that are defined by spherical coordinate systems. That is, moving the crane with one of its actuators results in a rotational, rather than straight line motion, of the crane payload. In order for human operators to drive these cranes to a desired location, they must convert the desired horizontal and vertical motion into appropriate rotational motions. This can be a difficult transformation, especially when there are obstacles in the workspace. Furthermore, when operators manipulate the crane by remote control or by standing on the ground, they do not rotate along with the crane. In these cases, they must transform their commands through a rotating reference frame. This complex coordinate transformation is not natural or user friendly to a stationary operator. It would be beneficial to the operate the crane in Cartesian coordinates. That is, by giving commands that correspond to right, left, forward, reverse, up, and down.

Cartesian motion control of non-rectilinear machines is not a new idea. Most commonly, it is an area of research in robotics [8, 2, 4]. However, this chapter presents a new technique in the area of boom and tower crane control and its flexible dynamics. The boom crane will be used to develop the concepts in the chapter, but implementation on tower cranes will be discussed at the conclusion of the discussion.

3.1 Cartesian Coordinate Transformation

This section outlines a method that transforms Cartesian motions given by a human operator into motions that are natural to a boom crane and its inherent spherical coordinates. Figure 3.1 shows a simplified coordinate system that describes the position of a boom crane

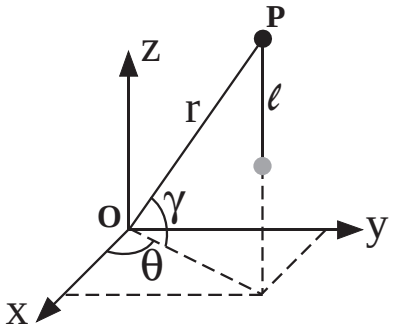

Figure 3.1: Spherical Coordinates of Boom Crane

payload in Cartesian (x, y and z) and spherical coordinates (γ, θ and ℓ)[1]. The two coordinate systems are related by the following three equations:

$$x = r\cos\gamma\cos\theta \tag{3.1}$$

$$y = r\cos\gamma\sin\theta \tag{3.2}$$

$$z = r\sin\gamma - \ell \tag{3.3}$$

It is assumed here that there is no payload sway so that the payload is directly below the hook. The time derivative of these equations is:

$$\begin{bmatrix} \dot{x} \\ \dot{y} \\ \dot{z} \end{bmatrix} = \begin{bmatrix} -r\sin\gamma\cos\theta & -r\cos\gamma\sin\theta & 0 \\ -r\sin\gamma\sin\theta & r\cos\gamma\cos\theta & 0 \\ -r\cos\gamma & 0 & -1 \end{bmatrix} \begin{bmatrix} \dot{\gamma} \\ \dot{\theta} \\ \dot{\ell} \end{bmatrix} \tag{3.4}$$

$$\{\dot{\mathbf{x}}_c\} = T^{-1}\{\dot{\mathbf{x}}_s\} \tag{3.5}$$

Where T^{-1} is the Jacobian of the coordinate transformation, $\{\mathbf{x}_c\}$ is the vector of Cartesian coordinates, and $\{\mathbf{x}_s\}$ is the vector of spherical coordinates. We are looking for the transformation from Cartesian to spherical, so both sides of (3.5) can be left-multiplied by

[1] Although this coordinate system is not a conventional spherical coordinate system, it will be called that in this chapter because of its similarity to one.

T to get:

$$\begin{bmatrix} \dot{\gamma} \\ \dot{\theta} \\ \dot{\ell} \end{bmatrix} = \begin{bmatrix} -\frac{\cos\theta}{r\sin\gamma} & -\frac{\sin\theta}{r\sin\gamma} & 0 \\ -\frac{\sin\theta}{r\cos\gamma} & \frac{\cos\theta}{r\cos\gamma} & 0 \\ \frac{\cos\theta}{\tan\gamma} & \frac{\sin\theta}{\tan\gamma} & -1 \end{bmatrix} \begin{bmatrix} \dot{x} \\ \dot{y} \\ \dot{z} \end{bmatrix} \tag{3.6}$$

$$\{\dot{\mathbf{x}}_s\} = T\{\dot{\mathbf{x}}_c\} \tag{3.7}$$

To ensure that T has an inverse, it must be shown that it is invertible for all points in the boom crane workspace. Taking the determinate of T^{-1} yields:

$$\det\left(T^{-1}\right) = \frac{1}{2}r^2 \sin 2\gamma \tag{3.8}$$

From this equation it is easy to see that the transformation is undefined for $\gamma = \{0, \frac{\pi}{2}\}$. So this transformation will be valid within this range. For a boom crane, this condition is easily avoided because cranes are rarely operated with the boom perfectly horizontal ($\gamma = 0$) or vertical ($\gamma = \frac{\pi}{2}$).

Because of the transcendental nature of transformation matrix, T, it is useful to know if the transformation is one-to-one. However, this has already been guaranteed because the transformation is invertible. Invertibility guarantees that a linear transformation is one-to-one. In this case, as long as $\gamma \neq \{0, \frac{\pi}{2}\}$.

By examining the equation for the suspension length in (3.6), there is coupling between x and y motion of the crane and the vertical motion of the payload, $\dot{\ell}$. That is, without compensation, the vertical position of the payload suspension point will be changed by horizontal motions of the payload. This indirect motion will have to be accounted for in the final control law for the hoist cable.

To summarize, the Jacobian matrix T defines the relationship between Cartesian motions and spherical motions. By examining (3.6) it can be seen that the transformation only depends on the current geometry of the crane: θ and γ. This matrix will be used to convert desired Cartesian motions into spherical motions that can then be sent to the crane actuators. This type of Cartesian motion control when applied to robots is called Jacobian inversion [8].

3.2 Actuation

This section describes how to account for the actuation of the boom crane in the Cartesian coordinate transformation. As was discussed in Section 2.3, the luffing speed for the majority of boom cranes is not directly controlled. In general, the luffing speed is the function of the actuator effort and the configuration of the crane. For the crawler boom crane diagramed in Figure 2.10 on page 22, the relationship between the luffing cable speed, $\dot{C}$, and the luffing speed, $\dot{\gamma}$, was shown to be:

$$\dot{C} = -\left(\frac{Hr\sin(\Psi-\gamma)}{\sqrt{H^2+r^2-2Hr\cos(\Psi-\gamma)}}\right)\dot{\gamma} \tag{3.9}$$

This equation was part of the kinematic filter discussed in Section 2.3. Also discussed in that section was how luffing also indirectly affects the payload suspension length:

$$\dot{\ell} = \left(\frac{Ar\sin(\Psi-\gamma)}{\sqrt{A^2+r^2-2Ar\cos(\Psi-\gamma)}}\right)\dot{\gamma} \tag{3.10}$$

In addition to this indirect hoisting, the hoist line can be actively adjusted by the operator. Consider the hoist line speed that is controlled by the crane operator to be $\dot{L}$. By combining the direct and indirect hoisting, the total suspension length speed is then:

$$\dot{\ell} = \dot{L} + \frac{Ar\sin(\Psi-\gamma)}{\sqrt{A^2+r^2-2Ar\cos(\Psi-\gamma)}}\dot{\gamma} \tag{3.11}$$

Combining the the relationshipes in (3.9) and (3.11) into one transformation matrix, V, yields:

$$\begin{bmatrix}\dot{C}\\ \dot{\theta}\\ \dot{L}\end{bmatrix} = \begin{bmatrix}\frac{-Hr\sin(\Psi-\gamma)}{\sqrt{H^2+r^2-2Hr\cos(\Psi-\gamma)}} & 0 & 0\\ 0 & 1 & 0\\ \frac{-Ar\sin(\Psi-\gamma)}{\sqrt{A^2+r^2-2Ar\cos(\Psi-\gamma)}} & 0 & 1\end{bmatrix}\begin{bmatrix}\dot{\gamma}\\ \dot{\theta}\\ \dot{\ell}\end{bmatrix} \tag{3.12}$$

$$\{\dot{\mathbf{x}}_a\} = V\{\dot{\mathbf{x}}_s\} \tag{3.13}$$

Where $\{\mathbf{x}_a\}$ are the coordinates that are natural to the crane actuators and $\{\mathbf{x}_s\}$ are the spherical coordinates that are natural in motion analysis. In the Cartesian motion transformation being developed in this chapter, $\{\mathbf{x}_s\}$ is defined by the coordinate transformation

from Cartesian to spherical coordinates. By combining both transformations, T and V, the total coordinate transformation can be defined as:

$$\begin{bmatrix} \dot{C} \\ \dot{\theta} \\ \dot{L} \end{bmatrix} = \begin{bmatrix} \frac{H\sin(\Psi-\gamma)\cos\theta}{\sqrt{H^2+r^2-2Hr\cos(\Psi-\gamma)}\sin\gamma} & \frac{H\sin(\Psi-\gamma)\sin\theta}{\sqrt{H^2+r^2-2Hr\cos(\Psi-\gamma)}\sin\gamma} & 0 \\ -\frac{\sin\theta}{r\cos\gamma} & \frac{\cos\theta}{r\cos\gamma} & 0 \\ \frac{A\sin(\Psi-\gamma)\cos\theta}{\sqrt{A^2+r^2-2Ar\cos(\Psi-\gamma)}\sin\gamma}+\frac{\cos\theta}{\tan\gamma} & \frac{A\sin(\Psi-\gamma)\sin\theta}{\sqrt{A^2+r^2-2Ar\cos(\Psi-\gamma)}\sin\gamma}+\frac{\sin\theta}{\tan\gamma} & -1 \end{bmatrix} \begin{bmatrix} \dot{x} \\ \dot{y} \\ \dot{z} \end{bmatrix} \tag{3.14}$$

This equation defines a transformation from Cartesian space to actuation space of a crawler style boom crane. Similar expressions can be developed for other boom cranes, such as the hydraulic style boom crane. To do this, a different V matrix must be developed and then combined with the Jacobian transformation matrix T.

3.3 Saturation

This section describes a method to compensate for actuator saturation that naturally arises from the Cartesian coordinate transformation. The problem occurs when certain velocity commands in Cartesian space are impossible to reproduce in actuator space. If this saturation problem is not addressed, undesirable motion of the crane will result.

Because the transformation matrix T is singular at $\gamma = \{0, \frac{\pi}{2}\}$, it will also become nearly singular at values of γ approaching these limits. Cartesian trajectories that cause the crane to operate near this singular point will require high velocities in the spherical coordinates, $\{\mathbf{x}_s\}$, to maintain desired Cartesian velocities, $\{\mathbf{x}_c\}$. Assume that there exists angular velocity limits on γ and θ:

$$\max(\dot{\gamma}) = \dot{\gamma}_{\max} \tag{3.15}$$

$$\max(\dot{\theta}) = \dot{\theta}_{\max} \tag{3.16}$$

From (3.6) it is clear that as $\gamma \to 0$, $\dot{\gamma} \to \infty$. Likewise, as $\gamma \to \frac{\pi}{2}$, $\dot{\theta} \to \infty$. Therefore, when the crane's boom is near vertical, $\dot{\theta}$ will approach its physical limit and as the boom is near horizontal, $\dot{\gamma}$ will approach its limit.

To determine how the inputs should be scaled to prevent saturation, a special case of motion only in the x direction will be examined. Assume for a moment that the crane is

only near the case where the slewing motor ($\dot{\theta}$) is close to saturation. The transformation equation (3.6) simplifies to:

$$\begin{bmatrix} \dot{\gamma} \\ \dot{\theta} \end{bmatrix} = \begin{bmatrix} -\frac{\cos\theta}{r\cos\gamma} \\ -\frac{\sin\theta}{r\cos\gamma} \end{bmatrix} \dot{x} \tag{3.17}$$

If the slewing motor is saturating, then it is known that the desired motion, $\dot{x}$, and the current geometry of the crane require a faster slewing speed, $\dot{\theta}$, than the motor can provide. That is, $\dot{\theta}_{\text{des}} > \dot{\theta}_{\text{max}}$. In order to assure that this doesn't happen, $\dot{\theta}$ could be equated to $\dot{\theta}_{\text{max}}$. This solution is equivalent to letting the slewing motor saturate naturally. However, if this solution is implemented, the desired Cartesian motion is no longer guaranteed. This situation occurs because $\dot{\gamma}$ is maintaining its speed as if $\dot{\theta} = \dot{\theta}_{\text{des}}$; but in actuality $\dot{\theta} = \dot{\theta}_{\text{max}}$.

To maintain desired Cartesian motion during actuator saturation, the right side of (3.17) can be multiplied by a scaling factor to ensure saturation does not occur when the spherical commands are sent to the motors of the crane:

$$\frac{\dot{\theta}_{\text{max}}}{\dot{\theta}_{\text{des}}} \tag{3.18}$$

The resulting transformation equation is then:

$$\begin{bmatrix} \dot{\gamma} \\ \dot{\theta} \end{bmatrix} = \begin{bmatrix} -\frac{\cos\theta}{r\cos\gamma} \\ -\frac{\sin\theta}{r\cos\gamma} \end{bmatrix} \dot{x} \left(\frac{\dot{\theta}_{\text{max}}}{\dot{\theta}_{\text{des}}} \right) \tag{3.19}$$

Simplifying this expression by recognizing that the $-\frac{\sin\theta}{r\cos\gamma}\dot{x}$ term is $\dot{\theta}_{\text{des}}$ yields the saturation law:

$$\begin{bmatrix} \dot{\gamma} \\ \dot{\theta} \end{bmatrix} = \begin{bmatrix} \dot{\gamma}_{\text{des}} \left(\frac{\dot{\theta}_{\text{max}}}{\dot{\theta}_{\text{des}}} \right) \\ \dot{\theta}_{\text{max}} \end{bmatrix} \tag{3.20}$$

The law states that $\dot{\theta}$ is equated to $\dot{\theta}_{\text{max}}$ and $\dot{\gamma}$ is scaled by a factor that relates how much $\dot{\theta}$ was reduced to maintain the actuator limit. This ensures that the crane will perform a pure x motion; all be it at a slower rate than when the θ actuator is not saturating.

Following the same analysis, the saturation law for $\dot{\gamma}$ can be written as:

$$\begin{bmatrix} \dot{\gamma} \\ \dot{\theta} \end{bmatrix} = \begin{bmatrix} \dot{\gamma}_{\text{max}} \\ \dot{\theta}_{\text{des}} \left(\frac{\dot{\gamma}_{\text{max}}}{\dot{\gamma}_{\text{des}}} \right) \end{bmatrix} \tag{3.21}$$

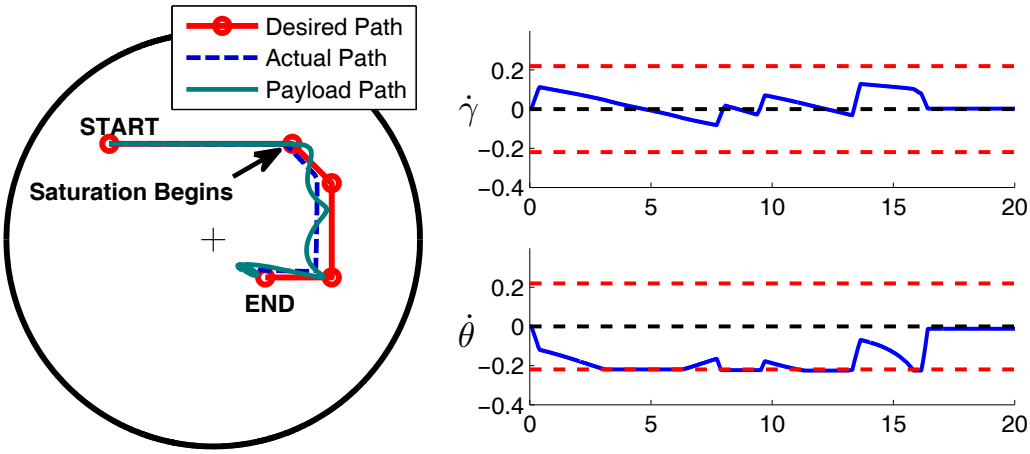

(a) Overhead View of Boom Crane Workspace

(b) Spherical Space Velocity Profiles

Figure 3.2: Example Cartesian Motion and Velocity Profiles

To show how saturation affects cartesian motion of a boom crane, a sample cartesian motion is simulated for a boom crane in Figure 3.2(a). The red/circled line is the desired payload trajectory if no saturation is present and the payload dynamics are ignored. The dashed line is the actual trajectory when the crane is subject to saturation limits. At first, the crane follows the desired trajectory perfectly. This remains true until the crane saturates in the θ direction. This can easily be seen in Figure 3.2(b), where the velocity profiles for $\dot{\gamma}$ and $\dot{\theta}$ are plotted. The $\dot{\theta}$ velocity profile saturates at four different points (approximately 3sec, 8sec, 11sec, and 16sec). This saturation is the reason why the desired path is different from the actual path of the crane.

This could be seen as a major disadvantage of a cartesian motion controller. However, cranes are operated by humans who continuously send velocity commands to the crane. In this operating mode, the operator is not sending a fixed velocity profile to the crane and expecting it to follow it perfectly. While the crane operator would notice a slowdown in speed of the crane, to compensate, the operator would send the command for a longer period of time. If positioning control was desired, a controller designed for that purpose could be implemented.

The actual path of the payload during Cartesian motion, shown as the solid line in

Figure 3.2(a), varies from the desired path because of pendulum dynamics. In the simulation response shown in the figure, no attempt to control the amount of oscillation was made. The following section will shown that payload oscillation can be easily controlled when the Cartesian motion transformation is implemented.

Since the magnitude of $\{\mathbf{x}_c\}$ can be arbitrarily selected by the control system designer, the question remains: What maximum Cartesian motions should be allowed? Essentially, the selection process involves a trade-off between constant-velocity Cartesian motions and maximum-velocity actuator motions. For time-optimal operation, it is obvious that the crane should always operate so that one of the crane's actuators is always saturating. However, for human operators, the Cartesian motion speed would continuously vary as the crane is being moved; which might hinder the operator from performing accurate control of the crane. Another challenging condition could occur when an operator first uses the crane. If they are unfamiliar with the Cartesian speed variation the crane has throughout its workspace, then the operator might expect the crane to move at a constant speed, but in fact its linear speed can vary considerably.

3.4 Feedback Linearization

The benefit of transforming the operation of a boom crane into Cartesian motions goes beyond operation efficiency. The transformation is also a feedback linearization controller for the payload dynamics. It transforms the spherical motions that lead to nonlinear equations of motion for the payload, into linear Cartesian equations of motion. The equations of motion of the payload are then much more linear. In effect, the payload will react to the boom motions as if the boom crane were a bridge or gantry crane.

The coordinate transformations T and V that define the feedback linearization require only two states of the crane to be measured: γ and θ. These states are not impractical to measure. The θ state could easily be measured by an encoder on the slewing motor. The γ coordinate could be measured by an encoder on the luffing cable motor, although one would have to implement the actuation transform, V, for this to work. The luff angle could also be measured by an inclinometer placed on the boom or an encoder attached to the rotation

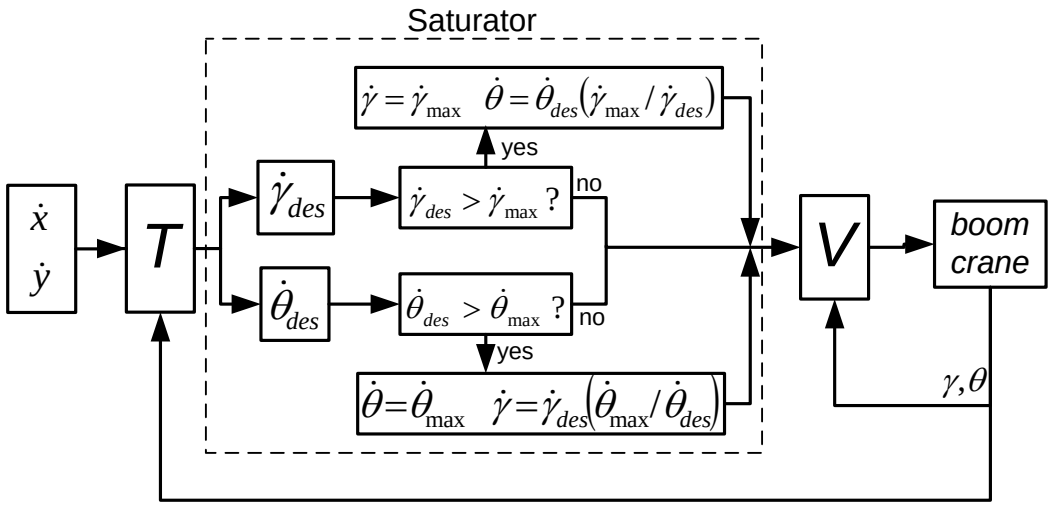

Figure 3.3: Transformation Block Diagram

point of the boom.

A block diagram of the Cartesian-transformation-feedback-linearization control system is shown in Figure 3.3. The desired $\dot{x}$ and $\dot{y}$ commands are sent to the transformation matrix, T, that generates the desired $\dot{\theta}$ and $\dot{\gamma}$. If $\dot{\theta}_{\text{des}}$ or $\dot{\gamma}_{\text{des}}$ are greater than $\dot{\theta}_{\max}$ and $\dot{\gamma}_{\max}$ respectively, then the saturation laws defined in (3.20) and (3.21) define the velocity of the crane. These velocities are sent to the kinematic transformation matrix, V. Feedback linearization lines show that the transformation matrices require the current configuration of the crane, γ and θ.

The benefit of feedback linearization is the ability to apply standard linear system control techniques to the crane. Input Shaping is one such control technique that is affective at limiting unwanted vibration in cranes. It was shown in Chapter 2.4.1 that while input shaping reduced vibration in boom crane motions without any compensation for its nonlinear dynamics, further improvement is still with compensation; feedback linearization is one such compensation.

Figure 3.4(a) shows an example of a Cartesian motion without input shaping on the full nonlinear boom crane model and the coordinate transformation in Figure 3.3. The payload oscillates significantly in response to the unshaped Cartesian commands. With shaping enabled, in Figure 3.4(b), the payload oscillation is greatly reduced. Any of the input shapers described in the previous Chapters could be implemented to reduce payload

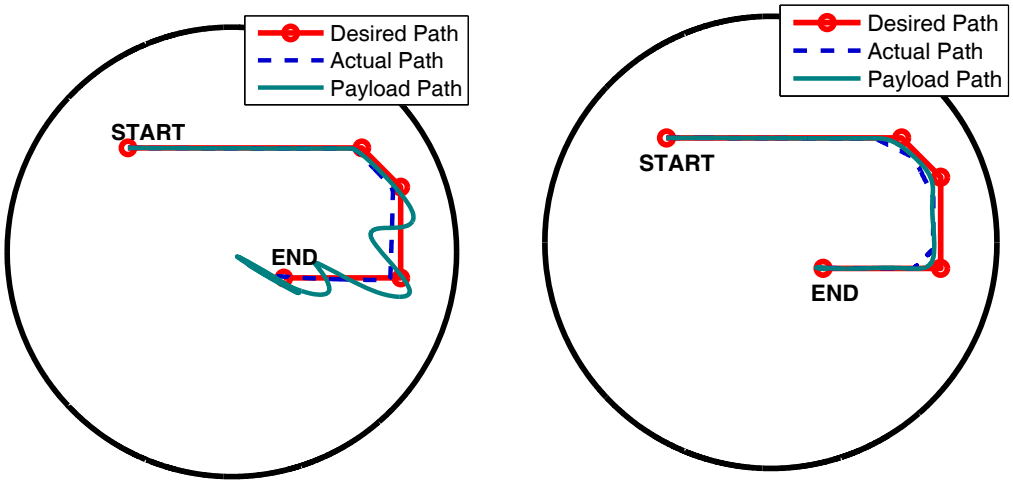

(a) Without Input Shaping Enabled. (b) With Input Shaping Enabled.

Figure 3.4: Effect of Input Shaping on Cartesian Boom Motion.

oscillation.

Another control strategy that could benefit from the feedback linearization of the payload dynamics is feedback control on the payload itself. This control system would require the measurement of the payload position in addition to the crane position states. Assuming that accurate measurement of the payload can be accomplished, simple feedback control systems, such as PD, could be used to reduce the swing of the payload [39, 19, 59]. For cranes, feedback control is best used to reduce payload oscillation caused by disturbances. These controllers could be designed without regard to the nonlinear dynamics of the payload, or the difficulties in accurately moving the crane. Figure 3.5 shows a block diagram of such a control system. A mobile boom crane would especially benefit from feedback control, as disturbances from driving the crane over rough terrain could cause significant payload oscillation.

Another benefit of this cartesian motion transformation for a mobile boom crane is the cancelation of payload oscillation caused by base motions. Essentially, if the motion of the base is known, then Cartesian motions of the boom can be used to cancel the vibration caused by the base motions. This technique, known as mult-input input-shaping, is currently under development [69].

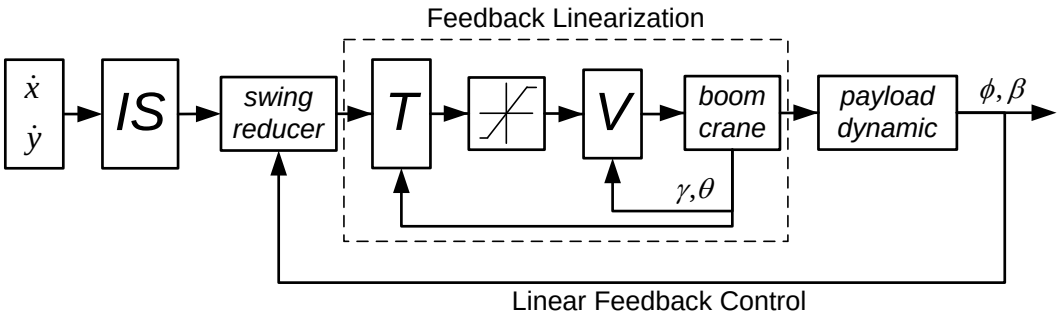

Figure 3.5: Feedback Control Block Diagram

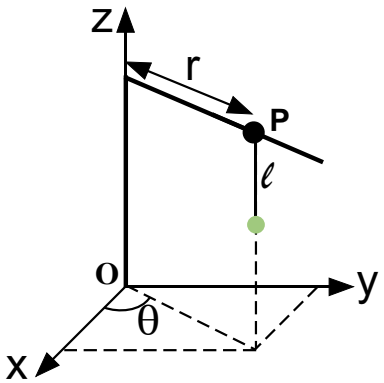

Figure 3.6: Cylindrical Coordinates of Tower Crane

3.5 Further Applications

There is nothing particular about this analysis that limits the cartesian transformation to boom cranes. One could easily implement this idea on any crane or robot system whose joint space is not cartesian space. A tower crane is one application that is naturally suited for this analysis. To implement this actuation system on a tower crane, one would only need to determine the transformation matrices T and V for the crane. Tower cranes naturally operate in cylindrical coordinates as shown in Figure 3.6. The kinematic transformation T_{tower} being:

$$\begin{bmatrix} \dot{r} \\ \dot{\theta} \\ \dot{\ell} \end{bmatrix} = \underbrace{\begin{bmatrix} \cos\theta & \sin\theta & 0 \\ -\frac{sin\theta}{r} & \frac{cos\theta}{r} & 0 \\ 0 & 0 & -1 \end{bmatrix}}_{T_{\text{tower}}} \begin{bmatrix} \dot{x} \\ \dot{y} \\ \dot{z} \end{bmatrix} \tag{3.22}$$

Another application of this analysis is a simple articulated boom lift like the one shown

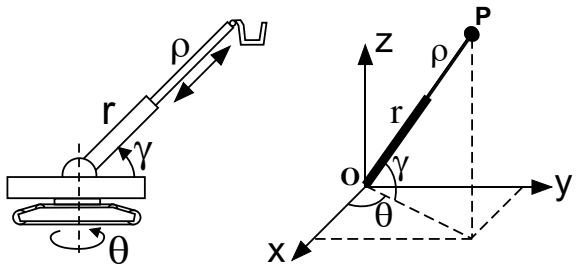

Figure 3.7: Articulated Boom lift and Coordinate System

in Figure 3.7 along with its coordinate description. This simple boom lift has a slewing motion and luffing motion like the boom crane, but it's third actuation is a prismatic joint that extends the length of the boom by an amount ρ. The inverse coordinate transformation of this device is:

$$\begin{bmatrix} \dot{\rho} \\ \dot{\theta} \\ \dot{\gamma} \end{bmatrix} = \underbrace{\begin{bmatrix} \frac{-\sin\theta\cos\theta}{(\sin\gamma\sin\theta+\cos^2\gamma)(r+\rho)} & \frac{-\sin^2\theta}{(\sin\gamma\sin\theta+\cos^2\gamma)(r+\rho)} & \frac{\cos\gamma}{(\sin\gamma\sin\theta+\cos^2\gamma)(r+\rho)} \\ \frac{-\sin\theta}{(r+\rho)\cos\gamma} & \frac{\cos\theta}{(r+\rho)\cos\gamma} & 0 \\ \frac{\cos\theta\cos\gamma}{\cos^2\gamma+\sin\gamma\sin\theta} & \frac{\sin\theta\cos\gamma}{\cos^2\gamma+\sin\gamma\sin\theta} & \frac{\sin\gamma}{\cos^2\gamma+\sin\gamma\sin\theta} \end{bmatrix}}_{T_{\text{ArtBoom}}} \begin{bmatrix} \dot{x} \\ \dot{y} \\ \dot{z} \end{bmatrix} \tag{3.23}$$

The only limitation of a machine that could take advantage of the approach described here is that the number of degrees of freedom of the machine must be three. The reason for this is that it was assumed that three independent actuators (and hence three degrees of freedom) exists on the machine that could uniquely provide a velocity command in three spacial dimensions. If the machine had four degrees of freedom, then it would be possible to generate more than one velocity command in actuator space that generates a single desired velocity in Cartesian space. Mathematically, the transformation matrix, T, would no longer be square and the matrix inversion of T, critical to the approach, could not be obtained.

To summarize, this chapter presents a Cartesian motion transformation for boom cranes and other rotary machinery. The transformation is meant to assist boom-crane operators as they manipulate payloads in difficult environments. Compensation for the actuation method of a crawler-style boom crane was also given. Because the inverse Jacobian method was used for the transformation, singularities exist which can lead to saturation of the

crane's actuators. A method to prevent this saturation while maintaining Cartesian motion is presented. It was also shown that the Cartesian transformation was also a feedback linearization control system, and as such, linear control techniques such as input shaping could be implemented on the boom crane without any adverse effects from nonlinear payload dynamics.

CHAPTER IV

DESIGN OF A MOBILE BOOM CRANE

This chapter describes a small scale mobile boom crane that was designed and is being constructed to support this research. There are two primary objectives for the mobile boom crane:

1. To be a platform for research into control of mobile boom cranes

2. To be a tool for engineering education

The previous two chapters serve as an introduction into the research possibilities of the mobile boom crane. In those chapters, the complicated dynamic control problem of the payload was introduced, along with a short study on how standard input-shaping techniques are effective despite of those complications.

However, an important goal of the mobile boom crane project is to develop new, more effective control techniques. One such idea, the feedback linearization mentioned in the previous chapter, will benefit from the mobile boom crane as a test bed. Another important application is control of the boom crane (slewing and luffing motions) and its mobile base simultaneously. The mobile boom crane is designed to developments in test these research areas as well.

Given their usefulness and interesting dynamic properties, mobile boom cranes are also useful for controls education. The fundamental dynamics of a crane, the pendulum, is easy for students to understand and observe. This allows students who work with cranes to easily see results. Bridge and tower cranes have been successfully implemented in advanced controls classes at Georgia Tech and Tokyo Tech [22, 27]. A mobile boom crane improves educational opportunities because it has the capability of providing students with a platform to study mobile robotics, oscillation control, actuator nonlinearities, control interfaces, tele-operation, nonlinear motion modeling, vibration analysis, feedback control, stability, inverse

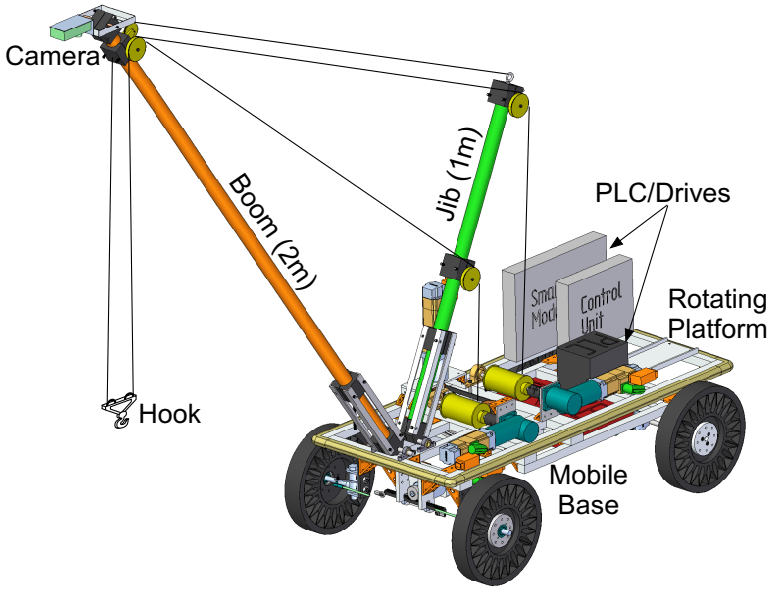

Figure 4.1: Mobile Boom Crane

kinematics, and trajectory tracking, among others.

4.1 Design Features

This section will describe the detailed design of the mobile boom crane. Section 4.1.1 will discuss the mechanical design of the crane and Section 4.1.2 will discuss the electronics/control system design of the crane.

4.1.1 Mechanical Design

Shown in Figure 4.1 is a conceptual drawing of the mobile boom crane. The main body of the boom crane rests on a mobile base. The base of the crane drives similar to that of a car with front wheel steering and rear wheel drive. This design enables the crane to emulate the drive system of an all-terrain-vehicle, which has been proposed as a practical base for implementing a mobile boom crane for de-mining purposes.

Attached to the top of the mobile base is the rotating platform that contains the mounts for the boom and gantry members, as well as most of the electronics, including motors, drives, and PLC. Mounting the electronics on the rotating base has a two fold purpose. First, they act as a counterweight needed to bring the center of mass of the crane to a stable position over the moving base. Second, with all control electronics on board, the

only tether to ground is a power cable. This allows for the crane to be used in many environments, not just in a laboratory setting.

The style of boom crane chosen for this project is the the crawler crane discussed previously in the thesis, and diagrammed in Figure 1.3 on page 3. An alternative design would have been a hydraulic boom crane, like the cranes pictured in Figure 1.2 on page 2. The crawler crane style was chosen for two reasons. One, because it uses electric motors, it is cheaper and lighter to implement than a hydraulic crane. The mobile crane is meant to be as light and portable as possible, a hydraulic style would not have met these design requirements, nor would a hydraulic system be necessary to lift the small payloads the mobile boom crane will lift. A second reason is that a crawler crane being actuated by electric motors is easier and more accurate to control than a hydraulic system.

One of the most difficult challenges for designing the boom crane was including hardware and sensors for a feedback control system. Machine vision is well suited for sensing the location of the hook in bridge and tower cranes [60]. However, in boom cranes the angle from the boom to the payload changes as the boom luffs. As a result, a camera rigidly attached to the end of the boom looking normal to the boom axis will only be effective at low luff angles. Ideally, the camera would always point vertically downward to sense the suspended payload.

To accomplish this in the mobile boom crane, a four-bar mechanism was implemented, as shown in Figure 4.2. The four links in the mechanism, shown as thick dotted lines in the figure, are the boom, the camera mount, the camera mount cable, and the base of the crane. These links keep the camera mount in a fixed orientation so that the camera is always directed downward at the payload. The machine vision camera will be used not only as a feedback control system, but as a data recording device as well.

4.1.2 Electrical/Control Design

A block diagram of the control system for the mobile boom crane is shown in Figure 4.3. A programmable logic controller (PLC), is central element in the control system. Its duties include input/output, digital control implementation, calculation, fault detection, and data

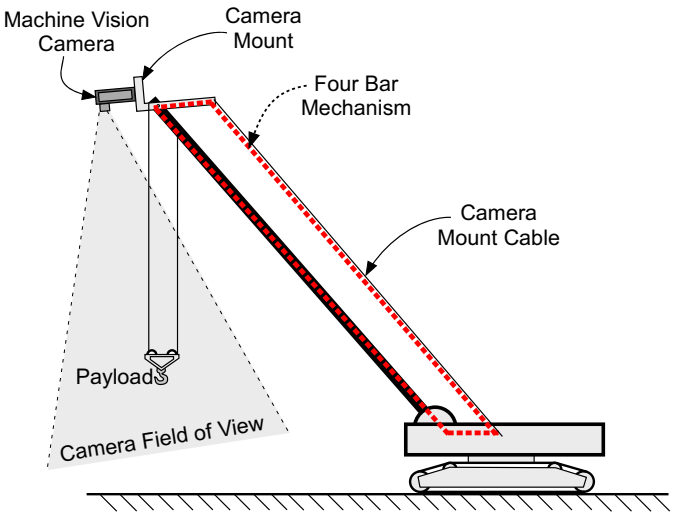

Figure 4.2: Four Bar Mechanism for Machine Vision Camera

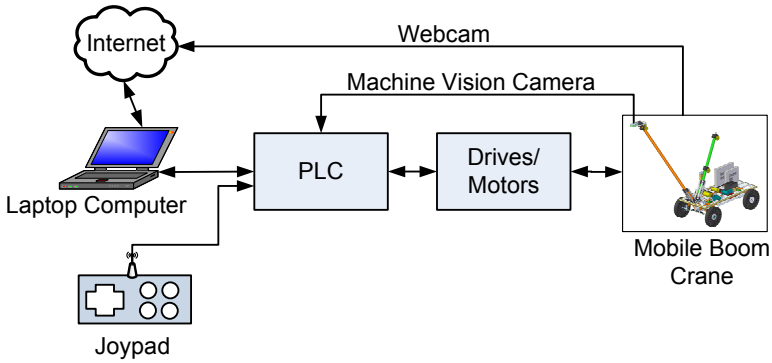

Figure 4.3: Control Diagram for Mobile Boom Crane

recording.

The crane can be controlled by two methods. The first is a joypad similar to that of many video game systems, pictured in Figure 4.4. The joypad has two control sticks that can control the base motion and boom motion. Other buttons on the joypad allow for the payload to be hoisted up and down and for selecting different control options. The joypad offers complete control of the boom crane in an easy-to-use format. This is in contrast to many boom cranes in which a different lever is used to control a given actuator. The intuitive nature of the joypad will also allow operators to easily control the crane without a long training period.

The crane can also be controlled via the computer interface shown in Figure 4.5. The crane can be manually controlled through the interface, but it also allows for trajectory

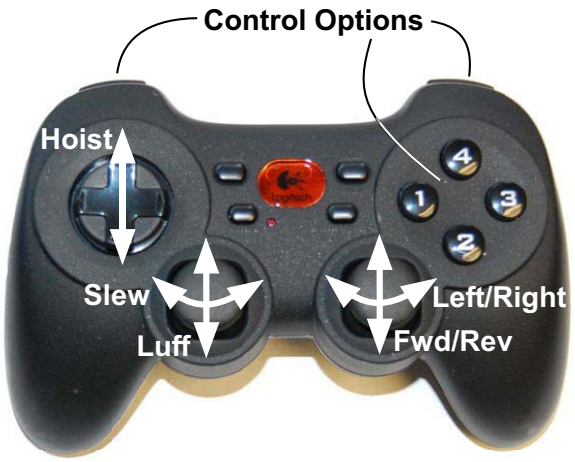

Figure 4.4: Joypad Used for Manual Control of Mobile Boom Crane

playback. The computer interface also allows for tele-operation of the crane over the internet. Tele-operation has been studied as a way to operate cranes in hazardous environments and allow educational test beds to be used by numerous students on a continual basis [54, 23, 27].

A boom crane presents an especially challenging problem for tele-operation because the crane is continuously rotating during operation. Because of this, a single view of the crane (2-dimensional or 3-dimensional) will not be able to inform an operator about the current state of the crane at all times. In the interface shown in Figure 4.5, an overhead view and side of the crane is shown. Three-dimensional views of the crane in its workspace will also

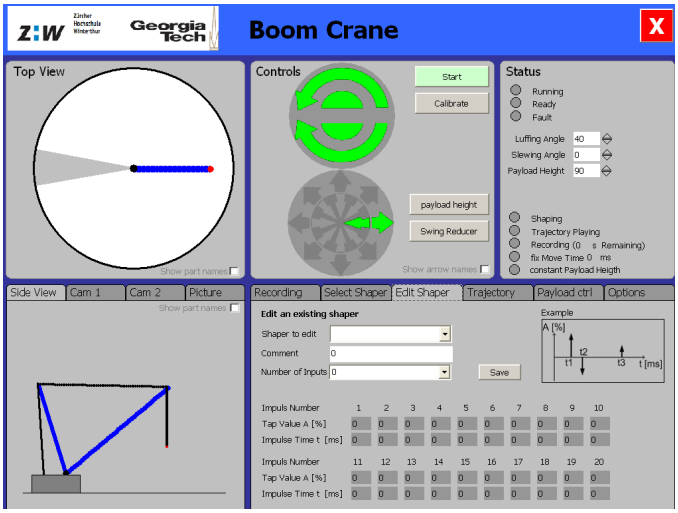

Figure 4.5: Graphical User Interface

be investigated.

To further aid in tele-operation, two webcams, shown in Figure 4.6, are used for real-time observation of the mobile boom crane. One camera provides an overhead view of the crane and its workspace. This camera gives the remote operator information about the crane environment and any obstacles the crane must avoid. The second is a "cockpit" camera that is mounted to the rotating base. This camera provides a view similar to that of an onboard operator of a standard crawler crane.

The motors and drives of the mobile boom crane are high performance Siemens Vector-drive motors. Because of this, and the light weight design of the boom, the motors will be able to accurately actuate the crane in all of its operating conditions. Remember that in Chapter 2 it was found that large amounts of torque were required to luff the crane at small luffing angles. However, smaller motors can be easily emulated on the high-performance motors by artificially setting low torque-limits in the motor drives. This emulation is possible for other control scenarios such as slow acceleration limits or large dead-zones.

4.2 Additional Benefits

The overall design of the crane is modular in nature. One consequence of this is that components can be added or replaced on the crane with relative ease. Of course, this allows

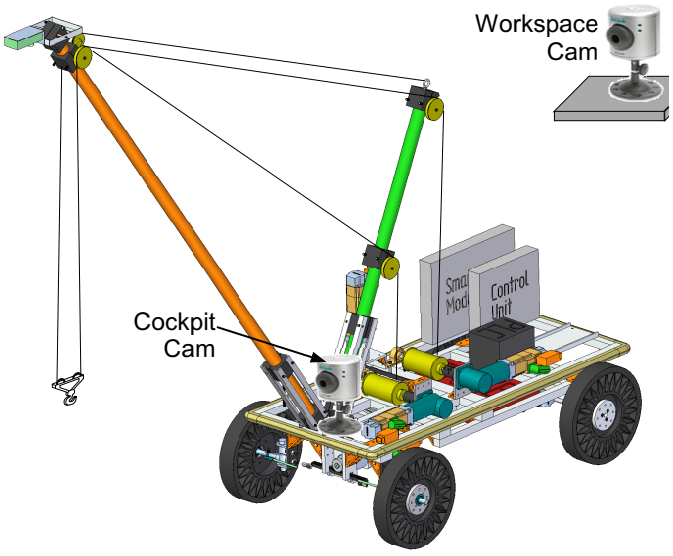

Figure 4.6: Webcams Used in Tele-Operation of Mobile Boom Crane

Figure 4.7: Extendible Boom Developed by Senior Design Students

for components to be updated regularly, but also allows the crane to be used as a platform for students in design classes to develop additional or better components for the crane. For example, in the Fall of 2007, students in a senior design class at Georgia Tech designed and built an extendable boom, shown in Figure 4.7, to attach to the crane and extend its functionality. Projects of this nature add additional value to the crane for research applications and also provide students with valuable design experience.

To support educational and research activities on the mobile boom crane, a 3D simulation was developed in Matlab^{TM} to facilitate testing of control strategies on the crane. A screen-shot of the simulation is shown in Figure 4.8. The simulation is an environment for students and researchers to easily and quickly implement their control designs before testing on the actual crane. The simulation runs in two modes. The first, pictured in Figure 4.8(a) is a standard cockpit view. The second is a ground-based operator view, pictured in Figure 4.8(b). This mode was made to test some of the aspects of Cartesian coordinate transformation in Chapter 3. The simulation also allows for portability, as the simulation can be run by anyone with a computer and Matlab^{TM}.

As mentioned previously, the only tether the mobile boom crane has to the ground is a power cable. This could limit the operation of the crane outside of lab. To increase crane mobility, a trailer is being constructed to attach an electric generator to the crane. The

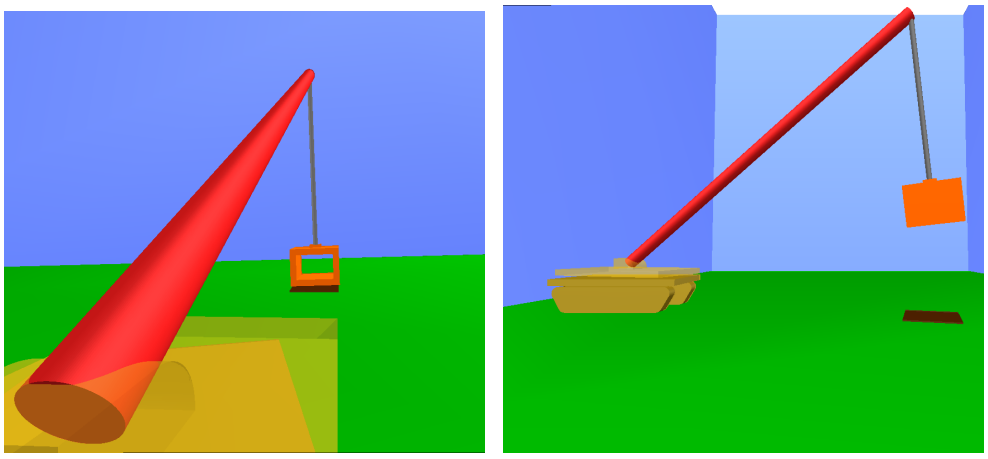

(a) Cockpit Operator View (b) Ground-based Operator View

Figure 4.8: Mobile Boom Crane Simulation

trailer, sketched in Figure 4.9, is designed to either be directly attached to the crane for in-tow operation, or to remain stationary and allow the crane to operate in a workspace around it. The electric generator addition was funded by an undergraduate research grant, so it will be partially designed and built by undergraduate students. This is another example of how the crane can be used in education applications.

This chapter discussed a small-scale mobile boom crane that is being built for research and education applications. The crane is designed to be able to test a wide range of research topics related to boom crane control. The crane includes feedback of the payload

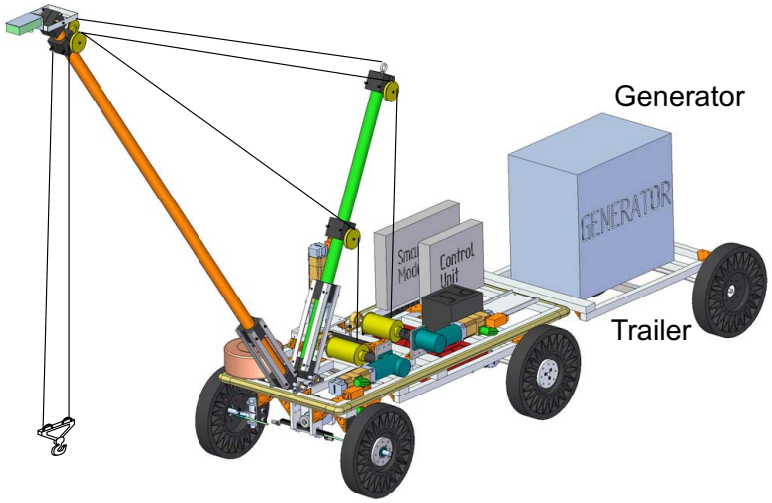

Figure 4.9: Electric Generator Trailer Used for Out-of-Laboratory Operation

swing via a machine vision camera, a joypad for manual control, a computer interface for tele-operation, and two web-cams to aide in tele-operation. The crane was also designed to be modular, allowing students to add or improve components of the crane for design classes or undergraduate research projects.

Acknowledgements

The mobile boom crane is sponsored by Siemens Energy and Automation, who will provide the motors, drives, PLC, vision camera, and money for building expenses for the crane.

CHAPTER V

INPUT-SHAPING FOR NON-LINEAR AND MULTI-MODE SYSTEMS

This chapter will describe three new methods for developing input shapers for specialized dynamic systems. The first input-shaping method compensates for an acceleration limit that is present in all physical systems. This nonlinearity is detrimental to the performance of some standard input shapers such as ZVD, EI, and SI. A technique for modifying these standard input shapers is presented.

The second method compensates for a system with unequal acceleration and braking dynamics. For this method, a first-order filter is used as a model for acceleration and braking delays. It assumed that the time constants are unequal, leading to a nonlinear command-shaping dynamic effect. A technique for modifying UMZV input shapers to work better for these types of systems is developed.

The third input-shaping method develops input shapers for systems with multiple natural frequencies. The new design centers around creating minimum-impulse input shapers for multi-mode systems.

5.1 Acceleration Limited Input Shaping

Cranes and many other manufacturing equipment often have drives that operate with a fixed or maximum acceleration limit. Fixed acceleration actuators also occur in other on-off systems such as the thruster jets used on spacecraft. Figure 5.1 shows how a fixed acceleration affects an input-shaped velocity command. A velocity step command is used

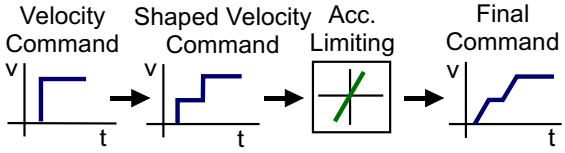

Figure 5.1: Effect of Acceleration Limiting

as a baseline command in this section because it is the standard input for many types of systems, such as cranes.

Because the acceleration limit is not taken into account when designing normal input shapers, a question arises: *Are the vibration-reducing properties of the input shaper degraded by the acceleration limit?* Section 5.1.1 determines which shapers are unaffected by the acceleration limit. Section 5.1.2 examines input shapers that are affected by an acceleration limit, while Section 5.1.3 demonstrates how to modify them to compensate for the detrimental effects. Experimental results from a 10-ton industrial bridge crane are used to support the main theoretical findings. Section 5.1.4 discusses extension of the techniques to other types of systems[1].

5.1.1 Unaffected Input Shapers

This subsection will develop a set conditions that an input shaper must meet in order for it to be unaffected by a constant acceleration rate limit.

Theorem 1 *The fixed acceleration system shown in Figure 5.2(a) will be equivalent to the reduced system shown in Figure 5.2(b) under the following conditions:*

$$\begin{aligned} &a) \quad |A_i| = c \quad \forall\, i = 1 \ldots n \\ &b) \quad t_{i+1} - t_i \geq \frac{v_f}{a}|A_i| \quad \forall\, i = 1 \ldots (n-1) \end{aligned}$$

where A_i and t_i are the impulse amplitudes and times of the input shaper, n is the number of impulses in the shaper, v_f is the final setpoint velocity, c is a constant, and a is the acceleration limit.

Proof: The shaped step command, indicated by v_s in Figure 5.2(a), can be written as:

$$v_s(s) = \sum_{i=1}^{n} \frac{A_i}{s} e^{-t_i s} \tag{5.1}$$

Based on assumption a):

$$v_s(s) = \sum_{i=1}^{n} sign\,(A_i)\, \frac{c}{s} e^{-t_i s} \tag{5.2}$$

[1]The concepts described in this section were developed in conjunction with Dr. Jason Lawrence.

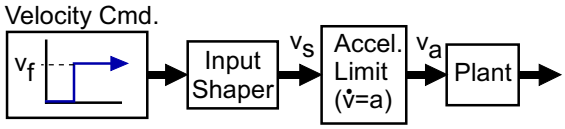

(a) Original Nonlinear System

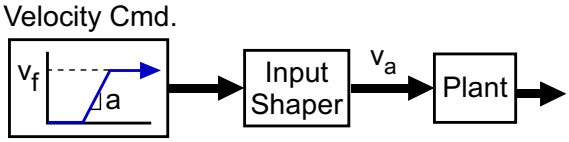

(b) Linear System Equivalent

Figure 5.2: Nonlinear System is Reduced to a Linear System

Figure 5.3(a) shows an example shaped step command, v_s. Based on (5.2) this command can be decomposed into a sum of delayed steps, as shown in Figure 5.3(b). Figure 5.3(a) also shows the acceleration limited command, v_a, as a dotted line. Similar to v_s, v_a can also be decomposed into a series of delayed, ramped-step commands, as shown by the dotted lines in Figure 5.3(b). Notice in Figure 5.3(b) that both the step commands and their corresponding ramped-step commands begin at the same time. Condition b) ensures that the rise time of each step in the acceleration limited command, v_a, will always be less than the time between the step changes in v_s. As a result, all of the ramped-step commands in the decomposition shown in Figure 5.3(b) reach the same final value as the step commands.

Based on the above observations and (5.2), v_a can be written as a sum of ramped steps:

$$v_a(s) = \sum_{i=1}^{n} sign\left(A_i\right) \frac{a}{s^2} \left(1 - e^{-\frac{v_f}{a}s}\right) e^{-t_i s} \tag{5.3}$$

where the term $\frac{a}{s^2}\left(1 - e^{-\frac{v_f}{a}s}\right)$ represents the Laplace transform of a ramped-step command with slope a and a steady-state value of v_f. Using assumption a), this equation can be rewritten as:

$$v_a(s) = \underbrace{\frac{1}{c}\frac{a}{s^2}\left(1 - e^{-\frac{v_f}{a}s}\right)}_{\text{Ramped Step}} \underbrace{\sum_{i=1}^{n} A_i e^{-t_i s}}_{\text{Input Shaper}} \tag{5.4}$$

According to (5.4) the v_a command can be represented as the product of a ramped-step and the original input shaper in the Laplace domain. This proves that the acceleration limited command, $v_a(t)$,is a properly shaped command that will move the system without

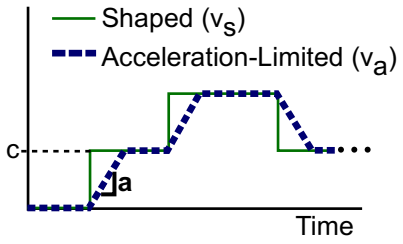

(a) Shaped and Acceleration-Limited Command

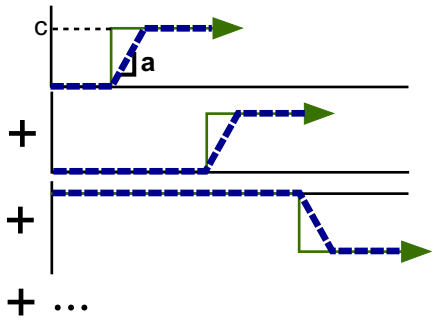

(b) Command Decomposition

Figure 5.3: Command Decomposition

vibration. As a result, input shaping will work exactly as designed. No special techniques are required to compensate for the effects from the acceleration limiting. However, instead of the system being driven by a step, it will respond as though it were commanded by a ramped step. *End Proof.*

The results of Theorem 1 are only applicable to input shapers that satisfy restrictions a) and b) in the theorem statement. Common shapers that satisfy restriction a) are ZV and unity magnitude (UM) shapers. In most crane applications restriction b) will be satisfied because the spacing of the impulses is based on the system period, which is typically much longer than the rise time of the system. If this condition is not satisfied, then the techniques developed in Section 5.1.3 can be used to find an alternative input-shaping solution.

Example: Zero Vibration Shapers

Previously it was shown that a ZV shaper will eliminate vibration for a linear system and is unaffected by an acceleration limit provided it satisfies constraint b) of Theorem 1. To demonstrate this property of the ZV shaper, simulations were performed and experimental data was collected on a 10-ton industrial bridge crane with acceleration-limited motors. The acceleration limit for the crane is $a = 0.12\text{m/s}^2$ with a maximum velocity of $v_f = 0.358\text{m/s}$.

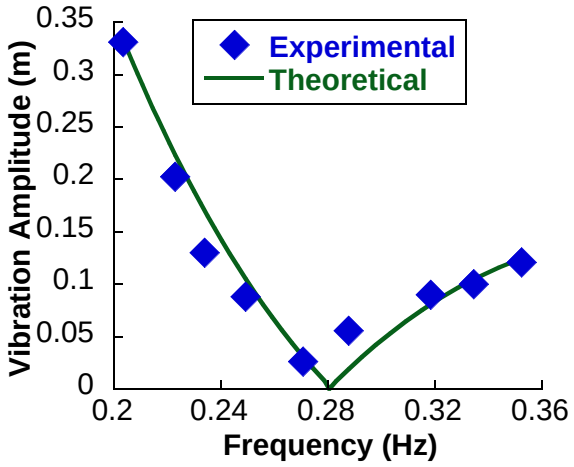

Figure 5.4: Sensitivity curve for ZV Shaper

The damping ratio of the crane is approximately $\zeta = 0.006$ as determined by the log decrement method. Figure 5.4 shows theoretical and experimental sensitivity curves of a ZV shaper implemented on the crane. In this experiment, the ZV shaper was designed to suppress a frequency of $\omega_m = 0.28$Hz. This shaper was used to form a shaped-step velocity command that was used to drive the crane. The oscillation of the crane's payload was measured for nine different payload suspension lengths, which correspond to the nine different experimental frequencies in Figure 5.4.

It can be seen by comparing this sensitivity curve with the ZV sensitivity curve shown in Figure 1.7 on page 7 in the introduction that the general shape is not modified and the vibration is still zero at the design frequency. These simulation and experimental results verify that the ZV shaper is not affected by the acceleration limit.

5.1.2 Predicting Shaper Degradation

For input shapers that do not meet the conditions of Theorem 1 constraints, such as ZVD, EI, or SI shapers, it is important to know how much vibration will be induced by the presence of an acceleration limit. To determine this effect on a crane, linear system theory can be used to predict the vibration of the crane's payload response. First, a single step is examined, then an input-shaped step is investigated. While this analysis is done for a crane, a similar analysis can easily be done for other linear flexible systems.

5.1.2.1 Step Response

A crane's payload response to a velocity input at the overhead suspension point is:

$$\frac{\theta(s)}{V(s)} = \frac{1}{L}\frac{-s}{s^2+\omega_n^2}, \tag{5.5}$$

Where θ is the swing angle of the payload, V is the velocity of the overhead trolley, L is the payload suspension length, and $\omega_n = \sqrt{g/L}$, is the natural frequency of oscillation. The response to an acceleration input is:

$$\frac{\theta(s)}{A(s)} = \frac{1}{L}\frac{-1}{s^2+\omega_n^2}, \tag{5.6}$$

Where A is the trolley acceleration. The responses to a step and ramped-step in velocity are given by:

$$\theta_{step} = \frac{-v_f}{L\omega_n}\sin(\omega_n t) \tag{5.7}$$

$$\theta_{ramped-step} = -2\frac{a}{L\omega_n^2}\sin\left(\frac{\omega_n v_f}{2a}\right)\sin\left(\omega_n t - \frac{\omega_n v_f}{2a}\right) \tag{5.8}$$

Where v_f is the magnitude of the step and a is the acceleration of the crane. From (5.8) it can be seen that as a approaches infinity, the acceleration-limited response approaches a velocity step response, as expected. These responses can be rewritten as a function of two dimensionless parameters, α and β, as:

$$\theta_{step} = -\beta\sin(\omega_n t) \tag{5.9}$$

$$\theta_{ramp} = -2\frac{\beta}{\alpha}\sin\left(\frac{\alpha}{2}\right)\sin\left(\omega_n t - \frac{\alpha}{2}\right) \tag{5.10}$$

where,

$$\alpha = \frac{\omega_n v_f}{a} \tag{5.11}$$

$$\beta = \frac{v_f}{L\omega_n}. \tag{5.12}$$

Input-Shaped Response

The response to a series of acceleration-limited step inputs will now be examined. The amplitude of residual vibration is a function of the two dimensionless variables, α and β, and the amplitudes and times of the steps. Consider an arbitrary input shaper with n impulses that have amplitudes A_i and time locations t_i. When this input shaper is convolved with a step command and passed through an acceleration limiter it will produce a command similar to that in Figure 5.3(a). Now assume that the velocity of each step reaches steady state before the subsequent impulse time. That is,

$$t_{i+1} - t_i > \frac{v_f A_i}{a} \tag{5.13}$$

If this is the case, then the equation for the velocity profile for the shaped command can be written as:

$$V_L(s) = \sum_{i=1}^{n} \underbrace{\left(\frac{a}{s^2} \left(1 - e^{-s\frac{v_f A_i}{a}} \right) \right)}_{\text{Ramped Step}} \underbrace{e^{-st_i}}_{\text{Time Delay}} \tag{5.14}$$

Superposition is used to form the total response from this input:

$$\Theta_s = -2\frac{\beta}{\alpha} \sum_{i=1}^{n} \left(\sin\left(A_i \frac{\alpha}{2} \right) \sin\left(\omega_n t - \left(\omega_n \tau_i + A_i \frac{\alpha}{2} \right) \right) \right). \tag{5.15}$$

Figure 5.5 plots the magnitude of this equation divided by β, or $|\Theta_s|/\beta$, versus α for ZVD, EI, and two SI input shapers. From this plot it is clear that as α increases, the greater the amplitude of residual vibration. This increase in vibration indicates an increased degradation of input-shaper performance. This result is consistent with the earlier result that as α approaches zero, the fixed-acceleration response approaches a step response and input shaping works as intended. There exists a limit on α, depicted in Figure 5.5 as a circle, for which α is no longer defined. This limit occurs when (5.13) is no longer valid. That is, the system is not able to accelerate fast enough to reach the desired velocity, $v_f A_i$ for each of the i steps in the command.

The process used to generate Figure 5.5 can be a useful tool when choosing a shaper for an acceleration-limited system. By plugging in the known system parameters it can be determined whether a given shaper will yield an acceptable level of residual vibration.

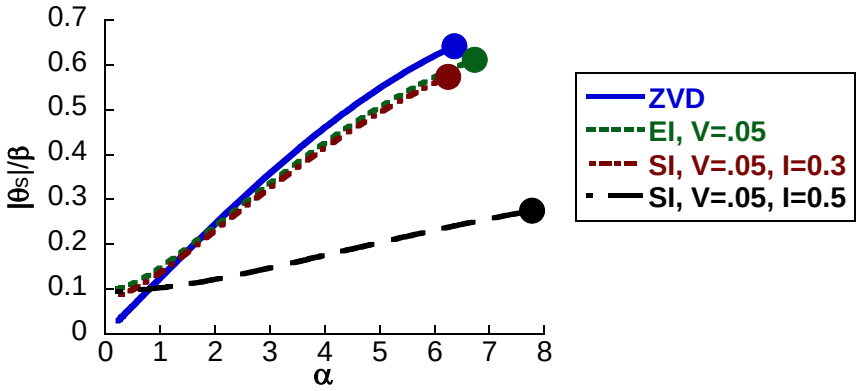

Figure 5.5: Amplitude of Residual Vibration as a Function of α for Various Shapers

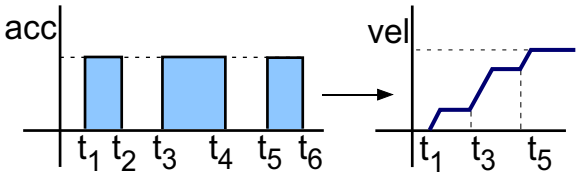

Figure 5.6: Acceleration for a Three-Step Velocity Command

5.1.3 Improving Affected Input Shapers

If the acceleration limit causes unacceptable shaper performance degradation, then a new modified shaper can be utilized. Consider the three-pulse acceleration command shown on the left in Figure 5.6. Integrating this profile over time will generate the acceleration-limited velocity command shown on the right in Figure 5.6. The acceleration profile in Figure 5.6 is analogous to the fuel-efficient pulse commands developed for flexible spacecraft in [50]. In that study, a set of constraints was developed to generate a time-optimal command in the form of Figure 5.6. Repeated here, the first constraint is the residual vibration from a set of n impulses:

$$V(\omega) = \sqrt{\left[\sum_{i=1}^{n} \sin \omega t_i\right]^2 + \left[\sum_{i=1}^{n} \cos \omega t_i\right]^2} \tag{5.16}$$

For ZV and ZVD shapers, this is set to zero residual vibration, $V(\omega) = 0$. For other shapers such as EI and SI, this is set to some small percentage of unshaped vibration. Because of the transcendental nature of (5.16), a constraint on the duration of the input shaper is imposed:

$$min\,(t_n) \tag{5.17}$$

Where t_n is the time of the last impulse. The constraint ensures that the shaper is as short as possible. Finally, the amplitudes are restricted to:

$$A_i = (-1)^{i+1} \tag{5.18}$$

This constraint is in place to ensure that the input shaper produces a command in the form of Figure 5.6.

These constraints can be used to form an input shaper that compensates for an acceleration-limited system. To do this, suppose that the acceleration profile shown in Figure 5.6 is that of a ZVD command that has passed through an acceleration limit. If the times t_i are chosen such that they satisfy the constraints developed in [50] and those of the input shaper, then a new ZVD shaper that compensates for a fixed acceleration can be formed.

One additional constraint that must be added to the problem formulation to generate a correct shaper is to set the area under the acceleration profile in Figure 5.6. In order to ensure that the command reaches the desired final velocity, the area must be equal to the final velocity of command. Mathematically, this is stated as:

$$v_f = a\left((t_2 - t_1) + (t_4 - t_3) + (t_6 - t_5)\right), \tag{5.19}$$

where t_i are the switch times in Figure 5.6. This final velocity could be viewed as a velocity limit of the system if the designer must take it into account. An optimization routine can now be set-up to solve for the impulse times and amplitudes that satisfy the constraint equations in (5.16) through (5.19).

After the optimization is completed and the switch times t_i are determined, the acceleration-limited ZVD shaper can be defined by:

$$\begin{bmatrix} \dfrac{A_i}{a_{max}} \\ \\ \tau_i \end{bmatrix} = \begin{bmatrix} t_2 - t_1 & t_4 - t_3 & t_6 - t_5 \\ \\ t_1 & t_3 & t_5 \end{bmatrix} \tag{5.20}$$

If a more robust input shaper is used, then the required number of acceleration pulses will increase. For example, a two-hump EI shaper or an SI shaper designed for more than $\pm 20\%$ changes in frequency will typically have four impulses, and therefore require four pulses in acceleration.

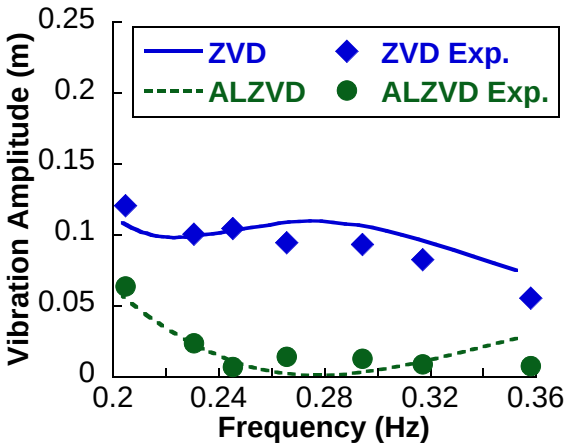

Figure 5.7: Sensitivity Curves for ZVD and ALZVD Input Shaper

To test the effectiveness of the compensated shapers, sensitivity curves were theoretically created and experimentally verified on the industrial bridge crane mentioned earlier in Subsection 5.1.1. Note that for all tests, the crane's acceleration limit is imposed on the input-shaped commands. Figure 5.7 shows the sensitivity curve for a standard and acceleration-limited (AL) ZVD input shaper. The vertical axis is residual vibration of the crane's payload in meters and the horizontal axis is the oscillation frequency. The ZVD and ALZVD input shapers were designed for a payload suspension length of 3.2m, corresponding to a frequency of $\omega_m = 0.28$Hz. Without modifying the input shaper, the payload suspension length was changed and the vibration level from a velocity step response was measured. The curves in Figure 5.7 show that the AL shaper outperforms the standard shaper over a wide range of frequencies. Similar plots for EI and SI input shapers are shown in Figures 5.8 and 5.9. The numerous experimental results shown in Figures 5.7-5.9 clearly demonstrate that the acceleration-limited shapers outperform their standard counterparts.

General Procedure

To summarize, an input shaper that compensates for a fixed acceleration can be generated by these steps:

1. Select the design constraints of the desired shaper (ZVD, EI, SI).

2. Formulate the constraints of a fuel-efficient shaper.

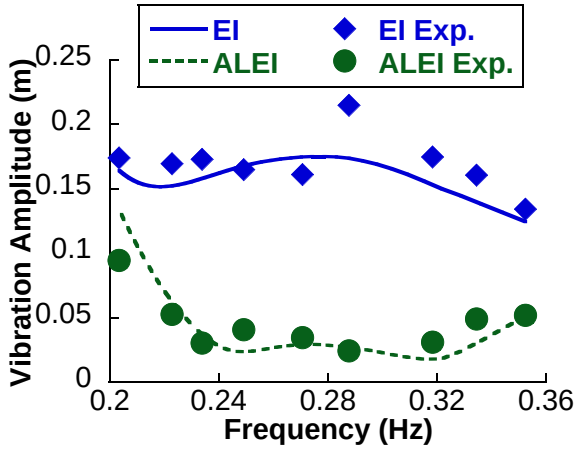

Figure 5.8: Sensitivity Curves for EI and ALEI Input Shaper

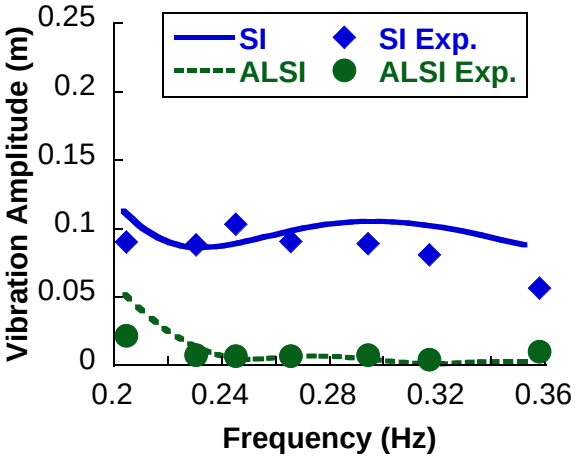

Figure 5.9: Sensitivity Curves for SI and ALSI Input Shaper

3. Perform a numerical optimization to determine the impulse times that produce the desired velocity, v_f.

4. Extract the input shaper using (5.20).

This process can be used for any input shaper, even those that do not satisfy condition b) of Theorem 1.

5.1.4 Concept Extensions

Multi-Step Commands

Thus far, all of the results have assumed that the desired command is a step. However, the above concepts can easily be extended to multi-step commands, such as the one shown in Figure 5.10. Note that a single velocity pulse, or a chain of velocity pulses can also be categorized as a multi-step command. The multi-step command transitions to a new velocity at the times τ_i. Now suppose the multi-step command is shaped, as shown by the dashed line. Assume, for the moment, that the shaped command reaches the commanded velocity, before the next commanded velocity transition τ_i:

$$\tau_{i+1} - \tau_i \geq t_n \tag{5.21}$$

where t_n is the time of the last impulse of the shaper. Under these conditions the shaped, multi-step command can be viewed as a sum of shaped step commands. The concepts presented earlier predict the response to each of these shaped step commands and the total response can be found with superposition. Recall that the model of the oscillation is linear, or approximated as linear, so the response to any series of inputs can be determined by superposition.

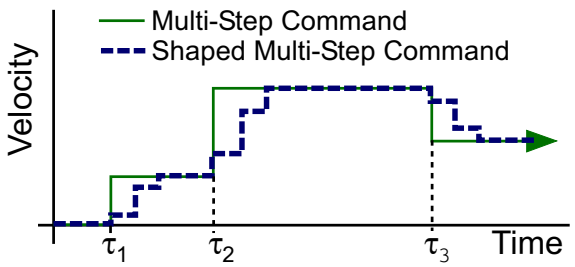

Figure 5.10: An Example of a Shaped and Unshaped Multi-Step Command

Consider what would happen in Figure 5.10 if time τ_2 were decreased while all the other parameters were held constant. At some point the velocity transition at τ_2 would "interrupt" the shaping sequence initiated at τ_1. This would degrade the effectiveness of the shaper and lead to increased vibration. This is an example of what happens when condition (5.21) is violated.

Other Linear Systems

The ideas in this chapter have been illustrated using a crane. However, nothing about these ideas is unique to cranes. In fact, the crane plant could be replaced with any stable, linear system that has one (or more) undamped modes. The results can also be extended to multi-mode shapers for multi-mode systems[46, 33, 15]. If the system has damped modes, then the results in Sections 5.1.1 and 5.1.3 still hold. However, the shapers for damped systems are more complicated than shapers for undamped systems in two ways:

1. The impulse times are given by: $\tau_i = f(\zeta) \cdot T$ where T is the damped period and f is a nonlinear function.

2. The impulse amplitudes are also a nonlinear function of the damping ratio.

As a result of these complications, the results in Section 5.1.2 do not strictly apply. Therefore, predicting the residual vibration of standard shapers due to the acceleration nonlinearity becomes more difficult. However, for systems with low damping ratios, the results are very similar to undamped systems. For example, an ALZVD shaper outperforms its

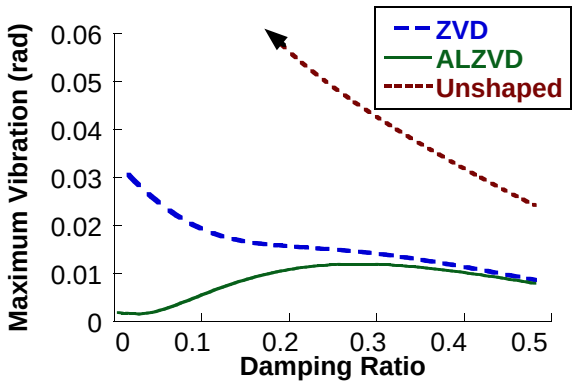

Figure 5.11: Shaper Sensitivity to Damping Ratio

standard counterpart over a wide range of damping ratios. This trend can be seen in Figure 5.11. The figure indicates that the ALZVD shaper always outperforms the ZVD, even for high damping ratios. Similar results can be found for other shapers.

5.2 Nonlinear Braking Input Shaping

This section describes an input shaping design technique for a system with an unsymmetrical acceleration/braking element in its control architecture. An example of this element's affect on a velocity command is illustrated in Figure 5.12. The actual velocity of the system will ramp up to speed by a first-order exponential rise, with a time constant τ_a. However, the system brakes using a different time constant τ_b. Such a nonlinearity would occur in systems using a clutch or some other mechanical element for braking. It can also occur because the electrical circuitry responds differently to acceleration and braking.

Although the input shaping technique described in this section is valid for any system that exhibits this braking nonlinearity, a bridge crane will be used to demonstrate the properties of the acceleration/braking nonlinearity. The most common command for cranes is a velocity pulse, like the command shown in Figure 5.12. This pulse occurs when a human-operator pushes a button, or it could arise from an automated constant velocity command. Because of its practicality, a pulse will be used as the baseline command for analysis of the nonlinearity.

Input shapers are generally designed for linear systems. So the question arises: *how do input shapers perform in the presence of the non-symmetrical acceleration-braking shown in*

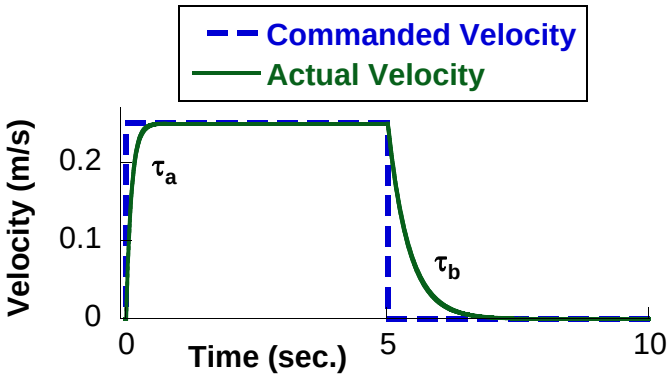

Figure 5.12: Non-Symmetrical Acceleration-Braking

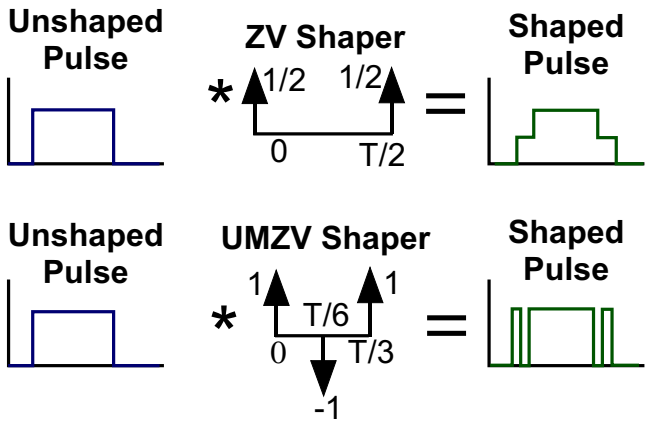

Figure 5.13: ZV and UMZV Shaped Pulse

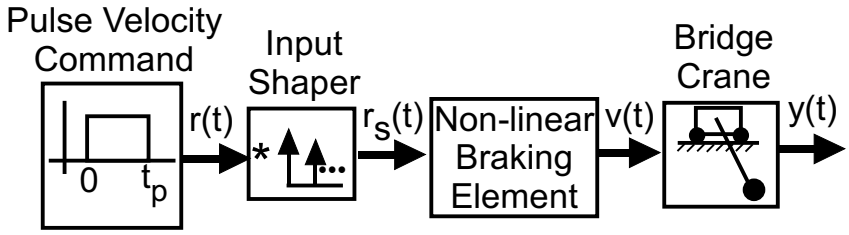

Figure 5.14: Crane Block Diagram

Figure 5.12? The analysis in this section will focus on two common types of input shapers: ZV and UMZV. Figure 5.13 shows how a pulse input in velocity is modified by these two input shapers. Subsections 5.2.1 and 5.2.2 demonstrate that the non-linearity effects some input shapers move than others. Subsection 5.2.3 develops a new type of command that is based on input shaping, but compensates for the non-symmetrical acceleration-braking. Subsection 5.2.4 examines the performance of this new command[2].

A typical implementation of an input shaper on a system with a braking nonlinearity is illustrated in Figure 5.14. The unshaped command, r(t), is a pulse with time duration t_p. This signal passes through an input shaper to form the shaped command, $r_s(t)$. The drive system cannot follow the shaped command exactly due to the non-linear braking effect. This block has an acceleration time constant τ_a and a braking time constant τ_b, as shown in Figure 5.12.

The control architecture shown in Figure 5.14 was implemented on a portable crane,

[2]The concepts described in this section were developed in conjunction with Dr. Jason Lawrence.

Table 5.1: Bridge Crane Experimental Parameters.

Setpoint Velocity, v_{max}	Hoisted Length, L	Acceleration Constant τ_a
0.17 (m/s)	0.84 (m)	0.117 (s)

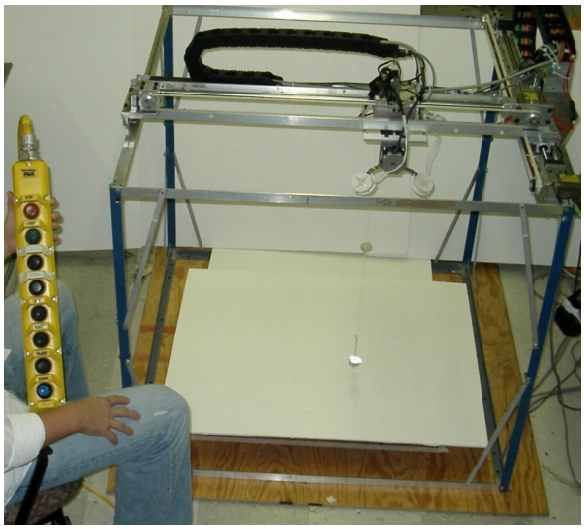

Figure 5.15: Portable Crane Experimental Setup

shown in Figure 5.15. The crane has a 1 m x 1 m x 1 m workspace [24]. It is actuated by Siemens motors, drives, and PLC and is capable of tracking a desired command and recording the response. This configuration makes it possible to investigate a wide range of dynamic effects. In this case the non-symmetrical acceleration-braking was programmed into the PLC. The suspended payload deflection is recorded with a digital camera. The configuration parameters used for all of the experiments in this section are shown in Table 5.1.

5.2.1 ZV Shaping with a Braking Non-linearity

It is known that a ZV shaper will eliminate the residual vibration for in a perfectly-modeled linear system. This section will shown that the ZV shaper works well in spite of the non-linear braking effect.

5.2.1.1 ZV Commands: Effect of Pulse Duration

As the pulse duration varies, the structure of the ZV shaped command changes. This, in turn, effects how successful the ZV shaper is at eliminating vibration. To clarify this

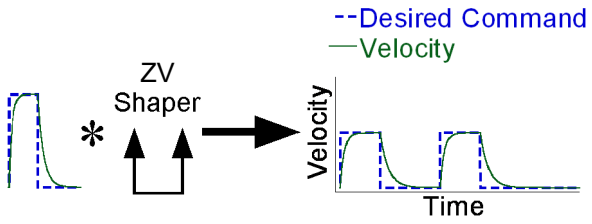

Figure 5.16: Deconvolution of a *ZV short command*

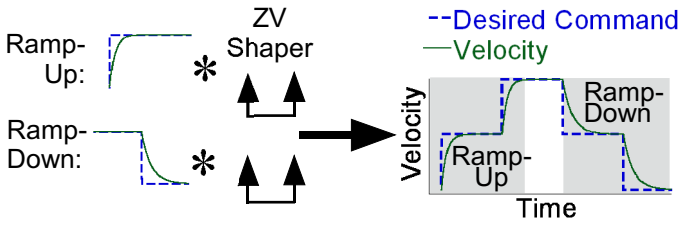

Figure 5.17: Deconvolution of a *ZV long command*

issue, a shaped command will be categorized as either a *short command*, *long command*, or *interference command* depending on the value of the pulse duration relative to the shaper duration. Figures 5.16, 5.17, and 5.18 show each command respectively.

ZV Short Commands. Figure 5.16 shows an example of a ZV shaped *short command*, as well as the resulting velocity. It consists of two pulses. The key feature is that the velocity returns to zero before the second pulse in the shaped command. This condition yields the following constraint on the pulse duration (t_p) given the command parameters:

$$t_p > t_2 - 3\tau_b \tag{5.22}$$

where $t_2 = \frac{T}{2}$ is the time of the second impulse of a ZV shaper. Note that $3\tau_b$ is used as the approximate time for the exponential decay to reach zero (steady state). For some systems with a long τ_b, *short commands* may not exist.

Similar to Figure 5.13, Figure 5.16 shows how a ZV *short command* is the convolution of a ZV shaper with a pulse. The velocity response can also be formed as the convolution of a ZV shaper with a smoothed pulse despite the nonlinear braking. This smoothed pulse is formed by applying the non-symmetrical acceleration-braking to the original pulse command. Note that this decomposition is only possible when assumption (5.22) holds. Because a ZV shaper can be deconvolved from the resulting velocity, it will yield zero

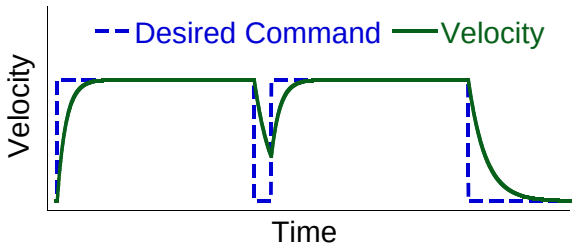

Figure 5.18: *ZV Interference Command*

residual vibration.

ZV Long Commands. Figure 5.17 shows an example of a ZV shaped long command and the resulting velocity. It consists of a two-step ramp-up segment, a coasting segment, and a two-step ramp-down segment. The key feature of this type of command is that the velocity reaches its full speed before the ramp-down segment. This condition yields the following constraint on pulse duration (t_p):

$$t_p < t_2 + 3\tau_a \tag{5.23}$$

Figure 5.17 also shows how long commands can be decomposed. Suppose the command were divided into two parts, labeled ramp-up and ramp-down in the figure. The ramp-up command can be expressed as the convolution of a step and a ZV shaper. Similarly, the velocity profile can be expressed as the convolution of a smoothed step with a ZV shaper. The smoothed step is formed by applying the non-symmetrical acceleration-braking to the original step. Again, this decomposition is only possible when assumption (5.23) holds. As a result, the ramp-up segment will cause zero residual vibration. Similar arguments can be made about the ramp-down segment. Because the total command can be formed as the sum of these two segments, a ZV shaped *long command* will cause zero residual vibration.

ZV Interference Commands. For these types of commands the pulse duration causes a change in command that interferes with the exponential acceleration or braking process. Figure 5.18 shows an example of such a command. This scenario occurs when the pulse duration is between a short and long command. Because of its structure, a ZV shaper cannot be deconvolved out of an *interference command*. Therefore, ZV shaped *interference commands* will yield some residual vibration.

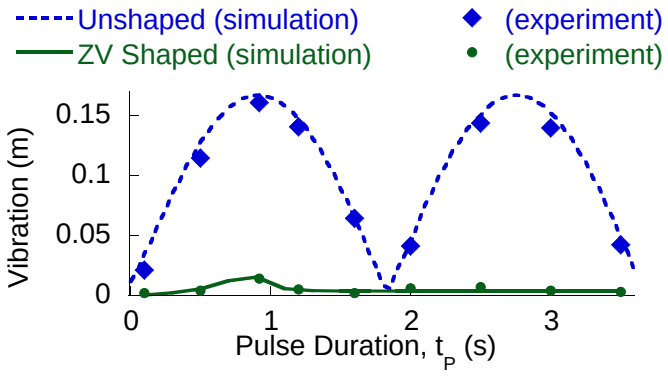

Figure 5.19: Vibration Induced by ZV Shaped and Unshaped Pulse for Various Pulse Durations [$\tau_b = 0.065\ (s)$]

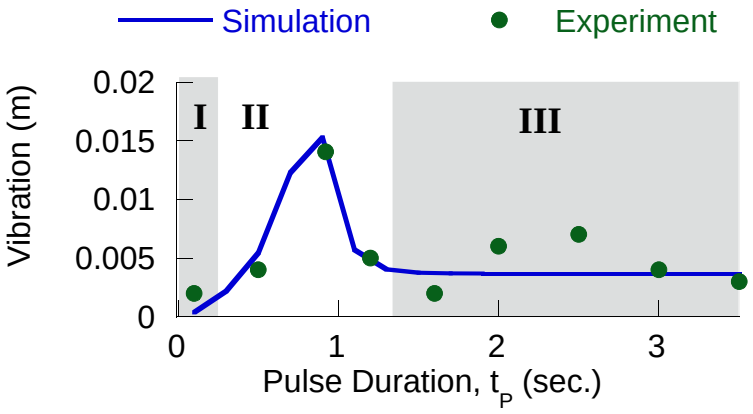

Figure 5.20: Vibration Induced by ZV Shaped Pulse for Various Pulse Durations [same parameters as Figure 5.19]

To test the conclusions made above, both simulations and experiments were conducted. Figure 5.19 compares the residual vibration of ZV shaped commands to unshaped commands. The horizontal axis is pulse duration and the vertical axis is the vibration induced by the corresponding command. Notice that all of the ZV shaped commands out-perform unshaped commands. Figure 5.20 gives a close-up view of the ZV shaped results. The figure divides the commands into *short* (I), *interference* (II), and *long* (III) using (5.22) and (5.23). Both *short* and *long commands* have very low residual vibration, while *interference commands* cause substantially more residual vibration.

Two important points should be made about the results. First of all, the range of *long commands* extends infinitely outward along the horizontal axis in Figure 5.20. So, for a large range of pulse durations, a ZV shaped command performs very well. The second

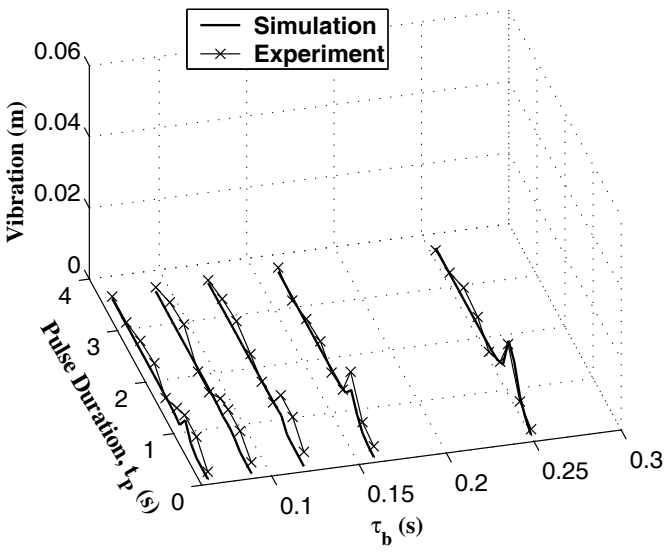

Figure 5.21: Vibration of ZV Commands for Various t_p and τ_b

point is that even though *interference commands* can cause residual vibration, it is still small compared to the residual vibration induced by unshaped commands.

5.2.1.2 Effect of Time Constants

As the acceleration and braking time constants vary, the severity of the braking non-linearity changes. In particular, as $\tau_a \rightarrow \tau_b$ the system behaves more like a linear system and a ZV shaper becomes more effective. Figure 5.21 shows the effect of changing both the pulse duration and the braking time constant. The vertical axis shows the vibration for each case. The figure plots both experimental and simulated results. Each line is analogous to the data presented in Figure 5.20. Notice that since τ_a is set at 0.117 (see Table 5.1), as $\tau_b \rightarrow \tau_a = 0.117$ the overall vibration is at a minimum because the braking nonlinearity vanishes.

5.2.2 UMZV Shaping with a Braking Nonlinearity

A UMZV shaper has some advantages over a ZV shaper. The shaper yields faster commands and can be implemented in on/off type drive systems. Therefore, a natural question to ask is: *how is a UMZV shaper affected by the braking non-linearity under discussion?* The previous subsection demonstrated that despite the non-symmetrical acceleration-braking,

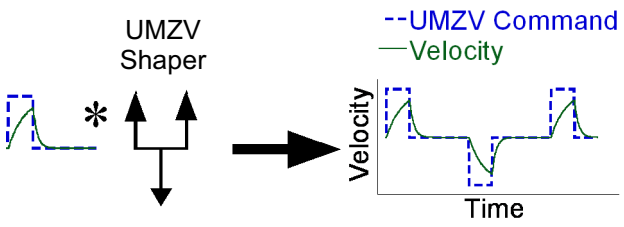

Figure 5.22: Deconvolution of a UMZV Shaped *Short Command*

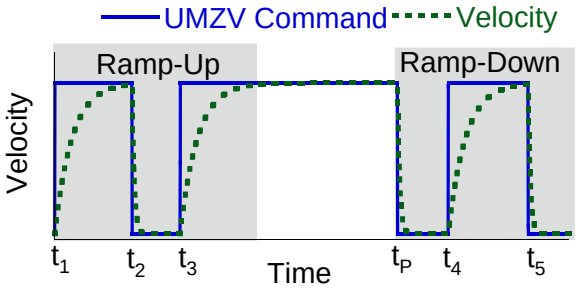

Figure 5.23: UMZV Command Template

ZV shaping still performed well under most conditions. However, this subsection will show that a UMZV shaper will have degraded performance due to the nonlinearity over a wide range of parameters.

5.2.2.1 UMZV Commands: Effect of Pulse Duration

When discussing the effects of pulse duration on UMZV shaping, it is again useful to categorize the commands as *short*, *long*, or *interference*.

UMZV Short Commands. Figure 5.22 shows an example of a short command and the resulting velocity. Equation (5.22) can be used as the constraint on t_p for short commands. However, in this case $t_2 = \frac{T}{6}$ is the time of the second impulse of a UMZV shaper. Figure 5.22 also shows how a UMZV *short command* can be expressed as the convolution of a UMZV shaper with a pulse. Similar to Section 5.2.1, the velocity can also be written as the convolution of a UMZV shaper with a smoothed pulse. Because this deconvolution is always possible, a UMZV short command will not induce residual vibration.

UMZV Long Commands. Figure 5.23 shows an example of a UMZV *long command* along with the resulting velocity. Using the same definition given in Section 5.2.1, a constraint

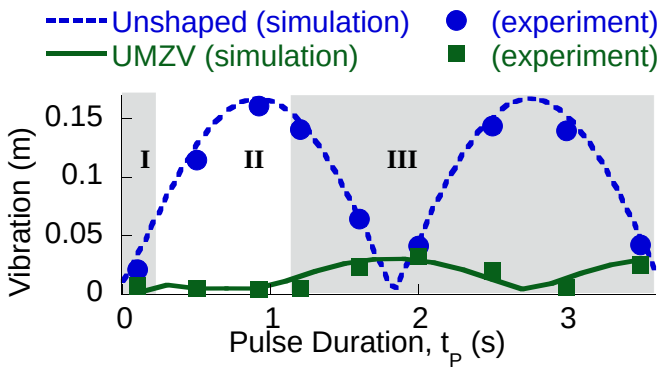

Figure 5.24: Vibration of Unshaped and UMZV Shaped Pulse for Various Pulse Durations $[\tau_b = 0.065(s)]$

on the pulse duration can be formed:

$$t_p > t_3 + 3\tau_a \tag{5.24}$$

where $t_3 = \frac{T}{3}$ is the time of the third impulse of a UMZV shaper. However, unlike ZV *long commands*, a UMZV shaper cannot be deconvolved out of a UMZV *long command*. So, in general, a UMZV *long command* will cause some residual vibration.

UMZV Interference Commands. An interference command falls in between a short and long command. The same arguments presented in Section 5.2.1 also hold here. Therefore, an interference command will induce residual vibration.

To test the above conclusions, simulations and experiments were performed. Figure 5.24 shows vibration as pulse duration is varied for unshaped and UMZV shaped commands. The figure divides the graph into *short* (I), *interference* (II), and *long* (III) commands. The figure shows that the system has measurable residual vibration for both interference and long commands. However, for the particular values of $\tau_a$and τ_b used, the vibration from *interference commands* is fairly small. Comparing Figures 5.24 and 5.19, the range of commands that cause residual vibration for UMZV commands is much larger than for ZV commands. However, the UMZV shaped commands still have much less vibration, on average, than the unshaped commands.

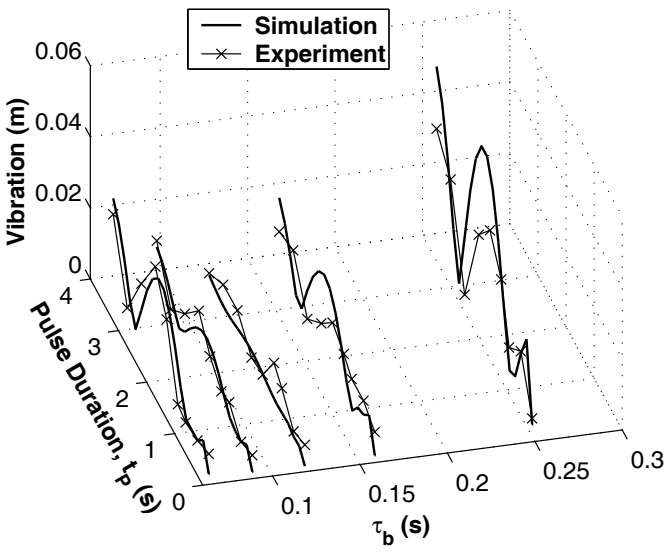

Figure 5.25: Vibration of UMZV Commands for Various t_p and τ_b

5.2.2.2 UMZV Commands: Effect of Time Constants.

The same conclusions presented in Section 5.2.1.2 regarding the acceleration and braking constants, can be drawn here. Namely, as $\tau_a \rightarrow \tau_b$ the system behaves more like a linear system. As a result, the effectiveness of the UMZV shaper improves under these conditions. Figure 5.25 shows the effect of changing both the pulse duration and the braking time constant. The vertical axis shows the vibration for each case. Notice that as $\tau_a \rightarrow \tau_b = 0.117$ the overall vibration approaches zero. However, notice that over most of the parameter space, UMZV-shaped commands induce residual vibration, unlike the ZV commands shown in Figure 5.21.

5.2.3 Formulation and Implementation of a UMZV$_C$ Shaped Command

As mentioned earlier, a UMZV shaper has the advantages of being fast and compatible with on/off actuators. However the last section showed that the effectiveness of UMZV shapers are degraded by the braking non-linearity. This section will show how to formulate a new, modified UMZV shaper that retains the advantages of the standard shaper, while compensating for the braking non-linearity. The new version of this shaper will be referred to as UMZV$_C$ (the "c" stands for compensated).

5.2.3.1 Formulation of the $UMZV_C$ Shaper

Figure 5.23 gives a graphical representation of the problem at hand. The goal is to find times $t_1, \ldots, t_5$ such that the command will yield zero residual vibration. Note that the command shown in Figure 5.23 would be classified as a long command according to the definition in Section 5.2.2.1. The first step is to find the residual vibration of the ramp-up portion as a function of times t_1, t_2, and t_3 and set it equal to zero. Then, a similar procedure can be applied to the ramp down portion.

The ramp-up portion of the trolley velocity in Figure 5.23 can be represented as the sum of three terms:

$$\begin{aligned} v(t) =& v_{max} \cdot \left(\left(1 - e^{-t/\tau_a} \right) * \delta\left(t - t_1\right) \right) \\ & - v_{max} \cdot \left(\left(1 - e^{-t/\tau_b} \right) * \delta\left(t - t_2\right) \right) \\ & + v_{max} \cdot \left(\left(1 - e^{-t/\tau_a} \right) * \delta\left(t - t_3\right) \right) \end{aligned} \tag{5.25}$$

for all $t \geq 0$, where v_{max} is the maximum velocity. Each term consists of a 1^{st}-order response to a step command convolved with a time-delayed impulse.

The steady state response to (5.25) can easily be derived from linear system theory. For example, if it is used to drive a undamped system, then:

$$\theta(t) = \sum_i \theta_i(t) \qquad \forall t \geq 0 \tag{5.26}$$

where $\theta_i(t)$ is the angular deflection of the payload due to the i^{th} term in (5.25) and is given by:

$$\theta_i(t) = \frac{1}{\omega L} |G_i| sin\left(\omega t - \omega t_i - \frac{\pi}{2} + \angle G_i \right),$$

$$|G_1| = \frac{v_{max}}{\sqrt{\left(\tau_a \omega\right)^2 + 1}}, \qquad \angle G_1 = tan^{-1}\left(\frac{1}{\tau_a \omega} \right) - \pi,$$

$$|G_2| = \frac{v_{max}}{\sqrt{\left(\tau_b \omega\right)^2 + 1}}, \qquad \angle G_2 = tan^{-1}\left(\frac{1}{\tau_b \omega} \right),$$

$$|G_3| = |G_1|, \qquad \angle G_3 = \angle G_1$$

A more compact representation can be formed using phasor notation. Recall that the goal is to find an expression for the residual vibration of the ramp-up segment as a function of the step times t_1, t_2, t_3. Using phasor notation, the residual vibration amplitude, $A(t_1, t_2, t_3)$, can be simply stated as:

$$A\left(t_1, t_2, t_3\right) = \left| \sum_i \vec{v}_i \right| \tag{5.27}$$

where,

$$|\vec{v}_i| = \frac{|G_i|}{\omega L} \qquad\qquad \angle\vec{v}_i = -\omega t_i - \frac{\pi}{2} + \angle G_i$$

Because the goal is to make (5.27) equal zero, the phasors can be scaled, rotated, or reflected across the real-axis without affecting the results. Using these properties, a simplified set of phasors can be formed:

$$\begin{aligned} &|\vec{v}_1| = 1, \quad \angle v_1 = 0, \quad |\vec{v}_2| = \sqrt{\frac{\left(\tau_a\omega\right)^2 + 1}{\left(\tau_b\omega\right)^2 + 1}}, \\ &\angle\vec{v}_2 = \omega t_2 + \tan^{-1}\left(\frac{1}{\omega\tau_a}\right) - \tan^{-1}\left(\frac{1}{\omega\tau_b}\right) \\ &|\vec{v}_3| = 1, \quad \angle v_3 = \omega t_3 \end{aligned} \tag{5.28}$$

Note that here we have used the assumption that time t_1 will be zero.

There are two methods for finding times t_2 and t_3 that yield zero residual vibration. One method is to substitute (5.28) into (5.27), set the result equal to zero, and solve algebraically. While this method will yield a solution, the calculations become tedious. A much more efficient, and insightful, method is to use a geometric approach. Each of the three phasors in (5.28) can be represented as vectors, as shown in Figure 5.26. For the vectors to sum to zero they must form a triangle. Note that vector $\vec{v}_3$ is translated from quadrant II (solid) to quadrant I (dashed).

Figure 5.26 also shows how the angles of the triangle relate to the phasor angles given in (5.28). Note that $\alpha_2 = \angle\vec{v_2}$ and $\alpha_3 = \angle\vec{v_3}$. With the vectors arranged in a triangle, the law of cosines can be used to solve for the angles α_2 and α_3. Then (5.28) can be used to

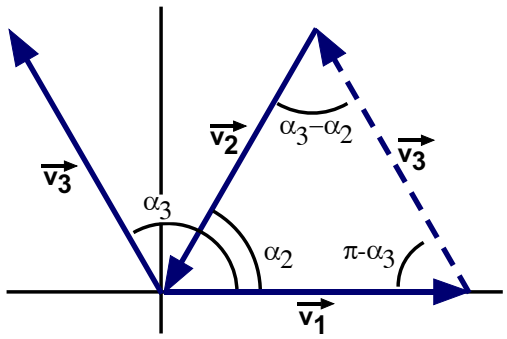

Figure 5.26: Phasor Diagram

solve for times t_2 and t_3:

$$\begin{aligned} t_2 =& 1/\omega \left(\tan^{-1}\left(\frac{1}{\omega\tau_b}\right) - \tan^{-1}\left(\frac{1}{\omega\tau_a}\right)\right) \\ &+ 1/\omega \cos^{-1}(\beta) + nT \\ t_3 =& 1/\omega \cos^{-1}\left(2\beta^2 - 1\right) + mT,\ \beta = \frac{1}{2}\sqrt{\frac{(\tau_a\omega)^2+1}{(\tau_b\omega)^2+1}} \end{aligned} \tag{5.29}$$

where n, m are positive integers and $n \leq m$ to ensure that $t_2 < t_3$.

A few comments should be made about the solution given in (5.29):

- The length of the command, t_3, will always be less than $\frac{T}{2}$ provided $n = m = 0$. This means that the UMZV$_\mathrm{C}$ command will always be shorter than a ZV command if $n = m = 0$.

- Additional solutions can be found by adding integer multiples of the system period, T, to t_2 or t_3. This appears as the mT and nT terms in (5.29).

- The β argument of the $\cos^{-1}$ terms in (5.29) must be between $[-1,\ 1]$ for the result to be a real number, thereby constraining the values of $\omega\tau_a$ and $\omega\tau_b$. The physical interpretation can be illustrated using Figure 5.23. The vibration from the steps at times t_1 and t_3 (accelerating) must be canceled by the vibration from the step at time t_2 (braking). However, if $\tau_b \ll \tau_a$, then the vibration from the t_1 and t_3 steps is very small compared to the vibration from the step at t_2. In this case, the vibration cannot be canceled, no matter how t_2 and t_3 are chosen. Under these conditions, the β term is outside the range $[-1,\ 1]$ and no real solution can be found.

5.2.3.2 Implementation of $UMZV_C$ Commands

A UMZV_C command cannot be formed by straightforward convolution of a pulse with an input shaper. More specifically, note that $t_4 \neq t_p + t_2$ and $t_5 \neq t_p + t_3$ in Figure 5.23. The reason is that during the ramp-up portion the velocity will: accelerate-brake-accelerate. However, during the ramp-down process this sequence is: brake-accelerate-brake. Because the sequences are different, the command switch-times must be different. To correctly solve for the ramp-down times, switch the values of τ_a and τ_b in (5.29) and solve for new times $\bar{t_2}$ and $\bar{t_3}$. Then solve for t_4 and t_5 using:

$$t_4 = t_p + \bar{t_2} \qquad t_5 = t_p + \bar{t_3} \tag{5.30}$$

5.2.4 Evaluation of UMZV_C Commands

The UMZV_C command retains all the advantages of a standard UMZV command: it is faster than ZV shaped commands, and uses only on/off commands. This section will examine the benefits and limitations of the UMZV_C command. It will be shown that UMZV_C commands are more effective than standard UMZV commands at reducing vibration over a wide range of parameters.

5.2.4.1 $UMZV_C$ Commands: Effect of Time Constants

Changing the acceleration and braking time constants affects the functionality of the UMZV_C shaped commands, though not nearly so much as standard UMZV commands. As was the case earlier, when $\tau_a = \tau_b$ the system is linear. The UMZV_C command becomes equivalent to a UMZV command and there is zero residual vibration. However, there are other effects that must be considered.

The derivation of the UMZV_C command made several assumptions about the values of $\tau_a$and τ_b. Notice that in Figure 5.23 the system reaches the commanded velocity before the next switch time. These constraints can be mathematically stated as:

$$\begin{aligned} c_1: &\qquad t_2 > 3\tau_a &\qquad t_4 - t_p > 3\tau_b \\ c_2: &\qquad t_3 - t_2 > 3\tau_b &\qquad t_5 - t_4 > 3\tau_a \end{aligned} \tag{5.31}$$

where the constraints are labeled c_1 and c_2 respectively.

Another restriction on the acceleration and braking constants comes from the $\cos^{-1}$ terms in (5.29). As discussed earlier, the arguments of these terms must lie between $[-1, 1]$. This feasibility constraint can be mathematically stated as:

$$\omega\tau_b > 0.5\sqrt{(\omega\tau_a)^2 - 3} \qquad\qquad \omega\tau_a > 0.5\sqrt{(\omega\tau_b)^2 - 3} \tag{5.32}$$

for both ramp-up and ramp-down segments in Figure 5.23.

5.2.4.2 UMZV$_C$ Commands: Design Algorithm

To create a UMZV$_\mathrm{C}$ command one must apply equations (5.29) and (5.30) and then possibly adjust the m and n parameters to satisfy the constraints in (5.31). One also needs to check that the feasibility constraint (5.32) is satisfied. To aid in this process the constraints can be represented graphically, as shown in Figure 5.27. The steps for using this figure to design a UMZV$_\mathrm{C}$ shaper are:

1. Use the system parameters τ_a, τ_b, and T to identify a point in Figure 5.31.

2. If the point is in the dark red region labeled "No Sol'n", then the parameters violate the constraint (5.32) and no solution is possible.

3. If the point is a feasible solution, then the Figure indicates the minimum values of n and m. Regions of constant n and m are separated by solid lines and are shaded white and grey in an alternating pattern.

4. Substitute the values of n and m, as well as the other system parameters into (5.29) and (5.30) to complete the command design.

5.2.4.3 UMZV$_C$ Commands: Effect of Pulse Duration

Changing the pulse duration also effects the functionality of a UMZV$_\mathrm{C}$ shaper. In earlier discussions, commands were categorized as either *short*, *interference*, or *long* depending on the value of t_p. The same analysis can be applied here. The UMZV$_\mathrm{C}$ command is designed to work for long commands because its derivation was based on the long command illustrated in Figure 5.23. As a result, assumption (5.24) must hold.

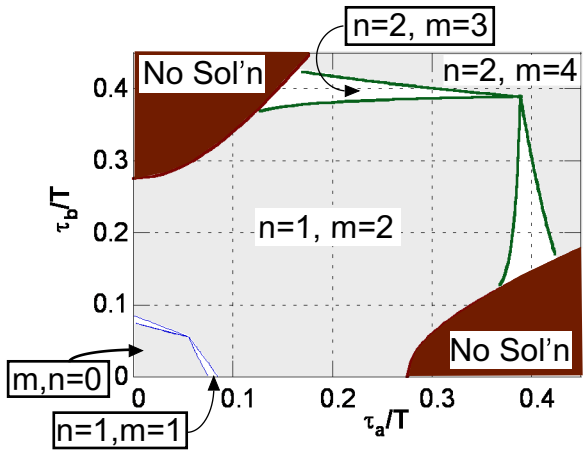

Figure 5.27: Constraints on τ_a/T and τ_b/T for a UMZV$_C$ Shaped Command

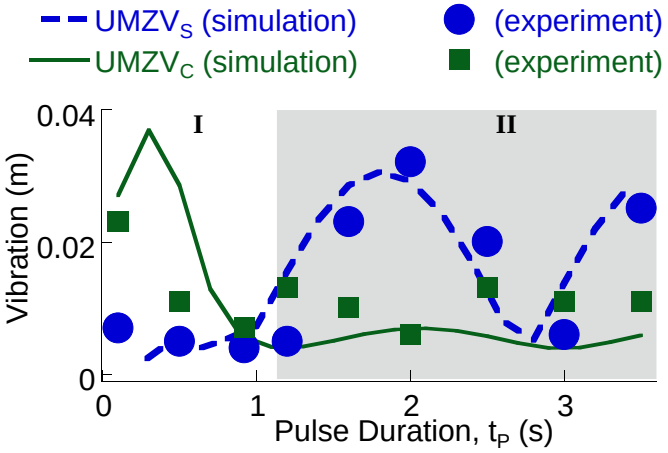

Figure 5.28: UMZV$_C$ Shaped and Unshaped Vibration for Various Pulse Durations [$\tau_b = 0.065(s)$]

To test the limits of the pulse duration, simulations and experiments were conducted. The vibration induced by UMZV$_C$ commands was measured for various pulse durations. The results are shown in Figure 5.28, along with the UMZV vibration data from Figure 5.24 for comparison. The graph is divided into two regions. Region II contains long commands that satisfy (5.24), and region I contains all other commands. The vibration resulting from UMZV$_C$ commands in region II is nearly zero, which supports the theoretical arguments above. The figure shows that the new UMZV$_C$ shaper is a substantial improvement over the standard UMZV shaper.

A second set of simulations and experiments were conducted in which both the pulse

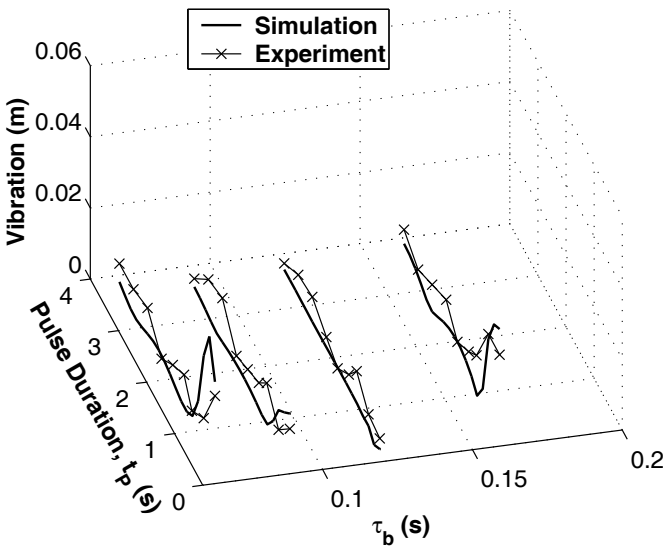

Figure 5.29: Vibration of UMZV$_{\mathrm{C}}$ Commands for Various t_p and τ_b

duration and braking time constant were varied. The results are shown in Figure 5.29. Notice that for most of these values, the vibration is nearly zero. Again this is a substantial improvement over the standard UMZV data shown in Figure 5.25.

In summary, this section examined the effects of non-symmetrical acceleration-braking on the performance of input-shaped commands. It was shown that ZV commands retain good functionality, whereas UMZV shapers are adversely affected by the nonlinearity. Therefore, a new type of UMZV$_{\mathrm{C}}$ shaped command was developed that compensates for the nonlinearity, while retaining all the benefits of a UMZV command. Simulations and experiments on a portable crane verified the key results.

5.3 Minimum-Impulse Multi-Mode Input Shaper

This section presents a new method to design input shapers for systems that have multiple natural frequencies. The primary goal of the analysis is to limit the number of impulses of the input shaper to n for a system that has $n-1$ natural frequencies. These new type of input shapers will be designated "minimum-impulse" input shapers. These shapers will have very short duration as compared to other conventional multi-mode input shaping

design techniques[3].

An introduction to multi-mode input shaping is given in Section 5.3.1. Then, the details of the new design technique will be given in Section 5.3.2 followed by a an example of the method for a two mode system in Section 5.3.3. The example two mode system will give a good framework for discussing the properties of the new minimum-impulse input shapers. Finally, experimental support for this two-mode example will be given in Section 5.3.4.

5.3.1 Multi-Mode Input Shaping

Most oscillatory systems are dominated by a single natural frequency, such as most cranes. However, some systems may have more modes that significantly affect the response of the system. For example, if a crane has a light payload (comparable to the hook), then a double pendulum effect can be experienced [51]. Or, if the payload is a large distributed inertia, a double pendulum effect can also arise [29]. This double pendulum contributes two significant natural frequencies to the payloads response.

There are a few existing techniques to find input shapers that suppress vibration for multiple modes. The simplest method is to convolve an input shaper designed to cancel one mode with another that cancels the other mode [48, 15]. Figure 5.30 shows how this is accomplished for two modes. The duration of the two-mode convolved shaper is the sum of the durations of the individual shapers. This fact usually means the convolved method has a relatively long duration, especially if robust input shapers such as ZVD and EI are used. However, the advantage of this method is they are simple to create. The designer only needs to find individual input shapers for both modes. Another advantage is that any

[3]The work in this section was completed in conjunction with Dr.Seong-Wook Hong and Mr.Sang-Won Park at Kumoh National Institute of Technology in Gumi, South Korea.

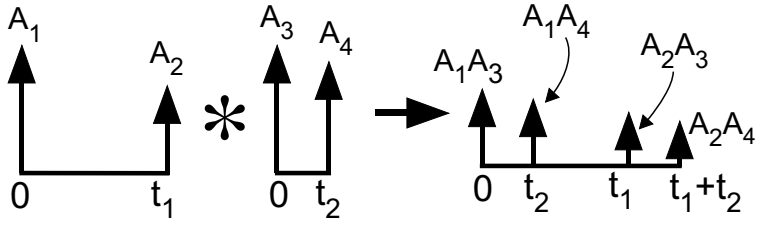

Figure 5.30: Convolution of two input shapers to form a two-mode shaper

type of shapers can be chosen, for example ZV-ZV or ZVD-ZVD, with no increase in design complexity.

Another method is to form a shaper by simultaneously solving constraint equations for two modes [48, 15, 32]. This will form a single input shaper that will reduce vibration for both modes. This type of input shaper is called a simultaneous two-mode shaper. Like the convolved method, the simultaneous method can be used to find any type of two-mode shaper: ZVD-ZVD, EI-EI, and so forth. The advantages are that it is often shorter than the convolved method. However, except for some special cases [36], it usually requires a numerical algorithm to solve the constraint equations.

Two methods that are similar to the method in this section have also been proposed. Singh uses a least common multiple of the periods of the natural frequencies in a system to generate an overall period [46]. The resulting input shaper has two impulses to cancel any number of natural frequencies in a system. A more robust three-impulse case is also presented. Tuttle uses a z-domain pole-zero cancelation approach to design multi-mode input shapers for various robustness levels [65]. Both of these methods are similar to the approach in this section, but approach the design of multi-mode input shapers in slightly different ways.

Finally, a specified insensitivity (SI) input shaper can be used for multiple mode input

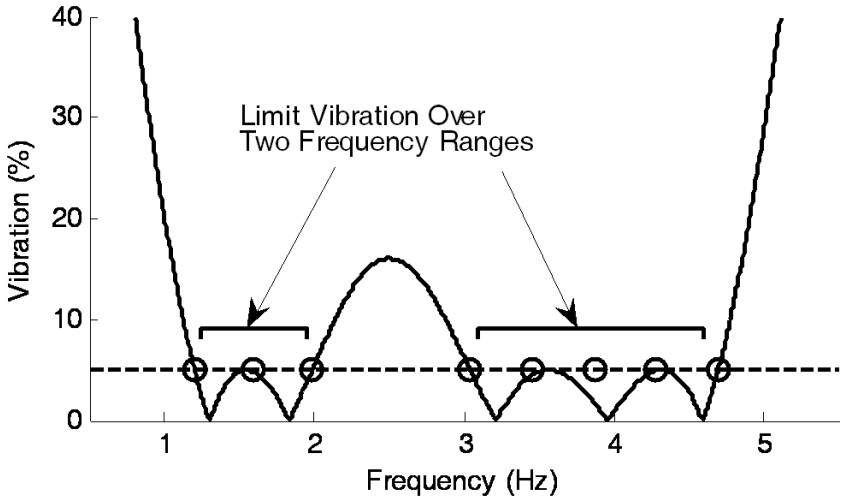

Figure 5.31: Creating a two mode SI shaper

shapers [51]. Figure 5.31 shows how an SI shaper can be used to limit residual vibration over two frequency ranges. The circles on the figure represent the frequencies at which vibration is limited by the constraint equations. By choosing two ranges of frequencies, the designer can robustly limit vibration for two separate modes.

In this section a new approach for designing multi-mode input shapers is presented. It is similar to the simultaneous method discussed previously in that the input shaper is determined for multiple modes simultaneously, but has a novel set of constraint equations. The main features of the new method are minimal number of impulses and provision of many possible solution sets at the same time. The proposed method is demonstrated with a two-mode shaper through a series of simulation and experiments.

5.3.2 Design Method

The main idea of the design is to use a minimum number of impulses to cancel a vibration in a multi-mode system. Each impulse of an input shaper is defined by two properties: its amplitude and timing. Since each mode of a system is also defined by two properties, its natural frequency and damping ratio, it is postulated that each impulse has the ability to cancel one mode. However, in order for cancelation to occur, the system has to be vibrating initially. This is the fundamental property of all input-shaping methods: use one impulse to cancel the vibration caused by an earlier one. Because of this, one additional impulse is needed to initially excite all modes. The first impulse of the input shapers serves this purpose[4]. Then, the remaining impulses can each cancel a single mode. Thus, an input shaper with n impulses is able to cancel $n-1$ vibration modes.

To begin the analysis, an expression for a series of n impulses of an input shaper can be written as:

$$I(t) = \sum_{i=1}^{n} A_i \delta\left(t - t_i\right) \tag{5.33}$$

where A_i is the impulse amplitude and t_i is the impulse time, with $t_{i-1} < t_i$, and δ is the unit impulse function. Assume, without loss of generality, that the first impulse starts at

[4]Remember, an impulse excites *all* modes of an oscillatory system equally.

time zero, i.e., $t_1 = 0$,. Then, (5.33) is rewritten in the Laplace domain as:

$$I(s) = \sum_{i=1}^{n} A_i e^{-t_i s} \tag{5.34}$$

The oscillatory system is assumed stable, so the associated under-damped eigenvalues can be written as:

$$s_k = \sigma_k + j\omega_{d,k} = -\zeta_k \omega_{n,k} + j\omega_{n,k}\sqrt{1-\zeta_k^2} \quad , \quad k = 1, 2, \ldots, n-1 \tag{5.35}$$

where ζ_k and $\omega_{n,k}$ are the k^{th} damping ratio and natural frequency of the system. The complex conjugate of each eigenvalue is also an eigenvalue of the system. For the remainder of this analysis, an i subscript will be used for input-shaper impulses and a k subscript will be used to denote system mode (natural frequency) numbers.

In order to eliminate the residual vibration of a multi-mode flexible system, the zeros caused by the input shaper in (5.34) should cancel the poles of the flexible system in (5.35). If the input shaper defined by (5.35) cancels the vibration modes of the plant it is applied to, then an arbitrary reference command that the input shaper is convolved with will also cancel the vibration modes [42]. Therefore, the following constraint on (5.34) is imposed:

$$I\left(s_k\right) = 0 \quad , \quad k = 1, 2, \ldots, n-1 \tag{5.36}$$

It is easy to see that that the complex conjugate poles, $\bar{s}$, also satisfy this equation. There are $n-1$ complex-valued nonlinear equations in (5.36), each of which provides two real-valued solutions for A_i and t_i. However, since the number of unknowns to be determined is $2n$, an additional constraint equation must be found to solve this problem. For input shaper design, this final equation is a constraint that the sum of the impulse amplitudes equal one:

$$\sum_{i=1}^{n} A_i = 1 \tag{5.37}$$

Now, (5.36) and (5.37) can be combined into a system of nonlinear equations:

$$\begin{bmatrix} 1 & 1 & 1 & \cdots & 1 \\ 1 & e^{-T_1 s_1} & e^{-T_2 s_1} & \cdots & e^{-T_n s_1} \\ 1 & e^{-T_1 s_2} & e^{-T_2 s_2} & \cdots & e^{-T_n s_2} \\ \vdots & \vdots & \vdots & \ddots & \vdots \\ 1 & e^{-T_1 s_n} & e^{-T_2 s_n} & \cdots & e^{-T_n s_n} \end{bmatrix} \begin{Bmatrix} A_0 \\ A_1 \\ A_2 \\ \vdots \\ A_n \end{Bmatrix} = \begin{Bmatrix} 1 \\ 0 \\ 0 \\ \vdots \\ 0 \end{Bmatrix} \tag{5.38}$$

The unknowns in this equation are the n impulse times (t_i) and amplitudes (A_i) of the input shaper. The solution to this equation will be an input shaper that suppresses vibration at $n-1$ oscillatory frequencies defined by s_k.

One straightforward method to numerically solve (5.38) is to nullify the norm of the left hand side minus the right hand side:

$$\text{norm}(\epsilon) = \text{norm}\left(\begin{bmatrix} 1 & 1 & 1 & \cdots & 1 \\ 1 & e^{-T_1 s_1} & e^{-T_2 s_1} & \cdots & e^{-T_n s_1} \\ 1 & e^{-T_1 s_2} & e^{-T_2 s_2} & \cdots & e^{-T_n s_2} \\ \vdots & \vdots & \vdots & \ddots & \vdots \\ 1 & e^{-T_1 s_n} & e^{-T_2 s_n} & \cdots & e^{-T_n s_n} \end{bmatrix} \begin{Bmatrix} A_0 \\ A_1 \\ A_2 \\ \vdots \\ A_n \end{Bmatrix} - \begin{Bmatrix} 1 \\ 0 \\ 0 \\ \vdots \\ 0 \end{Bmatrix} \right) \tag{5.39}$$

This solution method will be used to solve for a two-mode input shaper in the next section.

5.3.3 Two-Mode Example

This section will provide an example of the input shaper design method given above for a system with two natural frequencies. For this system, (5.39) reduces to:

$$\text{norm}(\epsilon) = \text{norm}\left(\begin{bmatrix} 1 & 1 & 1 \\ 1 & e^{-T_1 s_1} & e^{-T_2 s_1} \\ 1 & e^{-T_1 s_2} & e^{-T_2 s_2} \end{bmatrix} \begin{Bmatrix} A_0 \\ A_1 \\ A_2 \end{Bmatrix} - \begin{Bmatrix} 1 \\ 0 \\ 0 \end{Bmatrix} \right) \tag{5.40}$$

To provide an example solution to this equation, it will be assumed that the first frequency is $\omega_1 = 1$ Hz and the second higher frequency will vary from $\omega_2 = 1 \ldots 7$ Hz. Solutions to this equation are found using a recursive algorithm, starting at $\omega_1 = \omega_2 = 1$ Hz and steadily increasing ω_2 to 7 Hz. One solution to (5.40) at the initial condition is a ZV shaper

for $\omega = 1$ Hz[5]. However, for purposes of generating solutions to the recursive algorithm, a ZVD shaper will be used as an initial condition. A slight amount of damping, $\zeta \simeq 10e^{-4}$, was added to the oscillation modes to improve numerical stability of the algorithm.

Figure 5.32(a) shows the shaper duration from this solution as a function of the second natural frequency. A single solutions exist in a range between 1 and 3 Hz[6]. However, it is clearly seen that there exists more than one solution after 3 Hz. Three such solutions are shown in the figure. In general, the number of solutions increases as the ω_2 increases.

At ω_2=3 Hz, the fastest solution is a ZV shaper designed for a 1 Hz oscillation. The reason for this is that a ZV shaper will eliminate all odd multiples of its designed frequency. So, a ZV shaper designed for 1 Hz will eliminate vibration at 1 Hz, 3 Hz, etc. At ω_2=5 Hz, the fastest solution is a UMZV shaper designed for a 1 Hz oscillation. Similar to a ZV shaper, a UMZV shaper will cancel every other odd multiple of its designed frequency. In this case, a UMZV shaper designed for 1 Hz will cancel vibration at 5 Hz, 9 Hz, etc. Beyond 5 Hz, the shaper time duration is lower than the UMZV. In this case, impulses with magnitudes greater than one are introduced. For most actual systems, this is an unusable solution, because the input shaper might saturate the actuator [49].

Figure 5.32(b) shows a plot of how the impulse amplitudes for the fastest solutions (the solid line in Figure 5.32(a)) vary as ω_2 is increased. It is interesting that the impulse sequence is symmetric about the second impulse for all frequency pairs. That is $A_1 = A_3$. At $\omega_2 = 3$ Hz, the single-mode ZV solution, the second impulse amplitude is zero. Beyond this solution, negative amplitudes are introduced until at $\omega_2 = 5$ Hz, when the UMZV solution is reached. This solution lies on the boundary of applicable input-shaping solutions (the grey region represents solutions whose impulse amplitudes are greater than 1). For a system with a second frequency greater than 5 Hz, one of the other solution curves in Figure 5.32(a) must be used.

So far, the number of impulses, impulse amplitudes, and shaper duration have been

[5]The reader might notice that a ZV shaper has two impulses, not three like in (5.40). Therefore, for a ZV shaper to be a solution to this equation, one of the impulses will be equal to zero. (It will be seen later that $A_2 = 0$).

[6]For this initial condition, there is a single solution between 1 and 3 Hz. Other, longer shaper duration initial conditions would produce other other solutions in this frequency range.

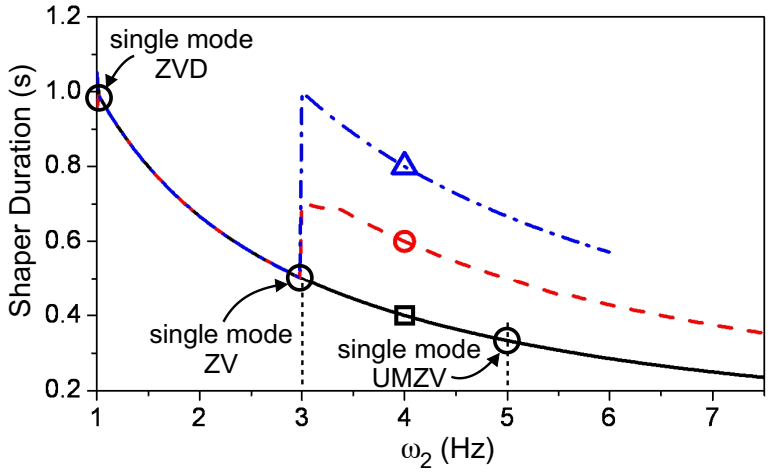

(a) Input shaper duration for the second frequency (T_2)

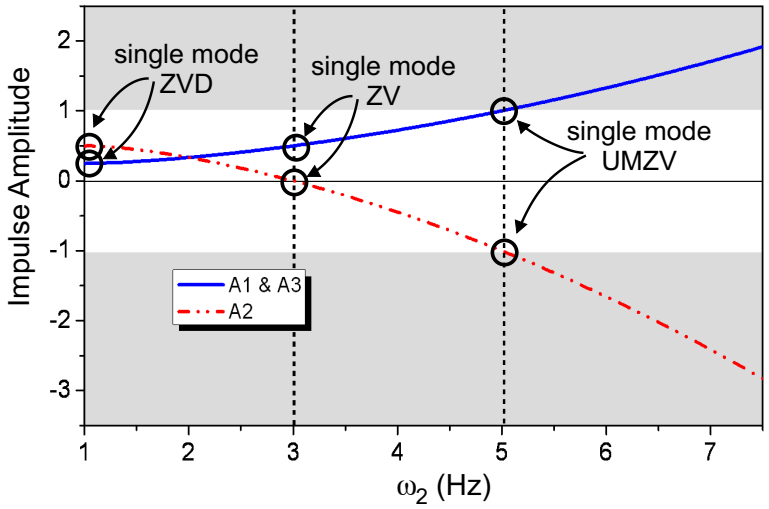

(b) The impulse amplitude of the input shaper vary as the second frequency

Figure 5.32: Two-Mode Minimum-Impulse Input Shaper Solution

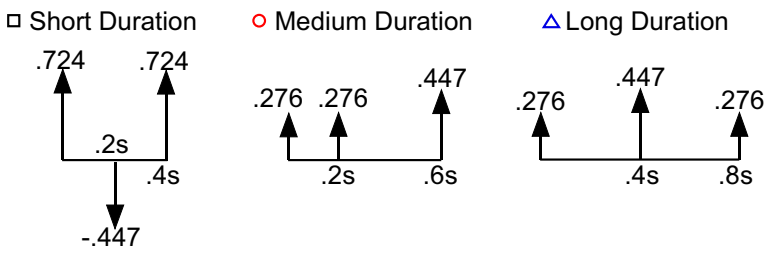

Figure 5.33: Three possible input shapers for ω_1=1Hz, ω_2=4Hz

discussed. Another important property of input shapers is their sensitivity to modeling errors. To investigate this issue, the robustness of three solutions to the minimum-impulse shaper are compared against other multi-mode input-shaping techniques, such as convolved ZV and multi-mode SI. A frequency pair of $\omega_1 = 1$ Hz and $\omega_2 = 4$ Hz will be examined. The minimum-impulse shaper solutions to this frequency pair are denoted on Figure 5.32(a) with a square, circle, and triangle. Figure 5.33 shows the numerical values for each of these solutions.

Figure 5.34 shows the sensitivity curve for the shortest input-shaper duration, 0.4s. From this plot it is seen that the shaper reduces the vibration at the design frequencies to zero, but as the frequency deviates from the design frequency, residual vibration increases significantly. The convolved 2-mode ZV has a duration of 0.625s and SI has a duration of 1.13s. Furthermore, at certain ranges the residual vibration increases beyond that of an unshaped command. This increase is a property of input shapers that contains negative impulses [49].

Figure 5.35 shows the sensitivity curve for the medium duration input shaper, 0.6s. Again, vibration is reduced to zero at the design frequencies. The insensitivity is only marginally improved over the short duration input shaper in the previous figure. However, because the input shaper contains only positive impulses, the vibration level is never above the unshaped command.

Finally, Figure 5.36 shows the sensitivity curve for the slowest duration shaper, 0.8s. The sensitivity of the shaper is improved considerably over the short duration shaper, but at the expense of a slower time response; it is twice as slow as the short duration. Table 5.2 summarizes the shaper durations and insensitivities for the five input shapers discussed in

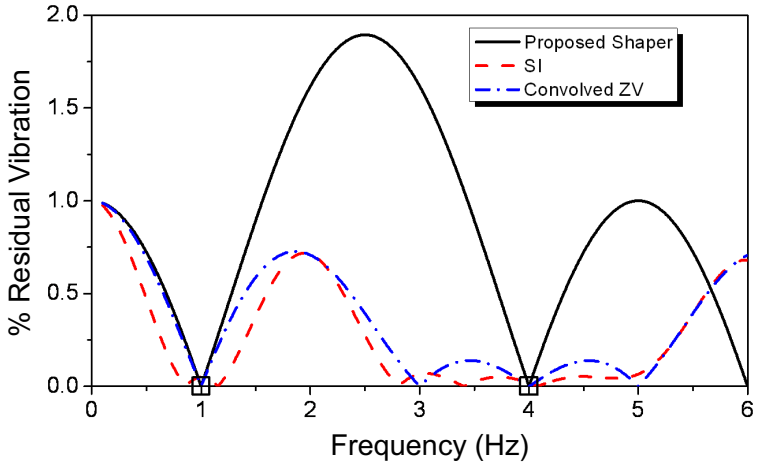

Figure 5.34: Sensitivity curve for $\omega_1 = 1$Hz, $\omega_2 = 4$Hz Short duration shaper

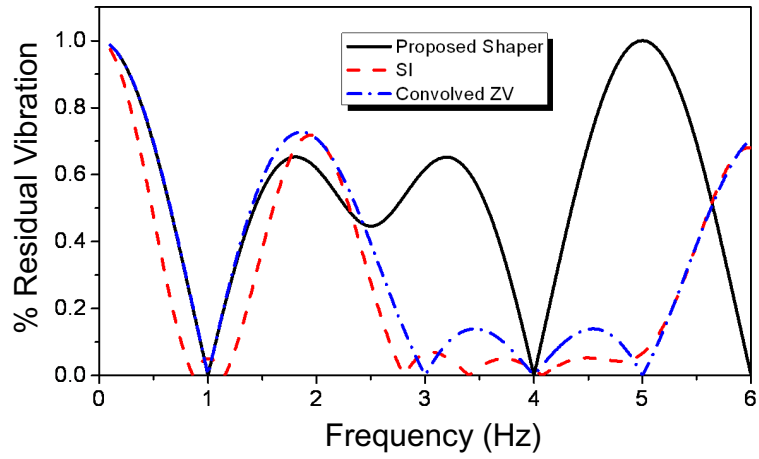

Figure 5.35: Sensitivity curve for $\omega_1 = 1$Hz, $\omega_2 = 4$Hz Medium duration shaper

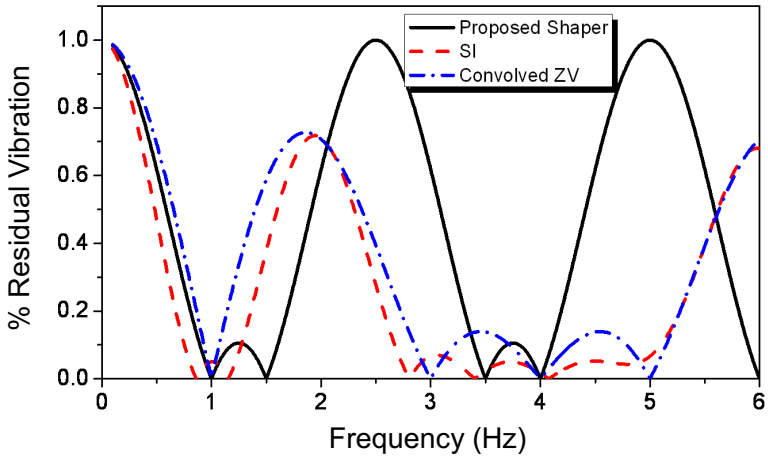

Figure 5.36: Sensitivity curve for $\omega_1 = 1$Hz, $\omega_2 = 4$Hz Long duration shaper

Table 5.2: Summary of Input Shaper Duration and Insensitivity for 1 Hz and 4 Hz System. (Ordered by Duration)

Shaper	Duration [s]	5% Insensitivity ω =1Hz	ω =4Hz
Min. Impulse Short	0.40	0.06	0.06
Min. Impulse Medium	0.60	0.07	0.07
Convolved ZV	0.63	0.07	0.26
Min. Impulse Long	0.80	0.13	0.13
SI (5% Ins.)	1.13	0.40	1.95

this section. Overall, the short duration minimum-impulse shaper is by far the fastest, but has the least amount of insensitivity. This shaper would be a good choice if both frequencies are known very well and are not expected to change. The other minimum-impulse shapers provide marginal improvements in low-mode robustness, and in general would provide few additional benefits over the short duration shaper. If extra robustness was needed, the minimum-impulse shaper would not be a good design choice and the SI shapers should be used.

5.3.4 Experimental Results

To confirm the theoretical performance of the new method, an experimental apparatus was built. As shown in Figure 5.37, the apparatus consists of a translating base mounted on a lead screw, whose motion is controlled by a motor. On the base are two flexible rods whose natural frequency can be tuned by changing the position of the masses along each rod. A laser scanning micrometer was used to measure the vibration response position of the rods.

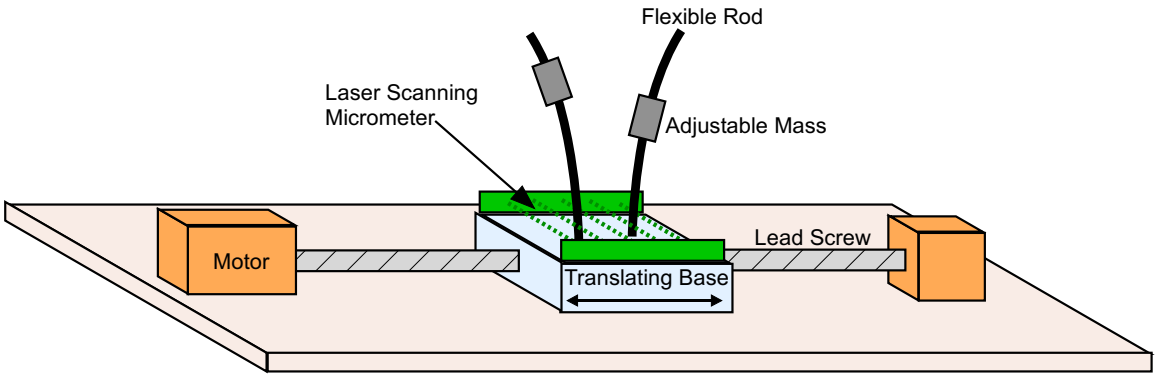

Figure 5.37: Diagram of Experimental Apparatus

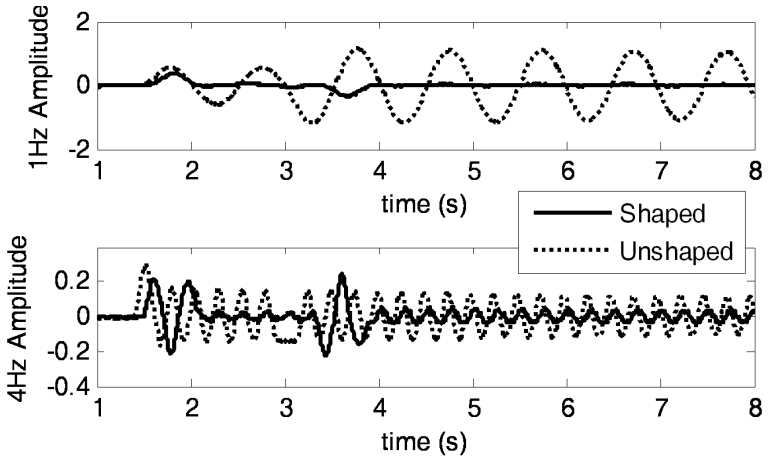

Figure 5.38: Experimental response of short duration shaper

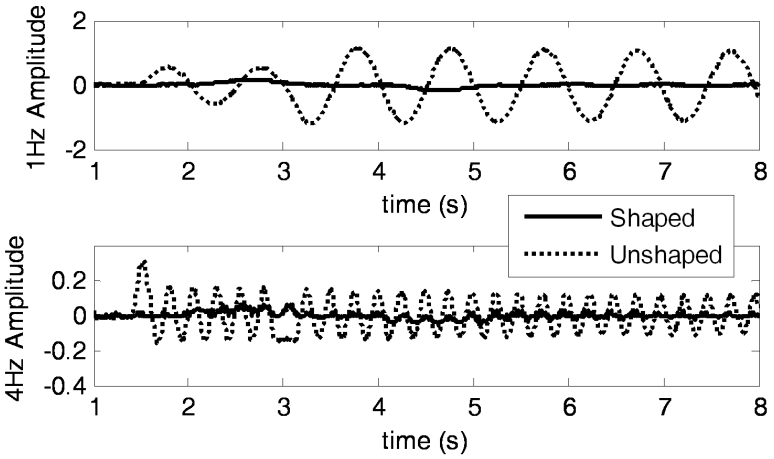

Figure 5.39: Experimental response of long duration shaper

The system was tuned so that the natural frequencies were $\omega_1 = 1$ Hz and $\omega_2 = 2$ Hz.

Each of the minimum-impulse shapers for a system with these two frequencies were tested on this device. The baseline command for the test was a pulse in velocity. Figure 5.38 shows the response of the system to the shortest duration shaper along with an unshaped response for comparison. While vibration of the low mode was canceled well, the high mode vibration was not. Because this input shaper is not very robust, a small modeling error in the shaper design will result in significant vibration. The experimental response of the long duration shaper is shown in Figure 5.39. As with the short duration shaper, the low mode is nearly eliminated. This time, the high mode vibration is successfully suppressed. This result demonstrates the increase in robustness of the longer duration shaper.

In conclusion, this section proposed a new formulation of the design method for multi-mode input shapers. The proposed "minimum-impulse" input shaper formulation limits the number of input-shaper impulses to n for an $n-1$ mode system. A solution method to this formulation was shown to have multiple solutions for some frequency pairs. A two-mode system was used to exemplify the characteristics of the new input-shaper design. It was shown that the shortest duration shapers from the solution method produce very fast shapers in comparison to other multi-mode design techniques, but at the cost of reduced robustness.

CHAPTER VI

APPLICATIONS ON AN INDUSTRIAL CRANE

This chapter presents an application of input-shaping and feedback control on an 35-ton industrial bridge crane at Logan Aluminum Inc, a leading manufacturer of aluminum sheet products. The crane controller installed on this crane features motion-induced oscillation reduction via input shaping, payload disturbance rejection via feedback control, an automatic positioning system, and an advanced operator interface. This controller is a good example application of some of the concepts presented in this thesis. A description of the crane is presented in Section 6.1. An explanation of how each of these control-system features was implemented on the crane is given in Section 6.1. Finally, results of performance evaluations are presented in Section 6.3[1].

6.1 System Description

Figure 6.1(a) shows a photograph of a bridge crane used primarily to transport cylindrical-shaped "rolls" to different machining and storage locations. A typical payload for this crane is depicted in the figure. The crane has a 35-ton capacity, and a Cartesian workspace of approximately 30 by 100 by 10-meters in the trolley, bridge, and hoisting directions, respectively.

The bridge and trolley of the crane is actuated with AC-induction motors. The motors are controlled by vector drives, meaning the motors can follow continuously variable velocity commands. The maximum transverse speeds of the crane is approximately 1.0 m/s.

Prior to installation of the crane control system, operators actuated the crane by issuing commands from a lever interface, like the one shown in Figure 6.1(b). These commands were directly sent to the crane drives. A model of this actuation process is illustrated with the block diagram of Figure 6.2. The DM block represents the behavior of the vector *drives*

[1]The contents of this chapter were created in conjunction Khalid Sorensen.

(a) Industrial Bridge Crane at Logan Aluminum

(b) Lever Crane Interface. Courtesy of Magnetek

Figure 6.1: Industrial Bridge Crane and its Controller Interface

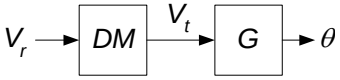

Figure 6.2: Crane Actuation Block Diagram

and AC-induction *motors*. This plant accepts reference velocity commands, V_r, issued to the crane by a human operator, and converts these signals to the actual velocity of the overhead trolley, V_t. Because the payload of the crane is a long distributed mass, a double-pendulum is created by the hook and payload. Therefore, motion of the trolley causes the hook to swing with an angle θ_h and the payload to swing with an angle θ_p. This behavior is represented by the block, G (the output of block G in Figure 6.2 is shown as θ, which represents both swing angles).

6.1.1 Dynamic Model of Industrial Cranes

The behavior of AC-induction motors and vector drives is nonlinear. However, this behavior can be accurately modeled by combining several simpler nonlinear components [62]. The DM block of Figure 6.2 is expanded in Figure 6.3 to reveal such a model.

The model is comprised of four elements: a saturator, a switch, a rate limiter, and a heavily damped second-order plant, H. The saturation element truncates excessive velocity

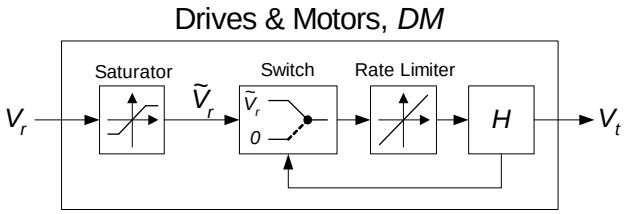

Figure 6.3: Expanded View of the Drives and Motors Block

commands to the crane, while the rate limiter places upper and lower bounds on the acceleration of the crane. H serves to mimic the smoothing effect caused by the inertia of the motors and crane. The function of the switching element is to pass the reference signal, $\widetilde{V}_r$, to the rate-limiting block. However, when positive-to-negative transitional velocity commands are issued to the crane, the switch temporarily sends a signal of zero. Transitional velocity commands are those commands that change the direction of travel of the crane (forward to reverse or vise versa). This type of behavior depends on $\widetilde{V}_r$ and V_t, and can be described with the following switching rules:

$$Switch = \begin{cases} \widetilde{V}_r, & \text{Sign}(\widetilde{V}_r) = \text{Sign}(V_t), \\ \widetilde{V}_r, & |V_t| \leq X, \\ 0 & \text{otherwise.} \end{cases} \tag{6.1}$$

This model may be used to represent the behavior of the Logan crane drives and motors by properly selecting the five parameters associated with the model: p - the saturation threshold, X - the switching threshold, a_{max} - the magnitude of the acceleration limiter, ζ_H - the damping ratio of H, and ω_{nH} - the natural frequency of H. For the Logan crane, these parameters were estimated to be 0.75 m/s, 0.038 m/s, 0.63 m/s^2, 0.75, and 3.7 rad/s, respectively. Figure 6.4 compares the response of the model and the response of the actual system to several velocity commands.

When the motors move the crane, oscillations are induced into the hook and payload. As previously illustrated in Figure 6.2, the angular response of the hook and payload to motion of the trolley is modeled by the plant, G. The oscillatory behavior of the hook and

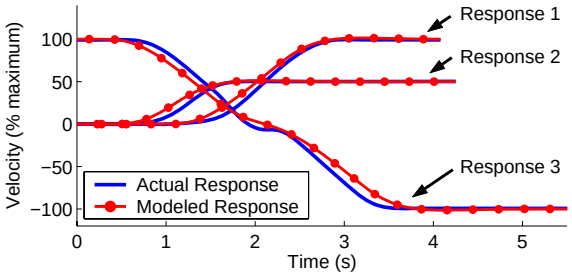

Figure 6.4: Comparison of the actual and modeled responses of the drives & motors to different velocity commands. (1) Response to a step of 100% velocity. (2) Response to a step of 50% velocity. (3) Response to a step from 100% velocity to -100% velocity.

payload can be described by two linear equations of motion [51]:

$$\begin{aligned} \ddot{\theta}_h(t) + \left(\tfrac{g}{L_h}\right)\theta_h - \left(\tfrac{gM}{L_h}\right)\theta_p &= -\tfrac{u(t)}{L_h} \\ \ddot{\theta}_p(t) - \left(\tfrac{g}{L_h}\right)\theta_h + \left(\tfrac{g}{L_p} + \tfrac{gM}{L_p} + \tfrac{gM}{L_h}\right)\theta_p &= \tfrac{u(t)}{L_h} \end{aligned} \tag{6.2}$$

Closed-form expressions for the oscillatory frequencies can be obtained from (**??**) as:

$$\omega_{1,\,2} = \sqrt{\frac{g}{2}}\sqrt{(1+M)\left(\frac{1}{L_h}+\frac{1}{L_p}\right) \mp \beta} \tag{6.3}$$

where g is the acceleration due to gravity, and

$$\beta = \sqrt{(1+M)^2\left(\frac{1}{L_h}+\frac{1}{L_p}\right)^2 - 4\left(\frac{1+M}{L_p L_h}\right)} \tag{6.4}$$

6.2 Integration of the Crane Control System

A topological illustration of the crane control system is shown in Figure 6.5. This figure depicts the elements that comprise the system:

- A control architecture for enabling swing-free motion and precise payload positioning.
- A touchscreen human-machine interface for aiding precise positioning of the crane.
- A standard lever interface.
- A machine vision system for sensing hook swing.
- Laser range sensors for measuring crane position.

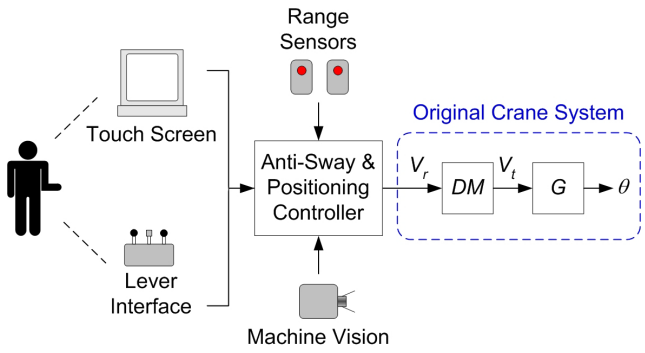

Figure 6.5: Components of the Crane Manipulation System.

The principal element of the control system is the anti-sway and positioning control. For the Logan crane, a programmable logic controller (PLC) was used to program the control law and handle the input/output of the system. The PLC accepts inputs from the other elements: motion commands from the three interface devices, crane position information from the laser range sensors, and hook displacement information from the machine vision system. The information from these elements is used by the control system to produce low-sway velocity commands, which are issued to the crane drives. The following subsections provide greater detail about each control system element.

6.2.1 Human-Machine Interface

The three-lever interface shown previously in Figure 6.1(b) permits the bridge, trolley, and hook to be commanded independently from each other by their respective actuation levers. An additional visual touch-screen interface was installed with the crane control system. The motivation for implementing the visual interface is to improve the way operators control the crane. Specifically, to simplify positioning of the crane.

In many applications, precise and repetitive payload positioning is required. The visual interface is a real-time graphical representation of the crane and crane workspace that permits operators to store desired payload destinations, and also command the crane to travel to these locations [63, 61]. To store a payload destination for future use, an operator first manually positions the crane in this location. Then, the coordinates corresponding to the position are stored in the visual interface. A target image represents the location on

the touchscreen. Operators specify a desired hook destination by touching a stored target that is displayed in the graphical workspace image. Once the operator specifies the desired destination, the feedback control system automatically drives the crane to the specified location without payload sway.

For precise positioning applications, the visual interface yields significant efficiency advantages over traditional manual control [61]. This is because operators using the interface can automatically position the crane at a desired location in a nearly time-optimal and swing-free manner. Manual positioning is more difficult. Operators must have extensive training. Often, the structures are moved very slowly to ensure accurate and safe positioning.

A visual interface, similar to the one described here, was installed on a 10-ton industrial bridge crane located at the Georgia Institute of Technology. Operator studies conducted on this crane revealed that operators using the visual interface completed positioning tasks 5% to 45% more quickly than with manual control [61].

6.2.2 Feedback Control Components

Machine Vision System

Sensory information about hook swing is obtained by using machine vision technology. The camera used for this application was a Siemens 720-series vision system. This camera is a stand-alone image sensor with on-board image acquisition, processing, and communication capabilities. The vision system is mounted on the trolley, near the fulcrum of the hook suspension cables, and oriented to view the hook and surrounding workspace. In this downward-looking configuration, the top of the crane hook is always within the camera field-of-view. A photograph of the trolley-mounted camera assembly is shown in Figure 6.6.

To facilitate reliable hook tracking, a light-emitting-diode (LED) array was installed next to the camera. When the vision system acquires an image, the LED array simultaneously pulses (similar to a flash bulb on a camera). Fiducial markers made of retro-reflective material, and mounted to the top of the hook, reflect the pulsed light back to the camera lens. By so doing, the fiducial markers are easily discernable from other features in the

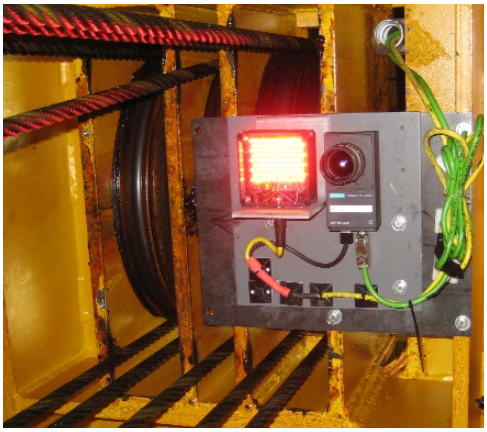

Figure 6.6: Camera and LED Array Mounting Configuration.

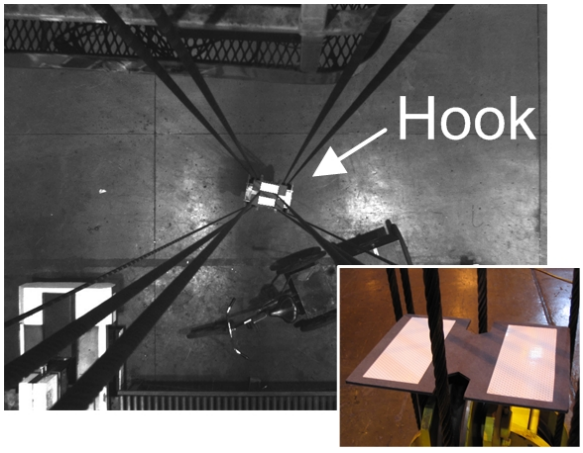

Figure 6.7: Image captured and processed by the machine vision system (large photo). Close up photograph of the fiducials mounted on the hook (sub photo).

Figure 6.8: Banner LT7 Laser for Measuring the Position of the Bridge.

image. An image acquired from the camera, and a close up view of the fiducial markers on this crane are shown in Figure 6.7.

Laser Range Sensors

Absolute bridge and trolley positions are measured by two Banner LT7-series laser range sensors. These position sensors have a range of 250 m and a resolution of approximately 1 mm. Both sensors are mounted on the bridge. One is oriented to detect the position of the trolley along the bridge. The other is oriented to detect the position of the bridge along the stationary runways. A photograph one of the mounted lasers is shown in Figure 6.8.

6.2.3 Anti-Sway & Positioning Control

A block diagram of the anti-sway and positioning control is shown in Figure 6.9. This block diagram depicts a control architecture where the original crane system is integrated into a two-loop feedback structure. The controller generates reference velocity commands that, when issued to the drive and motors, DM, achieve three desirable results in the payload: 1) input shaping control, 2) precise positioning capability, and 3) disturbance rejection.

Input Shaping Control

Input shaping control was incorporated into the control structure by including an input shaper into the signal path. In Figure 6.9, the input shaper is represented by the block labeled IS. This shaper is designed to negate the oscillatory dynamics of the closed-loop transfer function formed by the disturbance rejection feedback loop. The input shaper accepts commanded velocity signals, $\widetilde{V}_c$, from one of three elements. If the crane is being

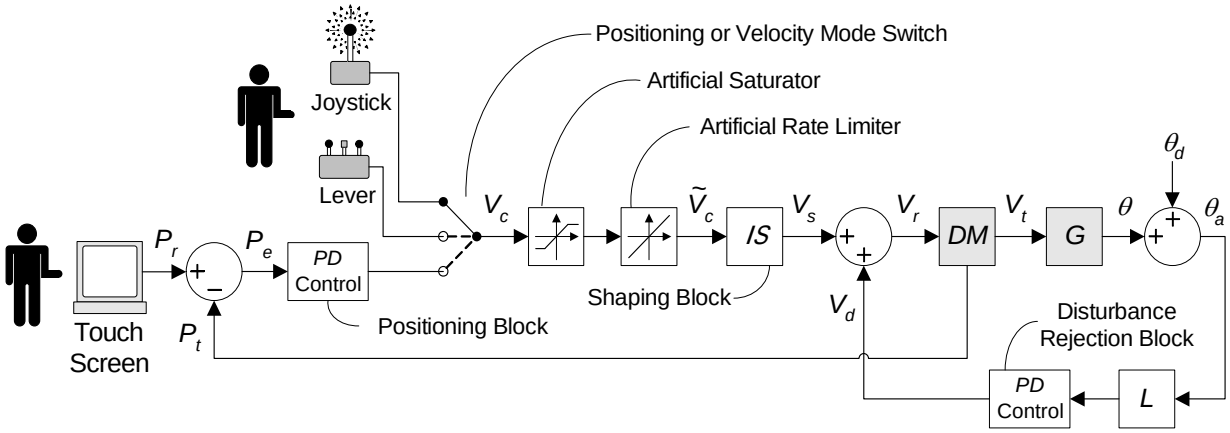

Figure 6.9: Anti-sway & Positioning Controller

manually manipulated, then signals from the lever interface are issued to the input shaper. If the crane is being automatically positioned through the use of the touchscreen, then signals from a positioning control block are issued to the shaper. The shaped commands, V_s, are then used as reference commands for the disturbance rejection loop.

While input shaping works effectively for linear systems, the drives and AC-induction motors that actuate the Logan cranes exhibit noticeable nonlinear behavior. The predominant effect of this behavior can be modeled by saturation and rate limiting elements within the block, DM, [57, 9]. Mitigating the effects of an rate limit, or acceleration limit for the crane discussed in this chapter, for common input shapers was discussed previously in Chapter 5, Section 5.1. In that section, a method to modify common input shapers to compensate for the acceleration limit of the machine.

Another strategy to mitigating the effects of saturation and rate limiting within the DM block was presented in [58]. This method works by adding an artificial saturation element and an artificial rate limit element into the control block diagram such that these elements filter reference commands before they are modified by the input shaper. By so doing, the shaped command generated by the input shaper will not be corrupted by the saturation and rate limit elements contained in the drives and motors. The saturation and rate limiting parameters of the artificial elements must be equal to, or more conservative than, the actual saturation and rate limiting parameters. Therefore, time-optimal commands are not

generated, but this method is easier to implement than that in Chapter 5.

Precise Payload Positioning

When an operator controls the crane by using the visual interface, position reference commands are issued to control system. Given that a payload eventually comes to rest directly beneath the overhead trolley, final positioning of the trolley is equivalent to final positioning of the payload. Therefore, precise payload positioning is accomplished by using position information from the laser range sensors to control the position of the trolley.

In response to the positioning error, a proportional-derivative (PD) control block generates a velocity signal that attempts to drive the crane toward the desired location. If this signal were issued directly to the drives and motors, then the objective of trolley positioning would be accomplished, but, noticeable hook swing would be exhibited. However, because the input shaper filters these commands, the dual objective of driving the crane toward a desired position, while also preventing motion-induced oscillation is achieved.

Disturbance Rejection

While the primary source of cable sway is command-induced oscillation, secondary sources of oscillation, such as external disturbances, or unmodeled dynamics also contribute to undesired hook swing. Disturbance rejection is accomplished by making use of the machine vision system to provide sensory feedback of the actual hook angle, θ_h. For small hook angles, the horizontal displacement of the hook from the vertical at-rest position can be reasonably estimated by $L\theta_h$. This quantity is utilized in a PD block, which generates corrective velocity commands to damp out the disruptive oscillations. These signals are added to the shaped velocity signals, V_s, obtained from the input shaper. The combined signal is then issued to the system drives.

Although the drives and motors used on the Logan cranes exhibit nonlinear behavior, these components do operate within their linear regions frequently. Therefore, during these periods of time, superposition holds. Thus, because the signal, V_s continually drives the crane toward a desired set point, and the signal, V_d, attempts to damp out oscillation, the controller will achieve the dual objectives of positioning and disturbance rejection.

6.2.4 Beneficial Attributes of Combining Input Shaping with Feedback Control

The control architecture presented in the previous subsection allocates the task of motion-induced oscillation suppression to the input shaping filter. Disturbance-induced oscillation suppression is achieved through feedback control. While feedback *alone* could suppress both motion and disturbance-induced payload swing, beneficial system behavior is exhibited when these tasks are separated [30, 16].

Input shaping reduces motion-induced oscillation in an *anticipatory* manner, as opposed to the *reactive* manner of feedback control. Oscillation suppression is accomplished with the *reference* signal that anticipates the oscillation before it occurs, rather than with a *correcting* signal that attempts to restore deviations back to a reference signal. In the context of crane control, this means that motion-induced oscillation can usually be suppressed within one-half period of oscillation when using input shaping. To achieve similar performance with feedback control, aggressive gains must be used, which results in higher actuator effort, and greater command distortion than when using input shaping.

Another beneficial consequence of allocating motion-induced oscillation suppression to an input shaping filter is related to the double pendulum of the payload. In this case, aggressive disturbance rejection feedback gains will cause the nonlinear drives and motors of the crane to exhibit limit cycling. By utilizing input shaping, motion-induced oscillation suppression of the multi-mode system can be quickly suppressed without aggressive feedback control gains.

This combination of feedback and input-shaping control architecture presented here could be used on the mobile boom crane discussed in Chapter 4.

6.3 Performance Evaluation

The anti-sway and positioning capabilities of the Logan crane controller were rigorously tested. Section 6.3.1 discusses motion-induced oscillation suppression via input shaping. Section 6.3.2 discusses disturbance rejection via feedback control. Finally, Section 6.3.3 discusses positioning.

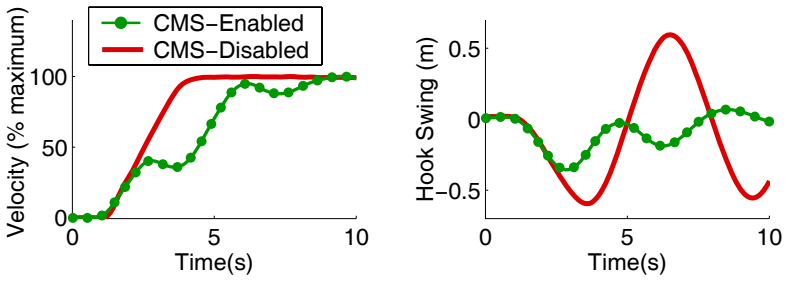

(a) Velocity Response of the Crane (b) Hook Swing Response of the Crane

Figure 6.10: Motion-Induced Oscillation Suppression With and Without CMS Enabled

6.3.1 Input Shaping Oscillation Suppression

To evaluate the performance of input shaping, the crane was driven both with and without the input-shaping portion of the control architecture enabled. In the first set of tests, input shaping is disabled. Then, a step command in velocity was issued to the system while the hook swing in the bridge direction was measured. The same test is then repeated with input shaping enabled.

The response of the crane to this test is shown in Figure 6.10. The velocity response of the bridge is shown in Figure 6.10(a). In the figure, the acronym CMS stands for Crane Manipulation System, a shorthand for the control system in Figure 6.9. The motion of the hook is shown in Figure 6.10(b). The solid lines represent the bridge and hook motion when input shaping was disabled, the dotted lines represent the bridge and hook motion when input-shaping was enabled. Note that with input shaping enabled, the bridge motion is noticeably different and caused much less hook swing.

Similar results were obtained when these tests were repeated in the trolley direction, and simultaneously in the trolley and bridge directions. The graphs in Figure 6.11 summarize the swing amplitude results from each of these tests. The vertical axis of each graph represents the amplitude of residual hook swing.

Another set of tests were conducted where a pulse in velocity was issued to the crane. The swing amplitude results of these tests are summarized in the bar graphs of Figure 6.12. The results summarized in Figure 6.11 and 6.12 demonstrate that the new control system on the crane can reduce motion-induced oscillation by roughly 90%.

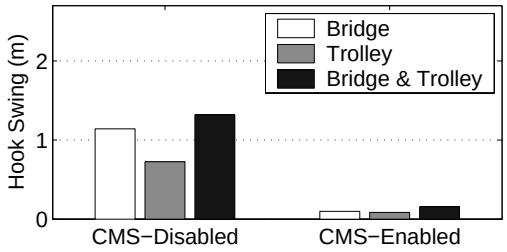

Figure 6.11: Residual Hook Swing Amplitude After a Step Velocity Command was Issued to the Crane

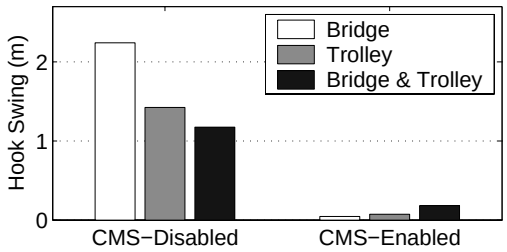

Figure 6.12: Residual Hook Swing Amplitude After a Pulse Velocity Command was Issued to the Crane

6.3.2 Disturbance Rejection

The disturbance rejection capabilities of the control system were evaluated by imparting an initial hook swing to the system and recording the response of the crane when the control system was activated. This experiment was repeated at several different suspension cable lengths ranging from 10m to 3m.

A typical response to this experiment for the maintenance crane is shown in Figure 6.13. The bridge position is shown with the solid line and the payload position is shown with the dotted line. The control system was activated at approximately time $t = 6s$. The hook oscillations were mostly damped out by time $t = 17s$, a time duration of approximately two oscillation periods.

6.3.3 Positioning Capabilities

The positioning capabilities of the control system were evaluated by issuing several reference positions to the cranes. The automatic control drove the cranes to the desired positions, while limiting motion-induced and disturbance-induced oscillations. The final positioning

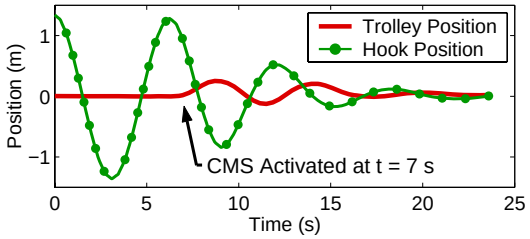

Figure 6.13: Cancelation of Disturbance-Induced Oscillations

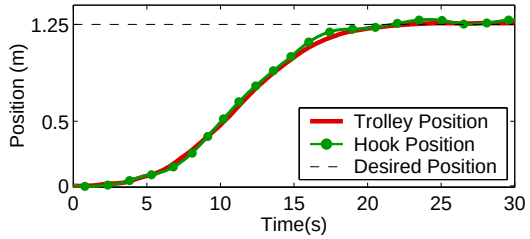

Figure 6.14: Trolley Response to a Position Command of 1.25 m

error was recorded for each trial.

The response of the crane to a typical position command is shown in Figure 6.14. This figure depicts motion in the trolley direction only, but each test required the crane to be positioned simultaneously in both the trolley and bridge directions. For the trial depicted in Figure 6.14, the trolley started at the 0 m location and was then commanded to move to the 1.25m m location. The solid curve represents the position of the trolley throughout the experiment; the dotted curve represents the position of the hook.

The positioning capabilities of the control system are summarized in Figure 6.15. The vertical axis of the figure is the final radial positioning error between the desired crane position and the actual crane position. Based upon these results, the average radial positioning

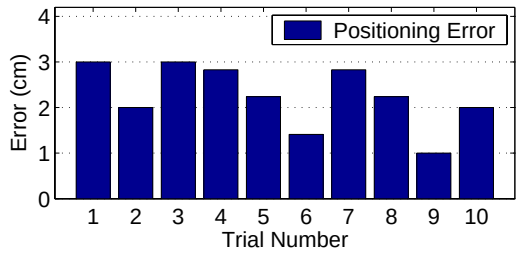

Figure 6.15: Final Positioning Error Measured Radially from the Desired Position to the Actual Crane Position

error for the crane is approximately 2 cm with a standard deviation of approximately 1 cm.

To summarize, a control system was developed and implemented on an industrial bridge crane. The system is comprised of a machine vision system for sensing hook position, laser range sensors for obtaining bridge and trolley positions, a visual touchscreen interface for simplifying positioning tasks, and an anti-sway/positioning control law. The new control system enables operators to manipulate the crane in a nearly swing-free manner. Motion-induced oscillations of the hook were reduced by roughly 90% through input-shaping control. The control can also reject externally-induced hook swing. Precision positioning of the hook was demonstrated with positioning capability on the order of a few centimeters. The control system architecture developed in this section, especially the operator interface features, can also be implemented on the mobile boom crane in Chapter 4. This implementation could be done by adapting the control laws to compensate for the nonlinear dynamics and by adding support for Cartesian motion transformation and feedback-linearization discussed in Chapter 3.

CHAPTER VII

CONCLUSION

Boom cranes are ubiquitous in construction and other industries and as such maximizing their performance is important. One limitation to most boom cranes is that they are usually attached to a stationary base. This thesis presented an analysis of mobile boom crane and its dynamics with a focus on applying input-shaping control to reduce oscillation. Additionally, a significant portion of the thesis dealt with designing input shapers for nonlinear and multi-mode systems.

Chapter 1 explained how standard boom cranes work and existing techniques to control their oscillation. A review of input-shaping control was also given. The time and frequency domain properties of common input shapers were discussed, such as ZV, ZVD, UMZV, EI, and SI.

A derivation for the equations of motions for a mobile boom crane was given in Chapter 2. Kane's method was used to derive the equations, but to validate the model the equations were compared to analogous equations of motion derived from Lagrange's Equations. Further validation of the model was given by comparing the equations of motion for the mobile boom crane to that of a stationary boom crane and a bridge crane.

Chapter 2 also presented a detailed analysis of luffing motions of a boom crane, and the challenges associated with accurately controlling luffing motion. It was shown that standard input-shaping methods work well on luffing motions, despite minimal compensation for the payloads nonlinear dynamics.

Finally in Chapter 2 an analysis of the effects of vertical acceleration on a pendulum is given. Motivated by vertical accelerations experienced by the boom crane payload on luffing motion, the analysis shows that pulses and steps in vertical acceleration change the frequency, amplitude, and phase of the pendulum. If these steps and pulses are applied at the correct point in the pendulum's swing, then reduction in the oscillation amplitude is

possible.

A method for operating a boom crane in Cartesian motions was explained in Chapter 3. The coordinate transformation will improver operator performance of a boom crane, especially operators who are standing on the ground and not rotating with the base of the crane. It was also shown that the coordinate transformation was also a feedback-linearization controller that could improve the performance of input shaping and other linear control techniques on the boom crane.

Chapter 4 reviewed the design of a small-scale mobile crane for research and education applications. Motivated by similar small-scale bridge and tower cranes already built, the mobile boom crane is meant to allow researchers and educations the opportunity to test control and operating strategies for this unique dynamic system

Input Shaping is a control technique that works best with linear systems. In Chapter 5, two methods for designing input shapers for specialized nonlinear systems were presented. The first method compensates for a system with a constant acceleration limit. Constraint equations were developed that modified standard input shapers to compensate for the limit. It was shown that compensated ZV, EI, and SI input shapers performed significantly better than their uncompensated counterparts.

The second nonlinear system analyzed was a system that has an unsymmetrical acceleration/braking dynamic. Approximated by a first order filter, the acceleration and braking nonlinearity was shown to be specifically detrimental to UMZV input shapers and slightly detrimental to ZV input shapers. As the disparity between acceleration and braking increased, the negative effect on the UMZV input shaper was more significant. A linear analysis of the nonlinearity was used to derive a new definition of the UMZV input shaper that compensates for the nonlinearity.

The final section in Chapter 5 discusses a new way of developing input shapers for multi-mode systems. A new set of constraint equations is presented that generate input shapers with a minimum number of impulses. Specifically, n impulses are required to reduce vibration for $n-1$ modes. The new type of input shapers were also shown to have very short durations compared to existing multi-mode input-shaping techniques. The trade-off

is that the new input shapers have poor sensitivity to frequency variations.

Finally, in Chapter 6, an application of feedback control, input shaping, and an advanced operator interface on an industrial crane was discussed. The control system developed was shown to perform well at reducing payload oscillation of the crane from motion-induced oscillation and disturbance-induced oscillation. Additionally, precise positioning of the crane was implemented on the controller.

APPENDIX A

KANE'S METHOD SOURCE CODE

This is the source code used to derive the equations of motions for a mobile boom crane using Kane's method and *Autolev*:

```
% File: mobile_boom2.al
% Generates equations of motion for MATLAB simulations of
% a Mobile Boom Crane
% Jon Danielson
% March 4, 2008
Autoz off
%%%%% Newtonian bodies, frames, particles, and points %%%%%
Newtonian N                 % Newtonian reference frame
Bodies cart, boom, cable    % cart, boom, and cable are bodies
Frames thetaboom, cablephi, gammaboom   % Intermediate frame
Points B, C                 % reference points
Particle P                  % treat payload as point mass
%%%%%% Variables, Constants, and Specified %%%%%%
Motionvariables' phi'', beta''
Constants G             %gravity
Constants h, r, a       %height of boom base, boom length, base offset
                        %specified inputs to system
Specified x'', y'', psi'', theta'',gamma'',l'', mp
%%%%%%% Mass and Inertia %%%%%
Mass cart = 0, boom=0, P=mp
Mass cable = 0                  % cable is massless
Inertia cart,  0,0,0
Inertia boom,  0,0,0
Inertia cable, 0,0,0

%%%%% Rotation Matrices %%%%%
Simprot(N,cart,3,psi)           %rotate cart
Simprot(cart,thetaboom,3,theta)     %rotate jib
Simprot(thetaboom,boom,-2,gamma)    %luff jib
Simprot(boom,gammaboom,2,gamma)     %we want the payload to swing in
                                    %reference to vertical, not normal to jib,
                                    %so we create a frame that is always
                                    %negative of the luft angle, gamma.
Simprot(gammaboom,cablephi,1,beta)  %    "   "
Simprot(cablephi,cable,-2,phi)      %swing of payload

%%%%%% Position Vectors %%%%%%
P_NO_cartO> = x*N1> + y*N2>     % from origin to cart center
```

```
P_cart0_B> = a*cart1>+h*cart3>      % from cart origin to base of boom
P_B_C> = r*boom1>           % from crane center to trolley/jib end
P_B_boom0> = 0.5*r*boom1>       % from crane center to jib center of mass
P_C_cable0> = -0.5*l*cable3>        % from boom end to cable center of mass
P_C_P> = -l*cable3>         % from boom end to payload
paypos> =express(P_N0_P>,N)     % express position of payload in newtonian
                                %frame
%%%%% Angular Velocities %%%%%
W_cart_N>   =  psi'*N3>                              % of cart
W_boom_N>   =  W_cart_N> + theta'*cart3> - gamma'*thetaboom2>
W_cable_N> =  W_boom_N>   + beta'*gammaboom1>   -  phi'*cablephi2>% of cable

%%%%%% Velocities %%%%%%
%V_boom0_N> = Dt(P_N0_boom0>,N)
%V_C_N> = Dt(P_N0_C>,N)  %v2pts(N,boom,N0,C)
V_P_N> = Dt(paypos>,N)  %v2pts(N,cable,C,P)

%%%%%% express velocities in newtonian frame%%%%
myvel> =express(V_P_N>,N)

%%%%%% Acceleration %%%%%%
A_P_N> = Dt(V_P_N>, N)

%%%%% Forces %%%%%%
Gravity(-G*N3>)
%%%%%% Equations of Motion %%%%%%
Zero = Fr() + FrStar()
Kane()

%Generate MATLAB code for simulation
UnitSystem kg,meter,sec
Input G = 9.8 m/sec, r=1 m
Input beta = 0 deg, beta' = 0 rad, phi = 0 rad, phi' = 0 rad
Output T sec, theta rad, beta rad, gamma rad, beta' rad, phi' rad
CODE Dynamics() mobile_boom2.m
save mobile_boom2.all
```

The equations of motion are:

$$
\begin{aligned}
&-\ell\cos(\phi)\ddot{\beta} = \\
&\frac{1}{2}\ell\dot{\psi}\dot{\theta}\sin(\phi-2\beta)+G\sin(\beta)-\frac{1}{4}\ell\dot{\theta}^2\sin(\phi+2\beta)+\ell\dot{\psi}\dot{\phi}\cos(\phi-\beta)+\ell\dot{\psi}\dot{\phi}\cos(\phi+\beta)+2\dot{\ell}\cos(\phi)\dot{\beta} \\
&\quad+\frac{1}{2}r\ddot{\theta}\cos(\gamma+\beta)+\frac{1}{2}r\ddot{\theta}\cos(\gamma-\beta)+\dot{\ell}\dot{\theta}\sin(\phi-\beta)+\frac{1}{2}r\ddot{\psi}\cos(\gamma+\beta)+\dot{\ell}\dot{\theta}\sin(\phi+\beta) \\
&+\dot{\ell}\dot{\psi}\sin(\phi-\beta)+\dot{\ell}\dot{\psi}\sin(\phi+\beta)+\ell\dot{\theta}\dot{\phi}\cos(\phi-\beta)+\ell\dot{\theta}\dot{\phi}\cos(\phi+\beta)-2\ell\sin(\phi)\dot{\beta}\dot{\phi}+\frac{1}{2}\ell\ddot{\theta}\sin(\phi-\beta) \\
&-\frac{1}{4}\ell\dot{\psi}^2\sin(\phi+2\beta)+\frac{1}{2}\ddot{y}\cos(\psi+\theta-\beta)+\frac{1}{4}\ell\dot{\psi}^2\sin(\phi-2\beta)+\frac{1}{2}\ddot{y}\cos(\psi+\theta+\beta)+\frac{1}{4}\ell\dot{\theta}^2\sin(\phi-2\beta) \\
&\quad+\frac{1}{2}a\ddot{\psi}\cos(\theta-\beta)+\frac{1}{2}a\dot{\psi}^2\sin(\theta+\beta)+\frac{1}{2}a\dot{\psi}^2\sin(\theta-\beta)+\frac{1}{2}\ell\ddot{\theta}\sin(\phi+\beta)+\frac{1}{2}\ell\ddot{\psi}\sin(\phi-\beta) \\
&\quad-\frac{1}{2}r\dot{\gamma}^2\cos(\gamma-\beta)+\frac{1}{2}r\dot{\gamma}^2\cos(\gamma+\beta)+\frac{1}{2}r\ddot{\gamma}\sin(\gamma+\beta)-\frac{1}{2}r\ddot{\gamma}\sin(\gamma-\beta)-r\dot{\gamma}\dot{\psi}\sin(\gamma+\beta) \\
&-r\dot{\gamma}\dot{\theta}\sin(\gamma+\beta)-r\dot{\gamma}\dot{\theta}\sin(\gamma-\beta)-\frac{1}{2}\ddot{x}\sin(\psi+\theta-\beta)-\frac{1}{2}\ddot{x}\sin(\psi+\theta+\beta)-r\dot{\gamma}\dot{\psi}\sin(\gamma-\beta) \\
&\qquad+\frac{1}{2}r\ddot{\psi}\cos(\gamma-\beta)+\frac{1}{2}\ell\ddot{\psi}\sin(\phi+\beta)+\frac{1}{2}a\ddot{\psi}\cos(\theta+\beta)-\frac{1}{2}\ell\dot{\psi}\dot{\theta}\sin(\phi+2\beta) \quad \text{(A.1)}
\end{aligned}
$$

$$
\begin{aligned}
&-\ell\ddot{\phi} = \\
&\frac{1}{4}a\dot{\psi}^2\sin(\phi+\theta+\beta)+\frac{1}{2}a\ddot{\psi}\sin(\theta-\phi)-\frac{1}{4}a\ddot{\psi}\cos(\phi+\theta-\beta)-\frac{1}{4}\ell\dot{\theta}^2\sin(2\phi)-r\dot{\psi}\dot{\theta}\cos(-\phi+\gamma)\\
&-\frac{1}{8}\ell\dot{\psi}^2\sin(2\phi-2\beta)-2\dot{\ell}\dot{\psi}\sin(\beta)-\frac{1}{2}r\dot{\theta}^2\cos(-\phi+\gamma)+\frac{1}{2}\ell\dot{\beta}^2\sin(2\phi)-\frac{1}{4}a\dot{\psi}^2\sin(\phi+\theta-\beta)\\
&-\frac{1}{4}\ell\dot{\psi}\dot{\theta}\sin(2\phi+2\beta)+\frac{1}{2}\sin(\psi+\theta+\phi)\ddot{y}-\frac{1}{4}\cos(\psi+\phi+\theta-\beta)\ddot{y}-\frac{1}{2}\ell\dot{\psi}\dot{\beta}\cos(2\phi-\beta)\\
&+\frac{1}{4}r\dot{\gamma}^2\cos(\phi+\beta+\gamma)-\ell\dot{\psi}\dot{\beta}\cos(\beta)+\frac{1}{2}r\dot{\gamma}\dot{\theta}\sin(-\phi+\beta+\gamma)-\frac{1}{8}\ell\dot{\theta}^2\sin(2\phi+2\beta)\\
&-\frac{1}{2}\ell\dot{\theta}\dot{\beta}\cos(2\phi+\beta)-\frac{1}{2}r\dot{\gamma}^2\cos(-\phi+\gamma)+\frac{1}{4}r\ddot{\psi}\cos(-\phi-\beta+\gamma)-\frac{1}{4}r\ddot{\psi}\cos(-\phi+\beta+\gamma)\\
&+\frac{1}{4}a\ddot{\psi}\cos(-\phi+\theta-\beta)+\frac{1}{4}a\ddot{\psi}\cos(\phi+\theta+\beta)+\frac{1}{4}r\ddot{\theta}\cos(-\phi-\beta+\gamma)+\frac{1}{4}\sin(\psi+\phi+\theta-\beta)\ddot{x}\\
&+\frac{1}{2}\cos(\psi+\theta-\phi)\ddot{x}+\frac{1}{2}\cos(\psi+\theta+\phi)\ddot{x}-\frac{1}{2}\ell\dot{\psi}\dot{\theta}\sin(2\phi)-\frac{1}{2}r\dot{\gamma}\dot{\psi}\sin(\phi+\beta+\gamma)\\
&-\frac{1}{2}r\dot{\gamma}\dot{\psi}\sin(-\phi-\beta+\gamma)-\frac{1}{4}\sin(\psi-\phi+\theta-\beta)\ddot{x}-\frac{1}{4}r\ddot{\psi}\cos(\phi-\beta+\gamma)-\frac{1}{4}\ell\dot{\psi}^2\sin(2\phi)\\
&-\frac{1}{2}r\dot{\theta}^2\cos(\phi+\gamma)-\frac{1}{4}\sin(\psi+\phi+\theta+\beta)\ddot{x}+\frac{1}{4}\sin(\psi-\phi+\theta+\beta)\ddot{x}-\frac{1}{4}r\dot{\gamma}^2\cos(-\phi+\beta+\gamma)\\
&-\frac{1}{4}r\ddot{\theta}\cos(-\phi+\beta+\gamma)-\frac{1}{2}r\dot{\psi}^2\cos(\phi+\gamma)+\frac{1}{2}\sin(\psi+\theta-\phi)\ddot{y}-\frac{1}{2}r\dot{\gamma}\dot{\theta}\sin(\phi+\beta+\gamma)-\ell\ddot{\psi}\sin(\beta)\\
&-\frac{1}{2}r\dot{\gamma}\dot{\theta}\sin(-\phi-\beta+\gamma)-\frac{1}{4}r\ddot{\theta}\cos(\phi-\beta+\gamma)-\frac{1}{2}r\dot{\psi}^2\cos(-\phi+\gamma)+\frac{1}{4}r\ddot{\theta}\cos(\phi+\beta+\gamma)\\
&-\frac{1}{2}r\ddot{\gamma}\sin(-\phi+\gamma)-\frac{1}{4}\ell\dot{\psi}\dot{\theta}\sin(2\phi-2\beta)+\frac{1}{4}a\dot{\psi}^2\sin(-\phi+\theta-\beta)+\frac{1}{2}g\sin(\phi+\beta)+\frac{1}{2}g\sin(\phi-\beta)\\
&-\ell\dot{\theta}\dot{\beta}\cos(\beta)-\frac{1}{2}r\ddot{\gamma}\sin(\phi+\gamma)+\frac{1}{2}r\dot{\gamma}\dot{\psi}\sin(-\phi+\beta+\gamma)-\frac{1}{8}\ell\dot{\psi}^2\sin(2\phi+2\beta)+\frac{1}{2}a\ddot{\psi}\sin(\theta+\phi)\\
&-\frac{1}{4}a\ddot{\psi}\cos(-\phi+\theta+\beta)-\frac{1}{2}r\dot{\gamma}^2\cos(\phi+\gamma)-\frac{1}{4}a\dot{\psi}^2\sin(-\phi+\theta+\beta)-\frac{1}{2}a\dot{\psi}^2\cos(\theta+\phi)\\
&+2\dot{\ell}\dot{\phi}-\ell\ddot{\theta}\sin(\beta)+\frac{1}{2}r\dot{\gamma}\dot{\psi}\sin(\phi-\beta+\gamma)+\frac{1}{2}r\dot{\gamma}\dot{\theta}\sin(\phi-\beta+\gamma)-\frac{1}{8}\ell\dot{\theta}^2\sin(2\phi-2\beta)\\
&+\frac{1}{4}r\ddot{\gamma}\sin(\phi+\beta+\gamma)-\frac{1}{4}r\ddot{\gamma}\sin(-\phi-\beta+\gamma)+\frac{1}{4}r\ddot{\gamma}\sin(\phi-\beta+\gamma)-\frac{1}{4}r\ddot{\gamma}\sin(-\phi+\beta+\gamma)\\
&-r\dot{\psi}\dot{\theta}\cos(\phi+\gamma)-\frac{1}{4}r\dot{\gamma}^2\cos(-\phi-\beta+\gamma)+\frac{1}{4}r\ddot{\psi}\cos(\phi+\beta+\gamma)-\frac{1}{2}a\dot{\psi}^2\cos(\theta-\phi)\\
&+\frac{1}{4}\cos(\psi-\phi+\theta-\beta)\ddot{y}-2\ell\dot{\theta}\sin(\beta)-\frac{1}{4}\cos(\psi-\phi+\theta+\beta)\ddot{y}+\frac{1}{4}r\dot{\gamma}^2\cos(\phi-\beta+\gamma)\\
&-\frac{1}{2}\ell\dot{\psi}\dot{\beta}\cos(2\phi+\beta)+\frac{1}{4}\cos(\psi+\phi+\theta+\beta)\ddot{y}-\frac{1}{2}\ell\dot{\theta}\dot{\beta}\cos(2\phi-\beta) \quad \text{(A.2)}
\end{aligned}
$$

APPENDIX B

LAGRANGE'S EQUATIONS SOURCE CODE

This is the source code used to derive the equations of motion for a mobile boom crane using Lagrange's Equations and the symbolic toolbox in *Matlab*:

```
%Mobile Boom Crane Dynamic Model Using Lagrange's Equations
%Jon Danielson
clc
clear all
syms r a h real
syms theta thetap thetapp real
syms l lp lpp real
syms mp G real
syms x xp xpp real
syms y yp ypp real
syms psi psip psipp real
syms gam gamp gampp real
syms phi phip phipp real
syms beta betap betapp real

%Generate Rotation Matrices
    T0=[cos(psi) sin(psi) 0
       -sin(psi) cos(psi) 0
       0              0       1]';

    T1=[cos(theta) sin(theta) 0
       -sin(theta) cos(theta) 0
       0              0       1]';
    T2=[cos(gam) 0  -sin(gam)
            0    1    0
        sin(gam) 0   cos(gam)];
    T3=T2';
    T4=[1 0 0
        0 cos(beta) sin(beta)
       0 -sin(beta) cos(beta)];

    T5=[cos(phi) 0 -sin(phi)
        0        1          0
        sin(phi) 0  cos(phi)];
%position vector from origin to payload
    r_o_p=simple([x y 0]'  + T0*[0 a h]' + T0*T1*T2*[r 0 0]' ...
       + T0*T1*T2*T3*T4*T5*[0 0 -l]');
%time-dependent variables
```

```
    vars=[x,y,l,psi,theta,gam,phi,beta];
%differenciate the position vector to get velocity vector
    v_o_p=difft(r_o_p,vars);
%Kinetic Energy
    T=simple(1/2*mp*dot(v_o_p,v_o_p));
%Potential Energy
    V=mp*G*r*sin(gam) + mp*G*l*(1-cos(phi)*cos(beta));
%Lagrangian
    L=T-V;
%Lagrange's Equations:
%phi general coordinate
    Zero1=simple(   difft(diff(L,phip),vars) - diff(L,phi)   );
    phipp=solve(Zero1,phipp);
    syms gamma gammap gammapp
    phipp=subs(phipp,{gam,gamp,gampp},{gamma,gammap,gammapp})
%beta general coordinate
    Zero2=simple(difft(diff(L,betap),vars) - diff(L,beta));
    betapp=solve(Zero2,betapp);
    betapp=subs(betapp,{gam,gamp,gampp},{gamma,gammap,gammapp})
```

• `difft.m` will perform a symbolic implicit differentiation with respect to time (created by the author):

```
function [out]=difft(exp,var,numderiv)
out=0;
%create the new differentiated variables
    for j=1:length(var)
        %add the derivatives of variables
        var=[var strcat(char(var(j)),'p') strcat(char(var(j)),'pp')];
    end
%perform the implicit differentiation
for i=1:length(var)
    out = out+( diff(exp,var(i)) ) * sym(strcat(char(var(i)),'p'));
end
```

The resultant equations of motion are:

$$\ell\ddot{\phi} = \dot{\theta}^2\ell\cos\phi\sin\phi\cos^2\beta - 2\dot{\beta}\dot{\psi}\ell\cos\beta\cos^2\phi - \ddot{\psi}a\sin\beta\sin\phi\sin\theta - 2\dot{\beta}\dot{\theta}\ell\cos\beta\cos^2\phi +$$
$$2\dot{\psi}\ell\cos\phi\dot{\theta}\sin\phi\cos^2\beta - 2\dot{\ell}\dot{\theta}\sin\beta - \ddot{\psi}\ell\sin\beta - g\sin\phi\cos\beta - \ddot{y}\sin\beta\sin\phi\cos\psi\cos\theta -$$
$$\ddot{\psi}r\cos\gamma\sin\beta\sin\phi + \ddot{\gamma}r\sin\gamma\cos\phi + \ddot{y}\sin\beta\sin\phi\sin\psi\sin\theta + \dot{\gamma}^2 r\sin\gamma\cos\beta\sin\phi -$$
$$\ddot{\gamma}r\cos\gamma\cos\beta\sin\phi + \dot{\psi}^2 r\cos\gamma\cos\phi - \dot{\beta}^2\ell\cos\phi\sin\phi + \dot{\gamma}^2 r\cos\gamma\cos\phi + \ddot{x}\cos\phi\sin\psi\sin\theta +$$
$$2\dot{\gamma}\dot{\theta}r\sin\gamma\sin\beta\sin\phi - \ddot{\theta}r\cos\gamma\sin\beta\sin\phi + 2\dot{\psi}r\cos\gamma\dot{\theta}\cos\phi - 2\dot{\ell}\dot{\phi} -$$
$$2\dot{\ell}\dot{\psi}\sin\beta + \ddot{\psi}a\cos\phi\cos\theta + 2\dot{\gamma}\dot{\psi}r\sin\gamma\sin\beta\sin\phi + \dot{\theta}^2 r\cos\gamma\cos\phi + \dot{\psi}^2\ell\sin\phi\cos\phi\cos^2\beta -$$
$$\ddot{\theta}\ell\sin\beta + \dot{\psi}^2 a\sin\beta\sin\phi\cos\theta - \ddot{y}\cos\phi\sin\psi\cos\theta - \ddot{x}\cos\phi\cos\psi\cos\theta + \dot{\psi}^2 a\cos\phi\sin\theta +$$
$$\ddot{x}\sin\beta\sin\phi\cos\psi\sin\theta + \ddot{x}\sin\beta\sin\phi\sin\psi\cos\theta - \ddot{y}\cos\phi\cos\psi\sin\theta \tag{B.1}$$

$$\ell\cos\phi\ddot{\beta} = -g\sin\beta + \ddot{\psi}a\cos\beta\sin\theta + 2\dot{\ell}\dot{\theta}\sin\phi\cos\beta + \ddot{\psi}r\cos\gamma\cos\beta + 2\dot{\ell}\dot{\psi}\sin\phi\cos\beta +$$
$$2\dot{\phi}\ell\dot{\beta}\sin\phi + \ddot{\theta}r\cos\gamma\cos\beta + \ddot{\theta}\ell\sin\phi\cos\beta - \dot{\psi}^2 a\cos\beta\cos\theta + \dot{\gamma}^2 r\sin\gamma\sin\beta -$$
$$\ddot{\gamma}r\cos\gamma\sin\beta - \ddot{x}\cos\beta\cos\psi\sin\theta - \ddot{x}\cos\beta\sin\psi\cos\theta + \ddot{y}\cos\beta\cos\psi\cos\theta - \ddot{y}\cos\beta\sin\psi\sin\theta +$$
$$\ddot{\psi}\ell\sin\phi\cos\beta - 2\dot{\gamma}\dot{\psi}r\sin\gamma\cos\beta - 2\dot{\gamma}\dot{\theta}r\sin\gamma\cos\beta + 2\dot{\phi}\dot{\theta}\ell\cos\phi\cos\beta +$$
$$2\dot{\phi}\dot{\psi}\ell\cos\phi\cos\beta + 2\dot{\psi}\ell\sin\beta\cos\phi\dot{\theta}\cos\beta + \dot{\psi}^2\ell\sin\beta\cos\phi\cos\beta + \dot{\theta}^2\ell\sin\beta\cos\phi\cos\beta -$$
$$2\dot{\ell}\cos\phi\dot{\beta} \tag{B.2}$$

REFERENCES

[1] Abdel-Rahman, E. and Nayfeh, A., "Pendulation reduction in boom cranes using cable length manipulation," *Nonlinear Dynamics*, vol. 27, no. 3, pp. 255–269, 2002.

[2] Antonelli, G., Chiaverini, S., Palladino, M., Gerio, G., and Renga, G., "Cartesian space motion planning for robots. an industrial implementation," in *Proceedings of the Fourth International Workshop on Robot Motion and Control*, (Puszczykowo, Poland), 2004.

[3] Arnold, E., Sawondy, O., Hilderbrandt, A., and Schneider, K., "Anti-sway system for boom cranes based on an optimal control approach," in *American Control Conference*, vol. 4, (Denver, CO), pp. 3166–71, 2003.

[4] Arteaga, M., Castillo-Sanchez, A., and Parra-Vega, V., "Cartesian control of robots without dynamic model and observer design," *Automatica*, vol. 42, no. 3, pp. 473–480, 2005.

[5] Bhattacharyya, R., "Behavior of a rubber spring pendulum," *ASME Journal of Applied Mechanics*, vol. 67, pp. 332–337, 2000.

[6] Blackburn, D., Lawrence, J., Danielson, J., Singhose, W., Kamoi, T., and Taura, A., "Radial-motion assisted command shapers for nonlinear tower crane rotational slewing," *submitted to Control Engineering Practice*, 2007.

[7] CK-Series-Cranes, "Kobelco crawler cranes," *www.kobelcocranesnorthamerica.com/products.aspx*, accessed Januray 2007.

[8] Craig, J., *Introduction to Robitcs: Mechanics and Control, Second Edition*. Addison-Wesley, 1989.

[9] Danielson, J., Lawrence, J., and Singhose, W., "Command shaping for flexible systems with constant acceleration limits," *accepted to ASME Journal of Dynamic Systems, Measurement, and Control*, 2007.

[10] Eloundou, R. and Singhose, W., "Interpretation of smooth reference commands as input shaped functions," in *American Control Conference*, (Anchorage, AK), pp. 4948–4953, 2002.

[11] Groom, K., Parker, G., Robinett, R., and Leban, F., "Swing-free carnes via input shaping of operator commands," in *Proceedings of the 16th IAARC/IFAC/IEEE International Symposium on Automation and Robotics in Construction*, (Madrid, Spain), pp. 417–21, Univ. Carlos III de Madrid, Madrid, Spain, 1999.

[12] Hekman, K. A. and Singhose, W. E., "A feedback control system for suppressing crane oscillation with on-off motors," *Int. Journal of Control, Automation, and Systems*, vol. 5, no. 3, pp. 223–233, 2007.

[13] Hong, K.-T. and Hong, K.-S., "Input shaping and vsc of container cranes," in *IEEE International Conference on Control Applications*, (Taipei, Taiwan), pp. 1570–1575, 2004.

[14] Huey, J. and Singhose, W., "Effect of vertical acceleration on the frequency of a pendulum: Impact on input shaping," in *Proceedings of 2003 IEEE Conference on Control Applications*, vol. 1, (Istanbul, Turkey), pp. 532–537, 2003.

[15] Hyde, J. M. and Seering, W. P., "Using input command pre-shaping to suppress multiple mode vibration," in *IEEE Int. Conf. on Robotics and Automation*, vol. 3, (Sacramento, CA), pp. 2604–2609, IEEE, 1991.

[16] Kenison, M. and Singhose, W., "Concurrent design of input shaping and proportional plus derivative feedback control," *J. of Dynamic Systems, Measurement, and Control*, no. September, 2002.

[17] Khalid, A., Singhose, W., Huey, J., Lawrence, J., and Frakes, D., "Human operator performance testing using an input shaped bridge crane," *J. of Dynamic Systems, Measurement, and Control*, 2006.

[18] Khorrami, F., Jain, S., and Tzes, A., "Experimental results on adaptive nonlinear control and input presahping for multi-link flexible manipulators," *Automatica*, vol. 31, no. 1, pp. 83–97, 1995.

[19] Kim, Y.-S., Hong, K.-S., and Sul, S.-K., "Anti-sway control of container cranes, inclinometer, observer, and state feedback," *International Journal of Control, Automation, and Systems*, vol. 2, pp. 435–449, 2004.

[20] Kinceler, R. and Meckl, P., "Input shaping for nonlinear systems," in *American Controls Conference*, vol. 1, (Seattle, Washington), pp. 914–918, 1995.

[21] Lawrence, J., Fatkin, B., Singhose, W., Weiss, R., Erb, A., and Glauser, U., "An internet-driven tower crane for dynamics and controls education," in *7th IFAC Symposium on Advances in Control Education*, (Madrid, Spain), 2006.

[22] Lawrence, J., Singhose, W., and Hekman, K., "Friction-compensating command shaping for vibration reduction," *ASME J. of Vibration and Acoustics*, vol. 127, pp. 307–314, 2005.

[23] Lawrence, J., Danielson, J., and Singhose, W., "Analysis and design of input shapers for systems with a braking nonlinearity," in *International Symposium on Flexible Automation*, (Osaka, Japan), 2006.

[24] Lawrence, J. and Singhose, W., "Design of a minicrane for education and research," in *6th International Workshop on Research and Education in Mechatronics*, (Annecy, France), pp. 254–259, 2005.

[25] Lawrence, J. and Singhose, W., "Command shaping slewing motions for tower cranes," *Accepted to J. of Vibration and Acoustics*, 2008.

[26] Lawrence, J., Singhose, W., and Heckman, K., "Robust friction-compensating input shapers," in *8th Cairo Univ. Int. Conf. on Mechanical Design and Production*, (Cairo, Egypt), 2004.

[27] Lawrence, J., Singhose, W., Weiss, R., Erb, A., and Glauser, U., "An internet-driven tower crane for dynamics and controls education," in *IFAC Symp. on Control Education*, (Madrid, Spain), 2006.

[28] Lewis, D., Parker, G., Driessen, B., and Robinett, R., "Command shaping control of an operator-in-the-loop boom crane," in *American Control Conference*, vol. 5, (Philadelphia, Pennsylvania), pp. 2643–7, 1998.

[29] Manning, R., Kim, D., and Singhose, W., "Recution of distributed payload bridge crane oscillations," in *WSEAS International Conference on Automatic Control, Modelling, and Simulation*, (Istanbul, Turkey), 2008.

[30] Muenchhof, M. and Singh, T., "Concurrent feedforward/feedback controller design using time-delay filters," in *AIAA Guidance, Navigation, and Control Conf.*, (Monterey, CA), 2002.

[31] Noakes, M. W. and Jansen, J. F., "Generalized inputs for damped-vibration control of suspended payloads," *Robotics and Autonomous Systems*, vol. 10, no. 2, pp. 199–205, 1992.

[32] Pao, L. Y., "Multi-input shaping design for vibration reduction," *Automatica*, vol. 35, no. 1, pp. 81–89, 1999.

[33] Pao, L. Y. and Singhose, W. E., "Verifying robust time-optimal commands for multi-mode flexible spacecraft," *AIAA J. of Guidance, Control, and Dynamics*, vol. 20, no. 4, pp. 831–833, 1997.

[34] Park, B. J., Hong, K.-S., and Huh, C., "Time-efficient input shaping control of container cranes," in *International Conference on Control Applications*, (Anchorage, AK), pp. 80–85, 2000.

[35] Price, R. H., "Projectiles, pendula, and special relativity," *American Journal of Physics*, vol. 73, no. 5, p. 433, 2005.

[36] Rappole, B. W. J., Singer, N., and Seering, W. P., "Multiple-mode impulse shaping sequences for reducing residual vibrations," in *23rd Biennial Mechanisms Conference*, (Minneapolis, MN), pp. 11–16, 1994.

[37] Rowland, D. R., "The period of a pendulum in a uniformly accelerating reference frame," *American Journal of Physics*, vol. 74, no. 9, p. 839, 2006.

[38] RT530E-2, "Grove rough terrain cranes," *www.manitowoccranegroup.com*, accessed April 2008.

[39] Sawondy, O., Aschemann, H., Kumpel, J., Tarin, C., and Schneider, K., "Anit-sway control for boom cranes," in *Proceedings of the 2002 American Control Conference*, vol. 1, (Ankorage, AK), 1992.

[40] Schmidt, B. A. and McDowell, D. G., "Analysis of a rotating pendulum with a mass free to move radially," *ASME Journal of Applied Mechanics*, vol. 65, no. 3, pp. 778–781, 1998.

[41] Shen, J., Sanyal, A. K., and Chaturvedi, N. A., "Dynamics and control of a 3d pendulum," in *43rd IEEE Conference on Decision and Control*, (Atlantis, Paradise Island, Bahamas), 2004.

[42] Singer, N. and Seering, W. P., "Preshaping command lnputs to reduce system vibration," *ASME Journal of Dynamic Systems, Measurement, and Control*, vol. 112, pp. 76–82, 1990.

[43] Singer, N. and Seering, W. P., "An extension of command shaping methods for controlling residual vibration using frequency sampling," in *IEEE International Conference on Robotics and Automation*, (Nice, France), pp. 800–805, 1992.

[44] Singer, N., Singhose, W., and Kriikku, E., "An input shaping controller enabling cranes to move without sway," in *ANS 7th Topical Meeting on Robotics and Remote Systems*, (Augusta, GA), 1997.

[45] Singer, N. C., Singhose, W. E., and Seering, W. P., "Comparison of filtering methods for reducing residual vibration," *European J. of Control*, no. 5, pp. 208–218, 1999.

[46] Singh, T. and Heppler, G. R., "Shaped input control of a system with multiple modes," *ASME Journal of Dynamic Systems, Measurement, and Control*, vol. 115, no. 3, pp. 341–347, 1993.

[47] Singhose, W., Seering, W. P., and Singer, N., "Input shaping for vibration reduction with specified insensitivity to modeling errors," in *Japan-USA Sympoisum on Flexible Automation*, vol. 1, (Boston, MA), pp. 307–313, 1996.

[48] Singhose, W. E., Crain, E., and Seering, W., "Convolved and simultaneous tow-mode input shapers," *IEEE Control Theory and Applications*, vol. 144, pp. 515–520, 1997.

[49] Singhose, W., Biediger, E. O., Chen, Y.-H., and Mills, B., "Reference command shaping using specified-negative-amplitude input shapers for vibration reduction," *J. of Dynamic Systems, Measurement, and Control*, vol. 126, no. March, pp. 210–214, 2004.

[50] Singhose, W., Derezinski, S., and Singer, N., "Extra-insensitive input shapers for controlling flexible spacecraft," *AIAA J. of Guidance, Control, and Dynamics*, vol. 19, no. 2, pp. 385–91, 1996.

[51] Singhose, W., Kim, D., and Kennison, M., "Input shaping control of double-pendulum bridge crane oscillations," *Accepted to ASME J. of Dynamic Systems, Measurement, and Control*, 2008.

[52] Singhose, W., Porter, L., Kenison, M., and Kriikku, E., "Effects of hoisting on the input shaping control of gantry cranes," *Control Engineering Practice*, vol. 8, no. 10, pp. 1159–1165, 2000.

[53] Singhose, W., Singer, N., and Seering, W., "Time-optimal negative input shapers," *ASME J. of Dynamic Systems, Measurement, and Control*, vol. 119, no. June, pp. 198–205, 1997.

[54] Singhose, W., Vaughan, J., Danielson, J., and Lawrence, J., "The use of teleoperated cranes for advanced controls education," in *ASME IMECE*, (Seattle, WA), 2007.

[55] Smith, O. J. M., *Feedback Control Systems*. New York: McGraw-Hill Book Co., Inc., 1958.

[56] Smith, O. J. M., "Posicast control of damped oscillatory systems," *Proceedings of the IRE*, vol. 45, no. September, pp. 1249–1255, 1957.

[57] Sorensen, K., Fisch, H., Dickerson, S., Singhose, W., and Glauser, U., "A multi-operational-mode anti-sway and positioning control for an industrial bridge crane," in *IFAC World Congress*, (Seoul, Korea), 2008.

[58] Sorensen, K. and Singhose, W., "Oscillatory effects of common hard nonlinearities on systems using two-impulse zv input shaping," in *American Control Conf.*, (New York City, NY), 2007.

[59] Sorensen, K., Singhose, W., and Dickerson, S., "A controller enabling precise positioning and sway reduction in bridge and gantry cranes," *Control Engineering Practice*, vol. 15, no. 7, pp. 825–837, 2007.

[60] Sorensen, K., Singhose, W., and Dickerson, S., "A controller enabling precise positioning and sway reduction in bridge and gantry cranes," *Control Engineering Practice*, vol. 15, no. 7, pp. 825–837, 2008.

[61] Sorensen, K. L., Spiers, J. B., and Singhose, W. E., "Operational effects of crane interface devices," in *IEEE Conf. on Industrial Electronics and Applications*, (Harbin, China), 2007.

[62] Sorensen, K. L., *A Combined Feedback and Command Shaping Controller for Improving Positioning and Reducing Cable Sway in Cranes*. Masters thesis, Georgia Institute of Technology, 2005.

[63] Suter, J., Kim, D., Singhose, W., Sorensen, K., and Glauser, U., "Integrating a wireless touchscreen into a bridge crane control system," in *IEEE/ASME Int. Conf. on Advanced Intelligent Mechatronics*, (Zurich, Switzerland), 2007.

[64] Tallman, G. H. and Smith, O. J. M., "Analog study of dead-beat posicast control," *IRE Transactions on Automatic Control*, no. March, pp. 14–21, 1958.

[65] Tuttle, T. D. and Seering, W. P., "A zero-placement technique for designing shaped inputs to suppress multiple-mode vibration," in *American Control Conf.*, (Baltimore, Maryland), pp. 2533 – 2537, 1994.

[66] URW-94, "Unic mini cranes," *www.minicranes.co.uk*, accessed April 2008.

[67] Vaughan, J., Yano, A., and Singhose, W., "Comparison of robust input shapers," *in press, Journal of Sound and Vibration*, 2008.

[68] Vaughan, J. and Singhose, W., "Comparison of command filterting methods for vibration reduction in automated manufacturing," in *International Symposium on Flexible Automation*, June 23–26 2008.

[69] Vaughan, J., Singhose, W., Debenest, P., Fukushima, E., and Hirose, S., "Initial experiments on the control of a mobile tower crane," in *ASME International Mechanical Engineering Congress and Exposition*, (Seattle, Washington), 2007.